(12)

MICROTUBULES FOR NONLINEAR OPTICAL LIMITING

FINAL REPORT

SwRI Project 01-3165

Prepared by

Stephen T. Wellinghoff, Ph.D.
Charles K. Baker, Ph.D.
Martin J. Sablik, Ph.D.
Ralph H. Hill, Ph.D.
David W. Naegeli, Ph.D.

Original contains color plates: All DTIC reproductions will be in black and white

Prepared for

Joel Schnur, Ph.D.
Naval Research Laboratories
Washington, D.C.

December 3, 1993

SOUTHWEST RESEARCH INSTITUTE
6220 Culebra Road, P.O. Drawer 28510
San Antonio, TX 78228-0510
Telephone: 210/684-5111 Fax: 210/522-3649

DISCLAIMER NOTICE

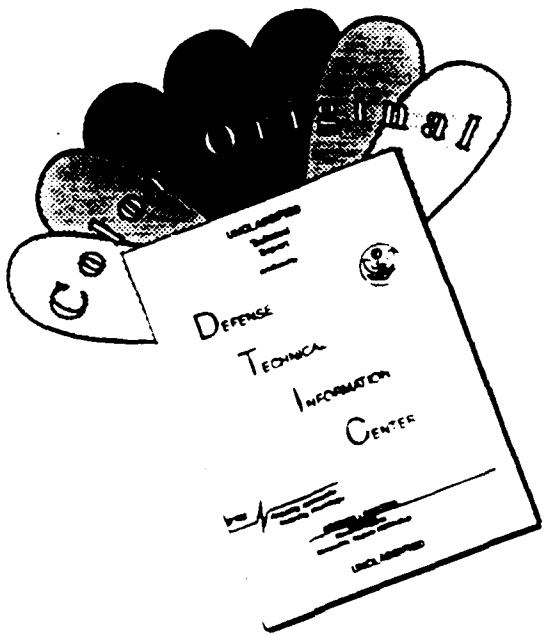

THIS DOCUMENT IS BEST QUALITY AVAILABLE. THE COPY FURNISHED TO DTIC CONTAINED A SIGNIFICANT NUMBER OF COLOR PAGES WHICH DO NOT REPRODUCE LEGIBLY ON BLACK AND WHITE MICROFICHE.

SOUTHWEST RESEARCH INSTITUTE
6220 CULEBRA ROAD, P.O. DRAWER 28510
SAN ANTONIO, TEXAS 78228-0510

MICROTUBULES FOR NONLINEAR OPTICAL LIMITING

FINAL REPORT

SwRI Project 01-3165

Prepared by

Stephen T. Wellinghoff, Ph.D.
Charles K. Baker, Ph.D.
Martin J. Sablik, Ph.D.
Ralph H. Hill, Ph.D.
David W. Naegeli, Ph.D.

Prepared for

Joel Schnur, Ph.D.
Naval Research Laboratories
Washington, D.C.

December 3, 1993

APPROVED:

Donald E Johnson

Donald E. Johnson, Ph.D.
Vice President

SOUTHWEST RESEARCH INSTITUTE

TABLE OF CONTENTS

TABLE OF CONTENTS (CONT'D)

LIST OF FIGURES

LIST OF FIGURES (CONT'D)

1. INTRODUCTION

1.1 Device Concepts

The effort in visible laser eye and sensor protection has focussed on several problems, one of which was the threshold for laser eye damage of 1.0-0.1 microjoule ($\mu J/cm^2$ (or 1000-100 W/cm^2 for a nanosecond pulse) over a broad wavelength range from 400-700 nm. This value is the so-called "clamping threshold" which is the maximum intensity permitted to exit the optical device, regardless of the input intensity.

The most interest was concentrated in finding a solution for nanosecond threats by a retrofit of existing equipment (binoculars, periscope viewers, etc.,) or by fabrication into a simple set of goggles or a visor. This very low clamping threshold, of course, requires a very highly nonlinear material that is fast and operates over a wide frequency range. The nonlinear materials work can be classified into the following types:

1) Liquid crystals
2) Organometallics and polymers
3) Ultrarapid crystallizing alloys and other thermally induced phase changes
4) Phase conjugate mirrors

Ideally, one would simply put a coating onto an optical element and it would let light through below 0.1 $\mu J/cm^2$ and absorb, scatter, or reflect all light above this value. Unfortunately, all of the above materials undergo this change in behavior at powers no smaller than 1 MW/cm^2, 10^4-10^3 higher than the damage threshold for the eye. This then requires that the light be focussed into the nonlinear material using a very "fast" lens (f/1 to f/2) or multiple lens arrays.

In the case of binoculars these focusing powers can be achieved by placing the nonlinear elements at some intermediate focal plane. The constraints are less severe in this case since the field of view is small and there is space for large lenses. One material concept proposes to use the sacrificial, explosive crystallization of supercooled ceramics to change from a reflecting to a nonreflecting surface (Fibertek). The hurdles to be overcome are improvement in the reflectivity at low intensity and some image distortion problems.

Other approaches using a thermal effect are more reversible. In one case composite layers of V_2O_5 and Ge are grown on the optical element (Rockwell). The Ge absorbs the infrared light and heats the vanadium oxide, converting it from an infrared transparent monoclinic material to the infrared reflector, rutile structure, at higher temperature. The film is designed so as to achieve maximum heat transfer to the oxide in the shortest time. This device does not switch in the visible however.

Lead silicate glass (Oklahoma State) was employed in an apertured device to generate a device with a clamped power at 457 nm of 10-20 MW/cm^2, well off the goal by two orders of magnitude. Other materials presented included Langmuir-Blodgett films with high second order nonlinearities (University of Manchester) but the practical application of these seemed rather distant.

Other approaches use up to 23 layers containing alternating layers of Si (napthophthalocyanine) absorber doped methyl methacrylate polymers and methyl methacrylate (Lockheed-Celanese). This device depends on Bragg reflection from the $\lambda/4$ thick layers of different refractive index at the organometallic resonance. At high intensities the absorber bleaches, reducing the refractive index of the layer to the adjacent undoped layer, permitting the stack to completely transmit. Reflectivities can be changed from 0.15 to 0 at 1 MW/cm^2 over a bandwidth of 20 nm. The investigators are now "chirping" the layers (changing the layer thickness from top to bottom of the stack in a controlled way) to increase bandwidth. This will also improve field of view which is now limited but will probably reduce the sharpness of the optical limiting effect.

A wide variety of materials was discussed by Naval Research Laboratories (NRL) including metal clusters in nonlinear matrices, rare earth napthophlalocyanines for visible limiting. Iron cobalt carbonyls were also proposed as visible limiters (University of Iowa and Hughes). Materials undergoing semimetal to metal transitions such as PbSnSe alloys were briefly discussed as IR limiters. All of these materials suffered from the need to generate the nonlinearity on resonance, and even then the observed nonlinearity was still several orders of magnitude away from that desired for laser eye protection.

A variable overlap superlattice concept was proposed as an interesting idea for minimizing absorptive losses but for increasing nonlinear refractive index. However, no numbers were quoted.

In addition to the materials described above, doped barium titanate was employed in a so-called "excisor" (two wave mixing) configuration where coherent laser radiation was reflected but incoherent radiation was passed (Hughes). The concept is still 10^3-10^4 away from laser eye protection goals.

With the great service interest in nanosecond protection, limiters containing liquid crystals are a possibility. The nonlinearity is nonresonant. Therefore, the optical element can be exceptionally clear and local heating is not as much a problem. In addition liquid crystals are self-healing. Here the fastest nonlinearity is a reorientation around the long molecular axis. Typically the liquid crystal is oriented between glass plates to form a clear transparency (Penn State) or distributed in a holey film of a matching refractive index (Kent State). Upon laser irradiation, microdomains are rotated out of overall orientation by the light electric field, causing differences in local refractive index, scattering of light and optical limiting.

In all cases, because of the limitations in the optical nonlinearity of the material, focussing of the radiation is necessary. In the case of a visor or "nonlinear eyeglasses", a single lens is not sufficient. A lateral array of microlenses with fast f/1 optics is being microlithographically fabricated in plastic by MIT Lincoln laboratories. The mixture of refractive and diffractive optics necessary for correction of coma, spherical and chromatic aberrations requires that four layers of these lenses be stacked and aligned with respect to one another. The nonlinear material is placed in the back focal plane of the lens arrays. Since the nonlinear material behind the first lens will defocus high intensity radiation outside the aperture of the second lens the exiting intensity will be clamped. Remaining problems include vignetting of one lens by another, alignment of all four layers of lenses, optical distortions and field of view.

Working with Corning, Optical Shields has fabricated a limiter that consists of a front surface of an array of 200-micrometer (μm) diameter glass microlenses with a focus distance of 0.8 mm, homeotropically ordered smectic A phase, and an apertured back plate that lets through all linear light. The clamping power at the focus position is about 0.75 J/cm^2 at 532 nm with a 5-nanosecond (nsec) pulse width which converts to a device clamping power of about 50 mJ/cm^2. This is an order of magnitude and a half away from the goal. The device damage threshold due to the destruction of the solid glass elements is quite high, on the order of 0.03 J/cm^2. The so-called "dynamic range" of the device is thus quite large.

Combination of this approach with the microlens array device seems to offer the best chance for a broad band eyeglass or visor protection in the nanosecond regime. At present the nonlinearity of the material needs to be improved by about two orders of magnitude and the optical defects of the four-layer microlens system needs to be corrected. It is not clear that the path to either of these goals is going to be easy since the demands for each further incremental improvement gets larger.

1.2 Nonlinear Optical (NLO) Materials

1.2.1 Optical Nonlinearities Based On One Dimensional Excitons

Because of the extensive energy splitting of outer π orbitals in extended 1-d structures such as polydiacetylene, the available oscillator strength, which is proportional to the electron density of the material, (practically, the volume density of carbon p orbitals), is borrowed into the lowest energy π-π* transition. The low lying excited electronic states (highest occupied MO, HOMO, or valence band and lowest unoccupied MO, LUMO or conduction band) can thus be strongly polarized by the light field. In addition, the very strong coupling of the electronic transition with backbone vibrations further concentrates oscillator strength into an exciton (bound electron hole pair) transition at the high energy side of the first transition.

The 500 fsec to 5 psec nonlinear absorption of a weak probe beam, ω_t, subsequent to excitation by a stronger pump beam, ω_p, is dominated by bleaching of this exciton transition by the pump beam [1]. The bleaching of the π-π* manifold is observed both for resonant and nonresonant pumping. The decay of the bleaching measured at the exciton peak by the probe beam is virtually instantaneous (<500 fsec) for nonresonant pump beam excitation (virtual states accessed) and considerably longer for resonant excitation (stationary states with finite lifetimes accessed). Peaks in the bleaching response preresonant to the exciton resonance are due to coupling with optical phonons.

The exciton mediated, third order, electronic nonlinearity is independent of exciton size and is dependent only on the linear absorption coefficient. Every material with low lying electronic transitions will thus exhibit the same nonlinear absorption per electron-hole pair excited. However, along with the higher overall absorption in 1-d organics comes the possibility of damage due to decay into photoactive triplet states [2]. This argument also holds in the "nonresonant regime" where virtual excitons that can exist only in the presence of the optical field control the nonlinear response.

High frequency vibrations (ca. 2000 cm^{-1}) and their overtones couple extensively with the electronic transitions of conjugated molecules with consequent broadening of the electronic transitions. Extinction coefficients in the "nonresonant" regime are usually greater than 1 cm^{-1}. Low molecular weight crystalline solids GaAs, NaCl etc. on the other hand show extinctions of only 10^{-3} to 10^{-6} cm^{-1}.

The intensity dependent refractive index, n_2 ($n_t = n_o + n_2 I$), is simply the result of the change in the absorption coefficient with intensity through the Kramers-Kronig transformation (Figure 1.1) [3]. Thus the only reason conjugated polymers appear to be better nonresonant NLO materials than inorganics is that a higher overall background absorption is maintained in the "nonabsorbing part" of the spectrum. This higher overall absorption assures that the figure of merit, n_2/α, where α is the nonlinear absorption coefficient ($\alpha_t = \alpha_o + \alpha I$) is no better for 1-d polymers when compared to inorganics.

The above discussion clearly points out that no additional nonlinear response can be achieved by making high polymers. Polymers are useful only for their mechanical properties. In our application we wish to dissolve molecules in the liquid crystal cores of optical waveguides. Thus oligomeric or monomeric nonlinear materials are more suitable for our purposes.

1.2.2 Optical Nonlinearities Based On Two Dimensional Sheets

Lamellar phases of $(C_{10}H_{21}NH_3)_2PbI_4$ consist of 14.9 Å hydrocarbon layers separating an edge linked sheet of $(PbI_4)^{-2}$ octahedra of 6.4 Å thickness (Figure 1.2). The strong 2-d confinement and dielectric constant shift across the organic-inorganic boundary results in a strong excitonic peak at 0.51 μm. Off resonance at 1.53 μm (nearly 3-photon resonant with the fundamental excitonic peak), $\chi^3 = 0.7\times10^{-9}$ esu ($n_2 = 10^{-12}$ cm^2/W) [4]. Much larger values of the third order nonlinearity are expected as the probe frequency approaches the exciton fundamental frequency; however, absorption and beam damage can become a problem under these conditions.

Another way to achieve exciton confinement in a two dimensional sheet structure is in the planar multiple quantum well structure (e.g., GaAs-GaAlAs) [5]. For example, at the exciton resonance ($\alpha_o = 10^5$ cm^{-1}), $n_2 = -2\times10^{-4}$ cm^2/W originates in a negative nonlinear absorption (exciton band saturation). Of course these resonant values of nonlinearity can only be achieved if oscillator strength is concentrated in the excitonic peak. The far off-resonance nonlinearity of this structure is less than polyacetylene because of the smaller background absorbance.

It should be noted that in II-VI semiconductors the exciton binding is much higher and saturable exciton bands appear at room temperature in bulk material (single crystal CdS: $n_2 = -10^{-6}$ cm^2/W on resonance) [6].

1.2.3 Optical Nonlinearities Based on Small Crystallites

40 Å diameter nanocrystals of GaAs can be grown in Vycor glass. The exciton is stabilized in the quantum sized particle and thus increases the background absorption due to the exciton tail at 1060 nm are observed, well away from the bandgap. As a result, the "nonresonant"

$n_2 = -5.6 \times 10^{-12}$ cm^2/W at 1060 nm is over an order of magnitude greater than that demonstrated by bulk GaAs at the same frequency [7].

Recently a new technique has been suggested that focuses the optical field in the quantum sized particle. This involves coating small semiconductor particles with metal. The most ideal system is small CdS particles coated with varying thicknesses of silver metal in the 20-50 Å range. Ag in this thickness range exhibits a plasmon resonance in the visible; however, no interband transitions contribute to the absorption. Especially strong effects are expected with interaction of this plasmon resonance with the excitonic resonance of the semiconductor. Optical field, E, magnifications ($I = E^2$) of up to 10× should be observed in the interior of the semiconductor particle.

With a range of coating thicknesses, the plasmon resonance absorption can be spread throughout the visible. It is then possible to obtain a broad band (500-800 nm) χ^3, 10^3 larger than uncoated particles. χ^3 is proportional to n_2 and a nonresonant $n_2 = -10^{-10}$ cm^2/W has been found in glasses doped with a 10^{-3} volume fraction of ca. 50 Å CdS particles [8]. Thus we expect to obtain a $n_2 = -10^{-7}$ cm^2/W over the visible range for the metal coated semiconductor particles. For a 10^{-3} volume fraction of Ag-CdS nanoclusters, the linear absorption coefficient is 400 cm^{-1} throughout the visible region.

1.2.4 Organometallic Materials

The charge transfer contribution to the molecular transitions can be increased by mixing metal d orbital of a transition metal into the π manifold of an electron deficient ligand. Platinum complexes of phthalocyanines exhibit nonresonant third order susceptibilities 50 times greater than the phthalocyanine alone [9]. Main group elements such as Pb were much less effective because of poor participation of d orbitals in the π system.

An especially clear case of oscillator strength borrowing into an intense long wavelength charge transfer (d-π)-(d-π)* transition is seen for Ru(+2) pyrazine complexes [10]. Coupling between the individual pyrazine-Ru(+2) units shifts the transition to longer wavelength as chain length increases. Oxidation of the complex shortens the interaction length, shifting the 700 nm transition to shorter wavelength and increasing the intensity of even a longer wavelength near IR transition.

The long wavelength transition can be pushed even further out into the near infrared with a consequent opening of the visible window. Ru(+2) d^6 metal complexes with highly electron deficient ligands such as 2-azo(bispyridine) (ABPY) and bis-(2-pyridine)-1,2,4,5-tetrazene (BPTZ) [11]. The longest wavelength transitions are achieved when electron donating groups are placed in the co-ordination sphere of the metal [12]. Recently, HF-SCF calculations have been carried out on dimetallated ABPY complexes to reproduce the frequency and oscillator strengths of the observed linear transitions [13]. As expected no singly excited transitions of significant oscillator strength are predicted in between 450 nm and the near IR transition which consists of a net charge transfer from the azo π orbitals to the metal d orbital lobes above and below the molecular plane. A maximum in χ^3 is predicted just to the long wavelength side of this transition.

1.3 Microtubular Array Concept

As discussed above there is little chance that materials science will be able to produce a broad band, nonlinear material that will be able to clamp at 1-0.1 $\mu J/cm^2$ (1 nsec pulse, 1000 -100 W/cm^2) in the near future. Focusing power by a factor of 100-1000 to on the order of 1 MW/cm^2 in the NLO material will be required while avoiding laser damage from local heating.

Our approach is to make a microtubular waveguide array containing nonlinear material distributed along the length of the tubular waveguide. The purpose of such a configuration is to: 1) accumulate the nonlinear effect over a large distance along the waveguide; 2) distribute any heat of absorption over a large volume; and 3) make a device compatible with a microlens array.

The best device consists of a coaxial light guide with a nonlinear core guide doped with Ag coated quantum sized CdS or ZnSe particles, centered within an annular guide of linear optical behavior such as a homeotropically oriented liquid crystals (Figure 1.3). The concept is to use a microlens to inject focused light into the central guide (Figure 1.4) where it would couple into the mode structure of the central guide. At low powers the higher refractive index of the central guide would contain the light by total internal reflection. All the radiation would appear at the back end of the guide where it would be defocused by another microlens, reconstructing the image point.

At a critical power, P_c, the nonlinear core would bleach reducing the composite refractive index of the central core below that of the annular guide. Light would then leak out of the central guide into the annular guide. If the capillary wall possessed a lower refractive index than even the annular guide, light would pass into the capillary wall where it could be absorbed by a nonreflective broad band absorber.

Since significant light confinement can be obtained if the refractive index difference between core and cladding is on the order of 0.01, the injected power must be able to bleach the internal guide's refractive index by this much. Since Ag coated CdS particles exhibit a broad band $n_2 = 10^{-7}$ cm^2/W at a particle fraction of 0.1%, a focused power of 10^5 W/cm^2 would be required to bleach the central guide. Thus a front microlens of focussing factor 100 would be required for laser eye protection. The linear absorption of the central guide would limit its length to 10-20 μm.

Our concept was to form a coaxial waveguide structure in an array of capillaries. The center guide was to contain either dilute metal-semiconductor particles or NLO organometallics. As a first approach to preparing this device we proposed to utilize semiconductor and/or semiconductor-metal coated, hollow microtubules of ca. 0.5-1.0 μm diameter width and 10-100 μm length [14].

1.4 References

1) B. I. Greene, J. Orenstein, and S. Schmitt-Rink, Science, 247, 679 (1990).
2) S. P. McGlynn, T. Azumi, and M. Kinoshita, "Molecular Spectroscopy of the Triplet State", Prentice Hall, Englewood Cliffs, NJ, 1969.
3) F. Henneberger et al., Appl. Phy. B46, 19 (1988).
4) R. Ito, C. Xu, and T. Kondo, Solid State Mat., 157 (1991).
5) D. S. Chemie, D.A.B. Miller, and P. W. Smith, Optical Eng., 24(4), 556 (1985).

6) F. Henneberger, U. Woggon, J. Puls, and C. Spiegelberg, Appl. Phys., B46, 19 (1988).
7) B. L. Justus, R. J. Tonucci, and A. D. Berry, Appl. Phys. Lett., 61(26), 3151 (1992).
8) S. R. Friberg and P. W. Smith, IEEE J. of Quantum Electr., QE(23)-12, 2089 (1987).
9) James S. Shirk et al., Appl. Phys. Lett. 55 (13), 1287 (1989).
10) A. von Kameke, G.M.Tom and H. Taube, Inorg. Chem. 17(7), 1790 (1978).
11) S. D. Ernst and W. Kaim, Inorg. Chem. 28, 1520 (1988).
12) Final Report for Contract #F33615-86-C-5065 (WPAF), S. K. Lo, S. T. Wellinghoff, S. T. Schwab, D. Herrera, R. Hill, D. Naegeli, and P. Hochmann.
13) Final Report for Contract (CNVEO-Army), S. K. Lo, S. T. Wellinghoff, R. Hill, D. Naegeli, and P. Hochmann.
14) J. H. Georger et al., JACS, 109, 6169 (1987).

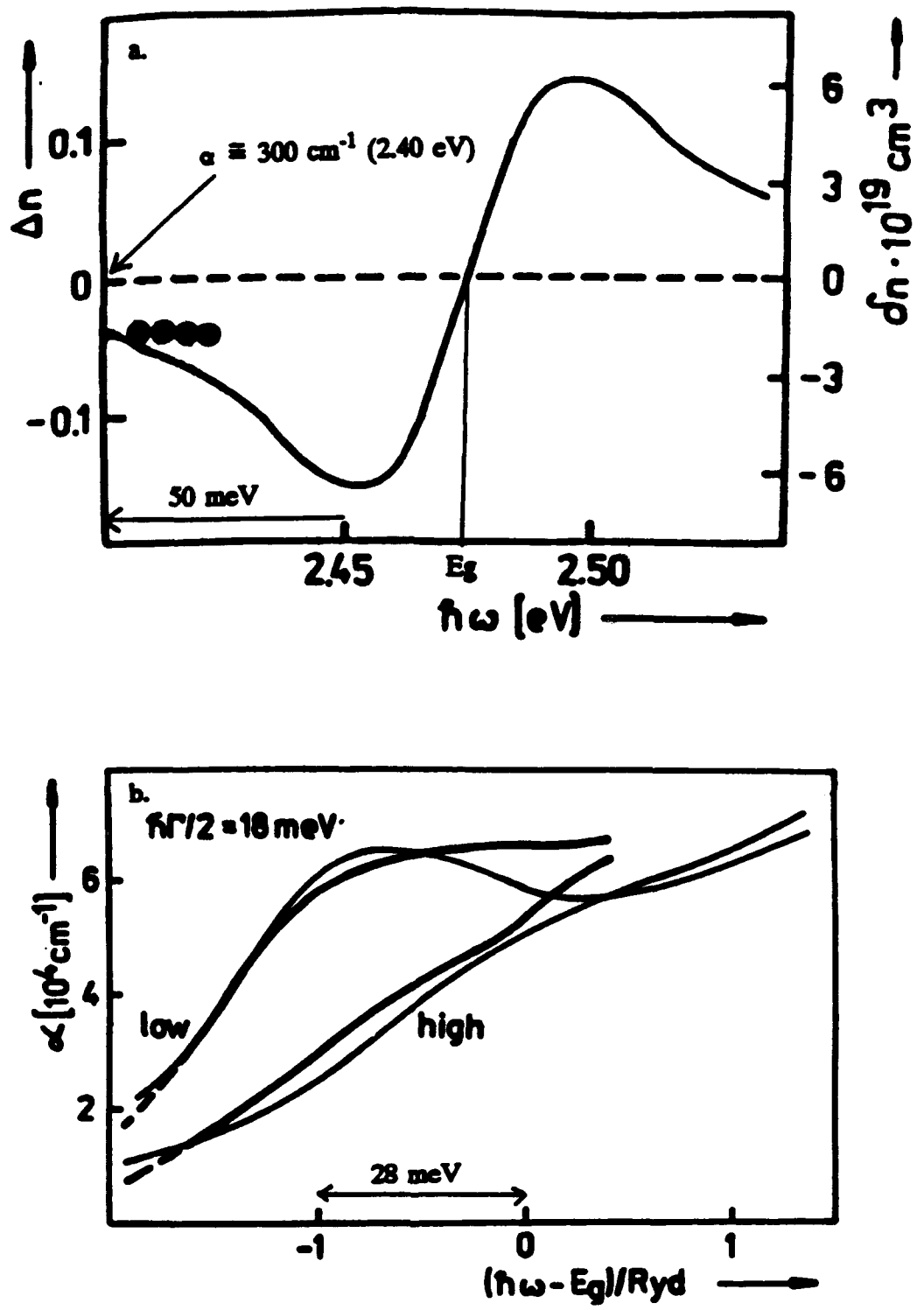

Figure 1.1 a) Alteration of the refraction index of room-temperature CdS in perpendicular polarization obtained from a Kramers-Kronig analysis of the absorption data at 30 kW/cm^2 band-to-band excitation; b) Right scale, (a) refraction change induced by one electron-hole pair in 1 cm^3 CdS. Dots: Data from four-wave mixing experiments, (b) Γ-exciton-phonon binding energy, Ryd-exciton binding energy.

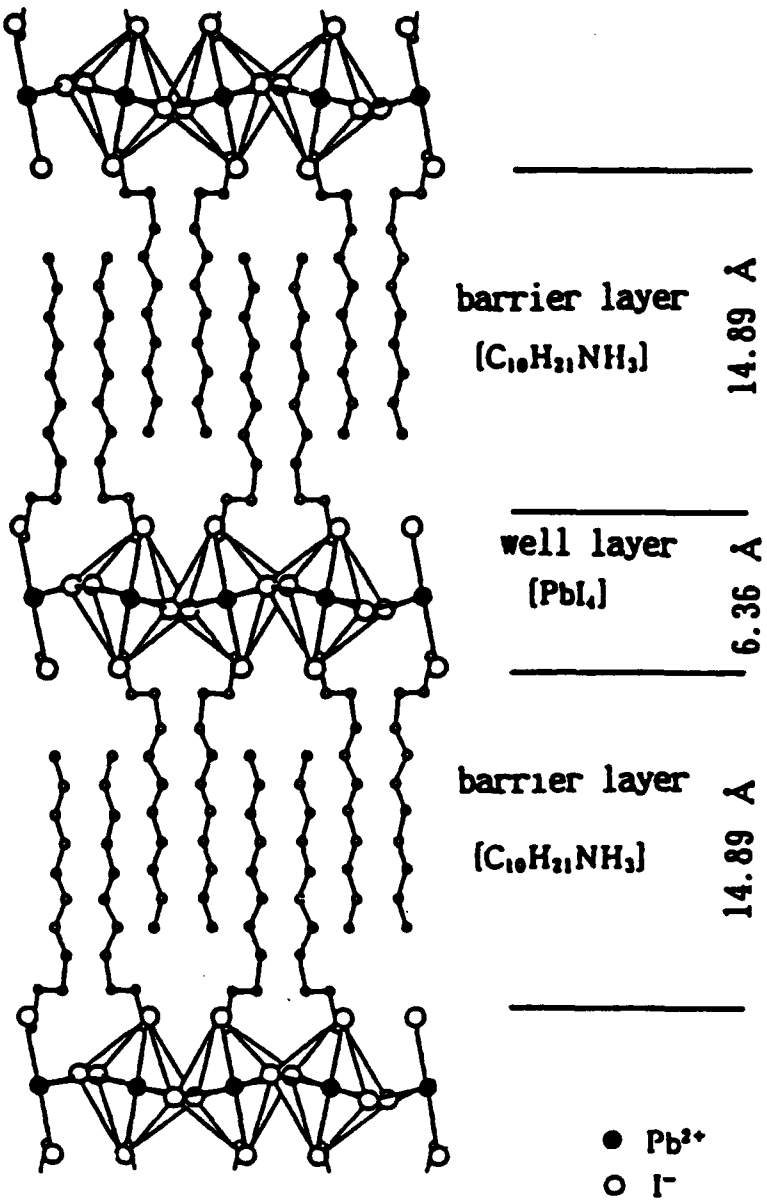

Figure 1.2 Unit cell structure of C_{10}-PbI_4 at 265°C.

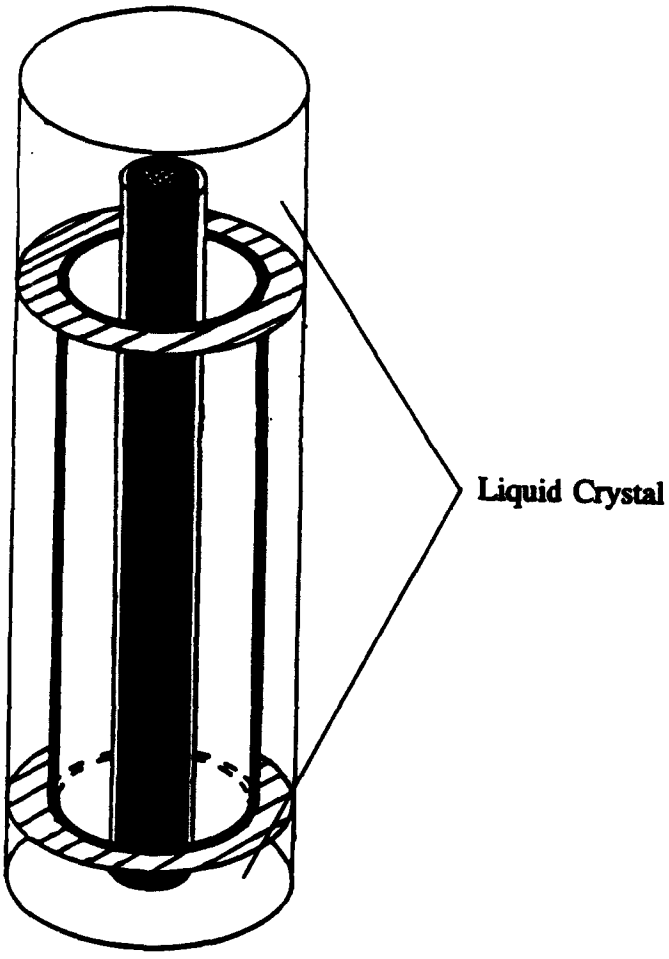

Figure 1.3 Structure of coaxial waveguide showing central guide and annual guide within a capillary.

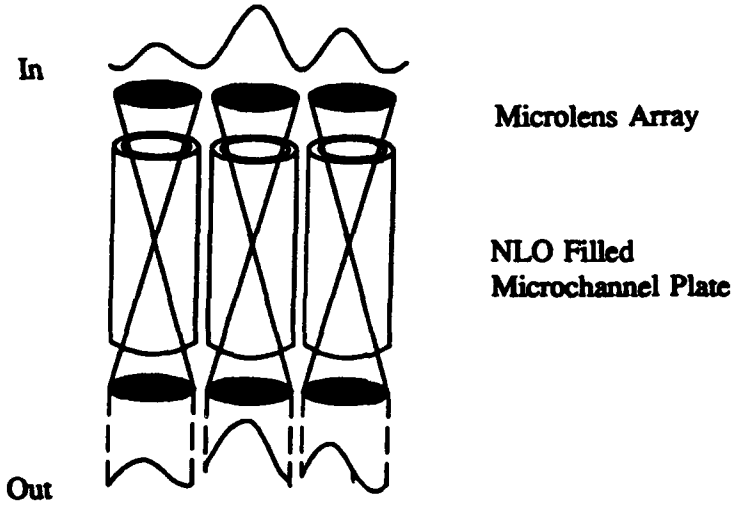

Figure 1.4 Capillary array showing interface with a microlens array.

2. PREPARATION OF COAXIAL WAVEGUIDES

2.1 Introduction

2.1.1 Capillaries Filled with Homeotropically Oriented Nematic Liquid Crystals

Nematic liquid crystals with hydrocarbon tails and polar heads can be forced to orient with the molecular long axis perpendicular to a low energy surface. When such a homeotropically oriented liquid crystal is constrained in a cylinder, a defect must develop where the nematic director orients into the axial direction (Figure 2.1). This orientation transition tends to be rather gradual [1-4]. However, insertion of small diameter fibers into the liquid crystal filled cylinders has revealed that homeotropic orientation can be maintained across the capillary if the fiber radius is large enough and if its surface is homeotropically orienting. In fact the fiber centered capillary is the lowest free energy configuration of the system. This suggests that molecular forces might be sufficient to hold the fiber at the center of the liquid crystal filled capillary if the forces of gravity were not sufficient to settle the fiber.

2.1.2 Capillary Waveguides Using Homeotropically Oriented Smectic A Liquid Crystals

Recent experimental work [5] by Honeywell and theoretical predictions [6-7] show that homeotropically oriented smectic A liquid crystals (K24 (8 CB) or 4-cyano-4'-octylbiphenyl) maintain the homeotropic orientation to within at least 1 μm of the axis of the cylinder tube whereupon a transition to an isotropic state occurs.

It is thus possible to make cylindrical waveguides with low refractive index at the glass wall, high projected refractive index in the annulus of the center and low refractive index in the center of the guide. The Honeywell workers have effectively excited doughnut type waveguide modes in a 150 μm capillary filled with homeotropically oriented K24 (8 CB) in the smectic A. The transmission loss was an exceptionally low 0.5 dB/cm. Some of this power loss was thought to result from inefficiencies in mode swapping which should be minimized by using smaller capillaries.

Rayleigh scattering losses originate from thermal generation of misoriented microdomains in the nematic region above the smectic A to nematic transition. Losses as high as 14 dB/cm were found; however, this loss could be suppressed by the application of AC electric fields perpendicular to the waveguide direction at frequencies above the realignment threshold frequency [8,9].

In the smectic A the bend elastic constant, K_{33}, and twist constant, K_{22}, are several orders of magnitude greater than the splay constant, K_{11}. The respective elastic constants found in nematic liquid crystals are all of the same order of magnitude and much smaller than the larger smectic elastic constants. Thus the likely morphology in a cylinder consists of concentric lamellar layers arranged about the central axis of the cylinder. The greater stiffness of the liquid smectic suppresses the molecular motions which give rise to Rayleigh scattering.

2.1.3 Capillary Waveguides Using Lyotropic Lamellar Phases

Lyotropic lamellar phases might be expected to exhibit similar orientation effects in small capillaries as smectic A phases. The microstructure of these phases consists of alternating lamellae of hydrophobic surfactant structures and water phases (Figure 2.2). Ternary systems of ambiphilic molecules such as alkyl ammonium salts and long chain alkyl carboxylate and sulfonate salts-long chain alcohols and water exhibit these sorts of phases at least in part of the phase diagram [10]. An especially well studied system is sodium caprylate, n-decanol and water whose phase diagram is shown in Figure 2.3 [11]. Five homogeneous mesomorphic phases (B-F) and two isotropic solution phases (L_1, L_2) are found in this system.

Of special interest to us are the lamellar phase D and the hexagonal phase F. The latter phase consists of long hexagonally packed water cylinders embedded in a hydrocarbon phase. The dimensions of the unit cell spacings are on the order of 100 Å in both cases. Since thin water filled lamellae or rods are available, respectively, the way is paved to grow dimensionally constrained NLO materials over substantial lengths in these phases. As mentioned in the introduction, enhancements of the third order susceptibility can be induced in materials of reduced dimensionality.

Attempts have been made to grow silicon dioxide inorganic layers in the water layers of the lamellar phase of didodecylammonium bromide-methanol-water by hydrolysis of alkoxysilanes [12]. Unfortunately, at the final stages of condensation polymerization, buckling and distortion of the lamella structure was observed. However, organic polymers have been free radical polymerized in the layers within a lamellar phase [13].

2.1.4 Flow in Liquid Crystal Filled Capillaries

Shear parallel to the smectic A lamellar layers is quite facile; however, shear perpendicular to the layers is so restricted that viscous flow proceeds by the generation of a trail of dislocations, similar to that seen in a solid [14]. At a high enough shear rate, flow instabilities even develop in Poiseuille flow in capillaries with homeotropic boundary conditions.

The properties of homeotropically oriented, smectic A or lamellar phase–small isotropic core of high energy which could be filled by a microtubule of close to the same radial dimension, high resistance to permeation of material perpendicular to the capillary axis, and low resistance to shear flow parallel to the capillary axis–seem ideally suited for coaxial centering of microtubules.

Thus, in the following section, we will relate the efforts we have made to make coaxial guides and to understand the process of filling and centering of tubules.

2.2 Experimental

2.2.1 Filling of Capillaries with Smectic A Liquid Crystal

The 4-cyano-4-n-octylbiphenyl (K24) liquid crystal used in this study was obtained from BDH Inc. and used as received. This liquid crystal is smectic at room temperature with transitions of: $K \rightarrow S_A$ (21.5°C), $S_A \rightarrow N$ (33.5°C), $N \rightarrow I$ (40.5°C).

Several types of glass capillaries were used in this study. The 50-μm ID Pyrex® glass capillaries were obtained from Vitro Dynamics, Inc. The 12-μm ID lead oxide doped-glass capillaries were custom made for and donated to SwRI by Honeywell, Inc. The nickel coated phospholipid microtubules were prepared by NRL according to previously described procedures and came dispersed in water. These hollow microtubules ranged from 2-3 μm in OD and from 25 to 100 μm in length; however, manipulation of these structures during usage resulted in severe fragmentation.

Dispersion of the microtubules into the K24 was achieved by washing the microtubule/water suspension with large amounts of acetonitrile followed by large amounts of toluene. The microtubule/toluene suspension was then added to the K24 and the entire mixture heated under vacuum for approximately 12 hours in order to remove the toluene.

The 50-μm Pyrex® glass capillaries were prepared for use by cleaning and silanizing them with octadecyltrichlorosilane. They were first cleaned by treating them with hot sulfochromic acid followed by Milli-Q water and toluene rinses and finally by drying them at 250°C for 30 minutes. The capillaries were then silanized by treating them with a 5% octadecyltrichlorosilane-toluene solution followed by a toluene rinse and then by drying them a 250°C for 30 minutes. This silanizing agent orients the liquid crystal molecules homeotropically with the director perpendicular to the surface.

The introduction of all cleaning solutions and the liquid crystal/microtubule suspension into the capillaries was achieved by applying a vacuum suction at one end of the capillary while immersing the other end into the desired solution.

Observation of microtubule alignment and centering was accomplished by attaching a 1-mL glass syringe and 26 gauge needle to one or both ends of a glass capillary prefilled with liquid crystal or a microtubule/K24 mixture. The capillary ends were epoxy sealed to the syringe needles and then pressure or vacuum was applied to the capillary by pushing or pulling the syringe plungers.

All photographs were taken using a Wild MPS11 35 mm camera attached to Nikon Optiphot polarizing light microscope. For the temperature control work, a heating stage was fabricated by attaching resistance ribbon to a glass microscope slide using ceramic cement. The temperature was controlled by varying the current through the ribbon and monitored using a digital thermometer. Two glass capillaries were placed in an index matching fluid between the glass slide and cover slip to prevent optical distortion caused by the curved capillary surface.

2.2.2 Filling of Capillaries with Lamellar Liquid Crystal

Pyrex® glass capillaries (100 mm length, 0.05 mm ID, 0.08 mm OD) were cleaned with chromic acid, rinsed with deionized water and dried at 180°C. After washing with toluene (distilled from Na metal), the tubes were silanized by exposure to 1% octadecyl trichlorosilane in toluene for 10 minutes. Following a final rinse with toluene, the capillaries were dried at 180°C for several hours.

The lead oleate (Pfaltz and Bauer) was used as received. The sodium caprate based (ICN Biomedical) lamellar liquid crystals were produced by mixing by weight: decanol (42%), sodium caprate (28%), and water (30%). Liquid crystal/microtubule mixtures were made by substituting the nickel-coated microtubes in water for the 30% water fraction.

The capillaries were filled with sodium caprate based or lead oleate based liquid crystals and microtubule mixtures by heating the liquid crystal and the glass capillary to 65-70°C.

2.3 Results and Discussions

2.3.1 Microtubules Dispersed in Smectic A Liquid Crystals

Figure 2.4a shows the dispersion of nickel coated microtubules in the K24 liquid crystal which is in the isotropic phase (T>40.5°C). A close examination of this picture yields several features which deserve comment. The microtubules are highly dispersed with little or no interaction with other tubules, perhaps because of the surfactant action of the K24. Secondly, circular features are seen throughout the field of view (as well as in the other pictures shown in this report). These are due to a problem in the camera optics and therefore should be ignored. This problem is currently being corrected.

Figure 2.4b shows the image through crossed linear polarizers of dispersed nickel coated microtubules in the K24 which is in the smectic A (S_A) phase (21.5<T<33.5°C). The sample is placed between a glass slide and cover slip. The dark background in this figure indicates that the S_A phase is homeotropically aligned between the glass slides. However, the microtubules significantly perturb the liquid crystal alignment in their immediate vicinity. The visible evidence of this is the series of bright fringes directed along the tubule axis, especially for microtubules oriented at 45° to the polarizer or analyzer. When the tubule long axis is oriented at a much smaller angle to either the polarizer or analyzer, the fringes are much less apparent. The fringe pattern terminates abruptly at the tubule terminus indicating a very sharp transition to the overall orientation of the matrix liquid crystal. Because of the small depth of field in the optical microscope, there is also some effect of the tubule position relative to the focus position. This is especially evident around the tubule on the right side of Figure 2.4b which brightens at an intermediate position along the optic axis of the microscope.

An isotropic zone around the tubule in a homeotropically oriented matrix (relative to the glass coverslips) would be equivalent to a cylindrical region of homeotropically oriented liquid crystal immersed in an isotropic matrix. The micrograph does not support an isotropic orientation of the liquid crystal molecules around the tubule since no orientation angle dependance of the fringe

pattern would be expected. Of course nothing can be surmised about the orientation of the liquid crystals within the tubule. But the very abrupt termination of reorientation influence at the tubule terminus suggests that the internal orientation would not be very important for determining overall tubule orientations.

It is well known that the maximum rotation of the polarized light into the analyzer will occur when one of the principal axes of the polarization ellipsoid of the molecule is oriented at 45° to the polarizer. This suggests that the K24 molecules are either oriented parallel or perpendicular to the surface.

2.3.2 Nematic Liquid Crystals in Capillary Tubes

Figure 2.5 shows a sequence of pictures of a nematic K24 liquid crystal filled 50-μm Pyrex® capillary as it is rotated between crossed linear polarizers. These photographs are in agreement with similar work done using the nematic liquid crystals, methyoxybenzilidene butylaniline (MBBA). With the capillary both perpendicular (Figure 2.5a) and parallel (Figure 2.5b) to the analyzer, one observes a flickering speckled pattern due to Rayleigh scattering throughout all of the sample except the center which is dark. The region next to the inner capillary walls has a very low intensity (which is very difficult to see in the photograph) indicating that the director is oriented perpendicular to the surface. This results in no rotation of the polarized source into the analyzer and thus extinction since the light polarization is directed along one of the principal axes of polarization. As we move radially inward from this region, there is a region of high light intensity due to rotation of the polarized light into the analyzer. In the center region there is complete extinction of light.

If the sample is rotated 45° to the polarizer, the light intensity pattern in Figure 2.5c is seen. This pattern is essential and opposite to that seen in Figures 2.5a and 2.5b in that the surface aligned and center regions are now rotated into the analyzer by the polarizer and the only two small regions on both sides of the center structure exhibit extinction.

This three region pattern indicates that liquid crystal alignment is homeotropic at the surface and gently curves to homogeneous alignment in the center. The two extinction lines seen in Figure 2.5c correspond to the region in the bend which is at 45° to the homeotropically and homogeneously aligned regions. This is shown schematically in Figure 2.5d.

Figure 2.6 shows a sequence of pictures of a nematic K24 liquid crystal filled capillary as it is rotated with parallel linear polarizers. These photographs are in agreement with similar work done using the nematic liquid crystal, MBBA. In comparison to the figures obtained from crossed polarized light, Figure 2.5, the regions of dark and light regions are essentially equivalent at 45°. For example, in Figure 2.6c the capillary is 45° to the direction of both the analyzer and polarizer and as three regions. The region next to the capillary wall is dark. This indicates that the polarized light is being rotated away from the analyzer and thus this region is aligned perpendicular to the surface. The second region towards the center has a high intensity and thus corresponds to the region in which there is curvature of the liquid crystal director. The center region is dark which means that there is rotation from the analyzer and thus the polarized light is extinguished.

2.3.3 Smectic A Liquid Crystals in Capillary Tube

Figure 2.7 shows a sequence of pictures of a smectic A K24 liquid crystal filled capillary as it is rotated between crossed polarizers. With the capillary parallel to the polarizer (Figure 2.7a), the region next to the wall is dark (not visible in photograph) indicating the S_A is aligned homeotropically to the surface. This is the expected result for a silanized capillary wall. Closer to the center a narrow fringe pattern is seen when the capillary is oriented parallel or perpendicular to the analyzer.

Rotation of the capillary 45° to the polarizer results in the entire sample becoming bright (Figure 2.7c). This is due to the rotation of the polarized light source into the analyzer across the diameter of the sample.

Figure 2.8 shows a sequence of pictures of a K24 filled capillary in the S_A phase as it is rotated with parallel polarizers. With the capillary long axis perpendicular to the polarizer (Figure 2.6a), the light intensity minimizes at 1/2, and 3/4 the diameter of the capillary when the microscope is slightly overfocused from the diametric plane; a bright line is seen at the center of the capillary. This contrast reverses when the microscope in underfocused. When the capillary is rotated 90°, the contrast for the most part vanishes. At 45°, the whole field within the capillary appears the darkest with the most obvious fringe pattern for both focus conditions. All of these effects are consistent with the capillary acting as a cylindrical lens containing an axially symmetric void.

The refractive index along the major axis of the liquid crystal is $n_e = 1.6971$, while the mutually equivalent perpendicular directions have an index of $n_o = 1.5142$. The glass capillary and the refractive index matching fluid have a refractive index close to 1.46. When the light is polarized perpendicular to the capillary axis, the cylindrical lens effect is the strongest. Little or no lens effect is seen when light is polarized parallel to the cylinder. These results are consistent with a homeotropic orientation of the liquid crystals with the large refractive index directed perpendicular to the capillary axis.

2.3.4 Microtubule Orientation in Smectic A Filled Capillaries

Nickel coated phospholipid microtubules have been dispersed in the K24 liquid crystal as described above and introduced into the glass capillaries. As shown in Figure 2.9, when the liquid crystal is in the S_A or is cooled slowly through the S_A state into the crystalline state, the majority microtubes become aligned in the disclination in the center of the capillary. The remainder of the microtubes can lie off center in either the bend or homeotropic regions. When this is the situation, microtubule alignment appears to be random with respect to liquid crystal alignment and surprisingly does not lead to defects in the radial nature of the crystalline structure or in the location of the central disclination. The microtubules also appear to be highly fragmented and at higher concentrations at the mouth of the capillary. Similar central tubule alignments have been seen in 12-μm ID capillaries.

To examine some of the factors which influence whether a given microtubule will become aligned during the filling and cooling process, the capillary was filled while the liquid crystal is in the isotropic, nematic, and smectic phases. The first observation that can be made is that there is a much higher number density of microtubules when filling is done from the isotropic state than

the nematic or smectic. In addition, there is a greater tendency towards clumping in the isotropic state. This suggests that the lower viscosities of the more disordered states enable greater flow of the microtubules and thus a greater tendency to enter the flow restrictive capillary. The observation of a more sparse population of longer microtubules in the center of nematic filled capillary, when compared with isotropic filled capillaries, is consistent with this view. Longer tubules might be preserved by the shock buffering effect of the more viscous nematic state which cushions the microtubule from turbulent flow breakage.

The problem of low microtubule density in a capillary filled in the smectic prevents it from being a viable process. When filling is done in the less viscous isotropic state, there seems to be a high incidence of microtubules sticking to the capillary wall. This seems to be a permanent condition and thus prevents the desired disclination centering from occurring. Therefore, we may conclude that the nematic phase is the best phase for the liquid crystals during filling. This allows for an intermediate viscosity which is necessary to protect the microtubules from breakage and for a high number density. In addition, the resistance to flow in center is at minimum due to the tendency of the liquid crystals to align parallel to the capillary walls as well as to the direction of flow.

An interesting phenomena occurs once the capillaries are filled and cooled into the smectic phase ($21.5<T<30.5°C$). Under these conditions, the microtubes are mobile within the central disclination and can be moved back and forth by pressure changes at the capillary entrance. However, when the liquid crystals are in the crystalline state, which essentially a frozen S_A, the microtubes are locked into a fixed and centered translational position.

2.3.5 Flow and Its Effect on Microtubule Orientation

A 50 μm capillary was filled with microtubules/K24 at an isotropic temperature and two syringes were attached as described in Figure 2.10 to observe the effect of flow on microtubule orientation at smectic, nematic and isotropic temperature conditions.

One syringe was removed from the previously described set-up which then allowed less restricted flow of the microtubule/K24 through the capillary. Figure 2.11a and 2.11b show rather long microtubules flowing down the center of a capillary filled with a homeotropically oriented nematic.

Figure 2.12 is a series of photographs of a short, centered microtubule that were obtained as the capillary was heated from smectic to the nematic and then into the isotropic state. Although the microtubule was well centered in the smectic state (Figure 2.12a) and moved only along the capillary axis, flow in the nematic state induced a misorientation (Figure 2.12 b). Heating to the isotropic created turbulence in the liquid crystal and quickly destroyed the orientation of the microtubule (Figure 2.12c). This indicates that centering of microtubules would occur in the smectic upon introduction of microtubules into the capillary.

2.3.6 Effect of Capillary Entrance Conditions on Microtubule Orientation

A 50-μm ID glass capillary filled with liquid crystal was attached to a syringe and needle with epoxy and positioned next to the polarizing microscope so that the open capillary tip could be observed while immersed in a microtubule/K24 mixture.

Air bubbles were forced out with the syringe before entrance of the microtubule into the smectic A filled capillary was observed. The orientation of the smectic A changes drastically at the capillary entrance so that the stiff elastic direction along the molecular axis, perpendicular to the smectic lamellae, is presented to the tubules (Figure 2.13).

Figure 2.14 shows a long microtubule passing through the liquid crystal cap through the center of the capillary, while Figures 2.15 and 2.16 show the same situation with a analyzer and crossed polarizers in the beam.

An interesting feature of the liquid crystal flow pattern in the 50-μm ID capillary is the disruption of the smectic fringe pattern when liquid crystals are first drawn into the capillary (Figure 2.17a). This disruption lasts only a few seconds until steady flow is achieved. However, Figure 2.17b shows liquid crystal swirling out and around the nodes with minimal distortion of the fringe pattern when liquid crystal is blown out of the capillary.

Figure 2.18a shows microtubules entering the center and near the wall when drawn in under high flow rates. This behavior suggests that there could be multiple cap-like structures at the capillary tip. A schematic of this effect is shown in Figure 2.18b.

2.3.7 Sodium Caprate-Decanol-Water Lamellar Liquid Crystals (NaC)

NaC-filled capillaries showed good orientation when the capillary and liquid crystals were both heated to 70°C while filling. The filling of the capillary took place in the lamellar (D) region of the phase diagram since lamellar phase boundary is little affected by temperature up to 70 °C. Figure 2.19 (a,b,c) shows NaC filled capillary at room temperature as it is rotated in polarized light. The behavior is quite similar to that seen for the smectic A crystal in that a transparent field is seen when the polarizer is oriented parallel to the axis of the capillary. A center disclination line appears only when the angle between the capillary axis and polarizer is finite. A slight banding pattern (probably originating from defects) oriented perpendicular to the capillary axis also appears at finite polarizer-capillary axis angles. However, no time dependent "flickering" of the contrast, typical of the nematic state, was seen.

When the NaC-filled capillary was viewed through cross polarizers, a bright birefringent fringe pattern was seen at all orientations (Figure 2.20). The number of fringes observed for the alkane like lamellar system was much less than that observed for the K24 liquid crystal because of the estimated smaller birefringence of the former system ($\Delta = 0.05$). In any case the fringes are parallel to the capillary axis, indicating a homeotropic orientation. Unlike the K24 liquid crystals, no birefringence appears in a wide dark band along the capillary axis. Obviously, the central isotropic region is much larger in the lamellar liquid crystals. The perpendicular distortion banding also shows up more clearly in Figure 2.20b.

Figure 2.21 (a,b,c) shows the NaC as viewed with the analyzer and polarizer parallel to each other at room temperature. Again the nonbirefringent central band appears. The improved fringe contrast at 45° is similar to that seen for K24 filled capillaries.

Figure 2.22 (a,b,c) reveals that the homeotropic orientation starts to randomize at 32-33°C (growth of nonbirefringent regions), the magnitude of which increases as the temperature is increased up to 80°C. The liquid crystals regained complete homeotropic orientation upon cooling from 70°C. Total disorder (isotropic) is observed at 120°C. The presence of completely non-birefringent areas, which were probably isotropic solution phases, in the presence of homeotropically oriented lamellar material was unusual, considering that the sample was in the single phase, lamellar region of the phase diagram.

2.3.8 NaC-Microtubule Mixtures

A capillary tube was filled with NaC liquid crystals and epoxied to a 1 cc syringe so that fluid could be drawn into the capillary in a controlled fashion. The open capillary tip was immersed in a NaC:microtubule mixture which was sandwiched between a glass slide and a cover slip. Considerable amounts of liquid crystal adhered to the capillary under these conditions and this generated some background birefringence.

Upon drawing the fluid in at 65°C, we found that the presence of an interface such as an air bubble was sufficient to disrupt the homeotropic orientation (Figure 2.23). A highly birefringent lamellar phase is still observed however.

Farther away from the bubble defect, microtubules were seen oriented with their long axis parallel to the capillary axis (Figure 2.24). However, because of the rather large lateral extent of the isotropic defect zone at the capillary axis, some misorientation of the tubules appeared. Mobile tubules appeared only in the central isotropic region. Application and release of a slight pressure at the capillary opening resulted in flow of the tubules in the central region and then a slow back and forth, damped oscillation along the capillary axis.

2.3.9 Lead Oleate (LO) Crystals

Lead oleate is a low melting (T_m = 45°C) ambiphile that forms lamellar plastic states. We wished to see if a highly ordered, homeotropically, lamellar, oriented state could be produced upon cooling into the crystalline state at room temperature.

A glass capillary prepared in the same fashion as for the NaC ternary system was filled with LO at about 70°C. Upon cooling to room temperature, a considerable texture was noted under polarized light. Under crossed polarizers, at 45° rotation, a birefringence pattern reminiscent of the capillary oriented nematic state appears. However, "flickering" of the individual grains in the oriented bands is not apparent (Figure 2.25). Evidently, upon cooling to room temperature, the ambiphilic nature of lead oleate promotes orientation at the capillary surface during crystallization; however, a large number of defects are introduced into the oriented layer. Heating to increasing temperatures above room temperature reduces the birefrigence in the ordered bands until melting into an unoriented state finally occurs (Figure 2.26).

2.4 References

1) R. B. Meyer, Phil. Mag., 27, 405 (1973).
2) C. E. Williams, P. E. Cladis, and M. Kleman, Mol. Cry. Liq. Cryst., 21, 355 (1973).
3) C. Williams, P. Pieranski, and P. E. Cladis, Phys. Rev. Lett., 29(2), 90 (1972).
4) D. Melzer and F.R.N. Nabarro, Phil. Mag., 35(4), 907 (1977).
5) S. K. Lo, L. M. Galarneau, D. J. Rogers, and S. R. Flom, submitted 1991.
6) H. Lin and P. Palffy-Muhoray, 17th Midwest Solid State Theory Symposium, October 1989.
7) F. C. Frank, Farad. Soc. Disc., 25, 19 (1958).
8) A. J. Hurd, S. Fraden, F. Lonberg, and R. B Meyer, J. Physique, 905 (1985).
9) M. R. Kuzma, Phys. Rev. Lett., 57(3), 349 (1986).
10) C. Kang and A. Khan, J. Coll. Interf. Sci., 156(1), 218 (1993).
11) P. Ekwall and L. Mandell, Acta. Chem. Scand., 21, 1612, 1619, 1630 (1967).
12) M. Dubois, T. Gulik-Krzywicki, and B. Cabane, Langmuir, 9(3), 673 (1993).
13) S. E. Friberg, C. S. Wohn, and F. E. Lockwood, Macromol., 20, 2057 (1987).
14) J. Marignan, G. Malet, and O. Parodi, Ann. Phys., 3, 221 (1978); R. G. Horn and M. Kleman, Ann. Phys., 3, 229 (1978).

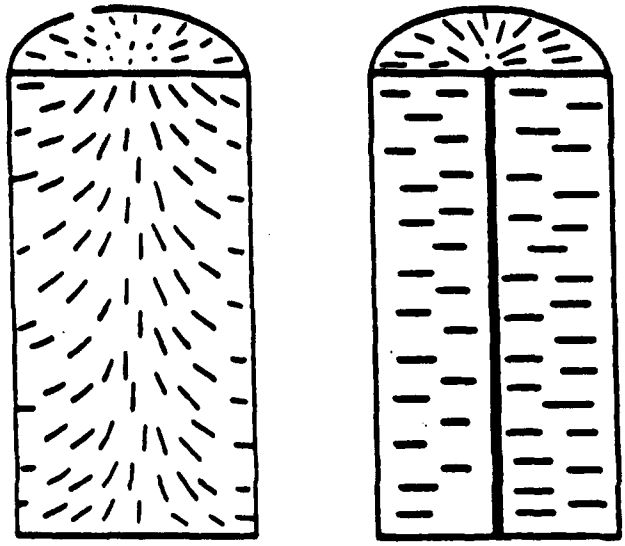

Figure 2.1 Morphology of homeotropically oriented nematic in a microcapillary with and without an inserted fiber.

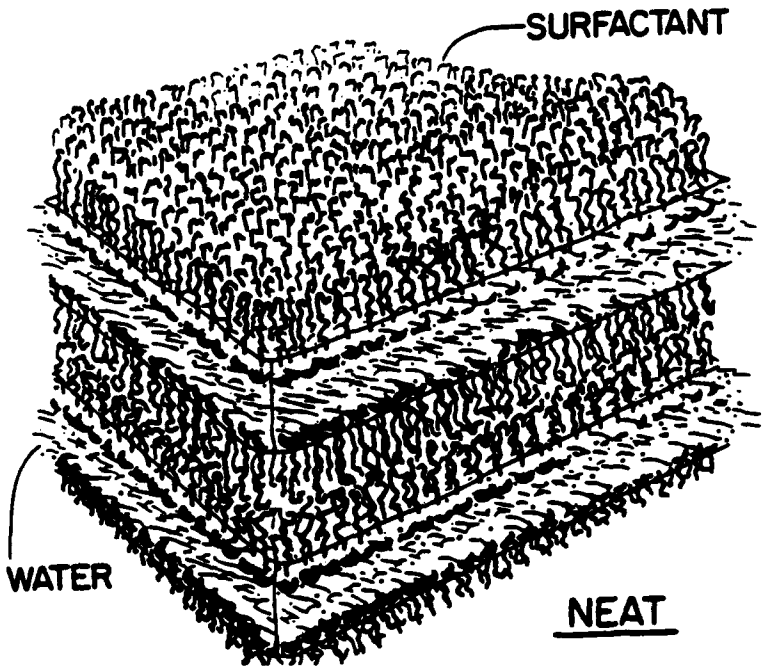

Figure 2.2 Microstructure of lamellar phase.

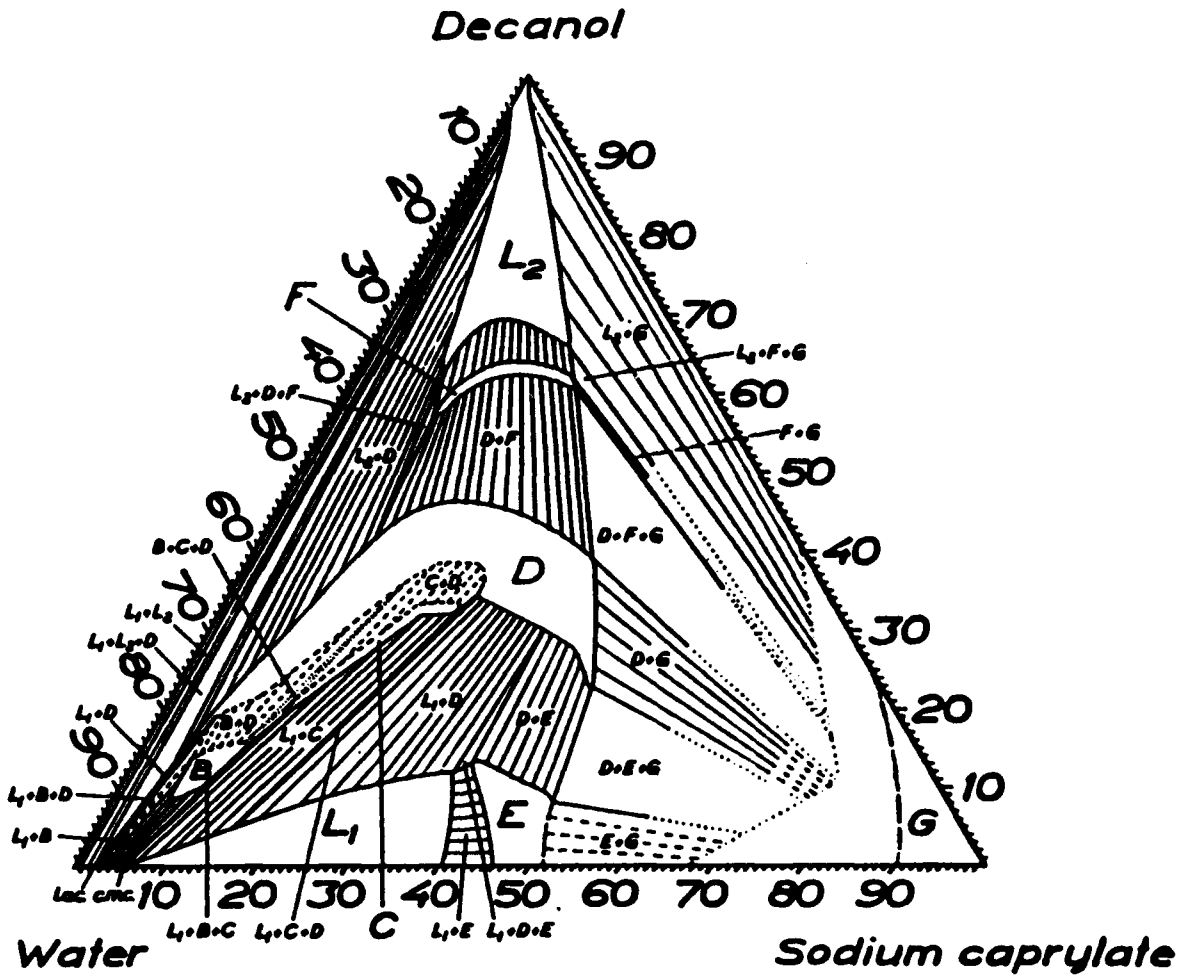

Figure 2.3 Phase diagram for the three component system sodium caprylate-decanol-water at 20°C. B-F regions with homogeneous mesomorphous phases; G region with solid substances; L_1 region with homogeneous isotropic aqueous solution; L_2 region with homogeneous isotropic decanolic solution.

(a)

(b)

Figure 2.4 Nickel tubules dispersed in K24; (a) parallel polarizers, isotropic state, (b) crossed polarizers smectic A static.

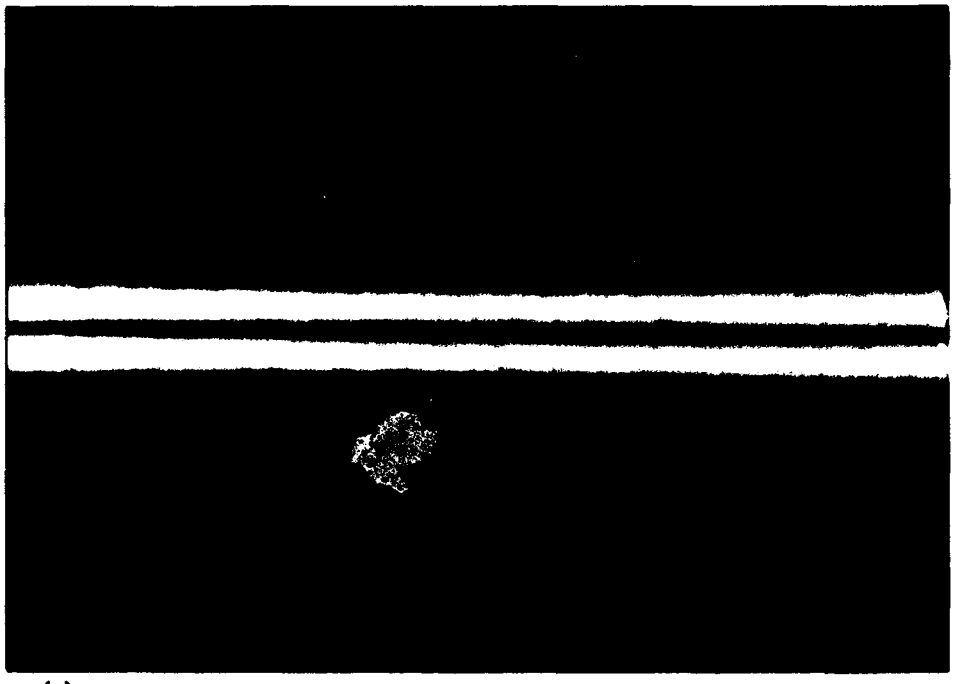

(a)

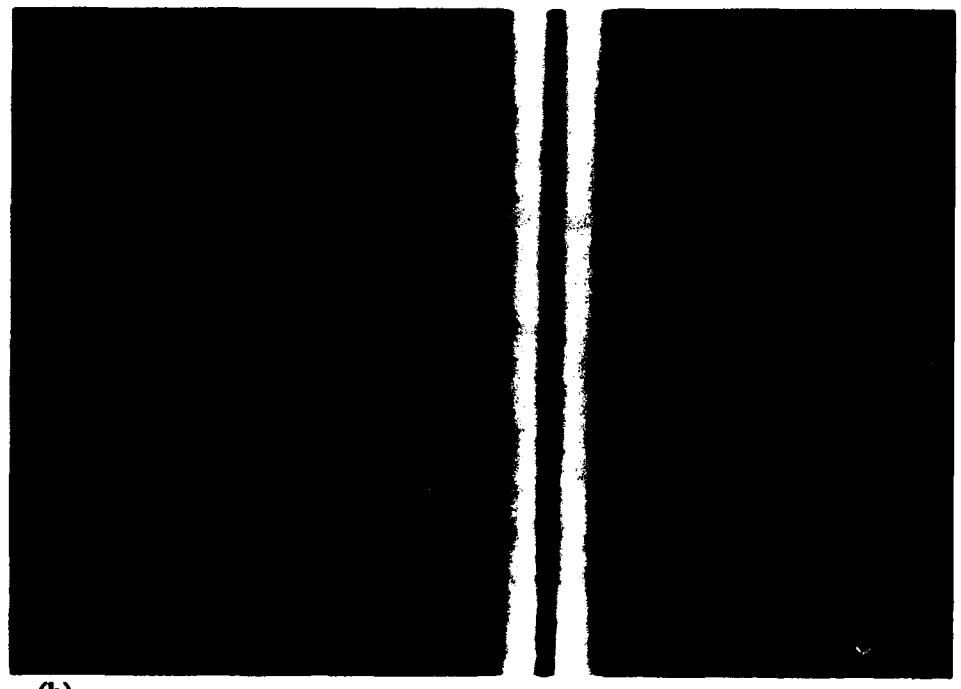

(b)

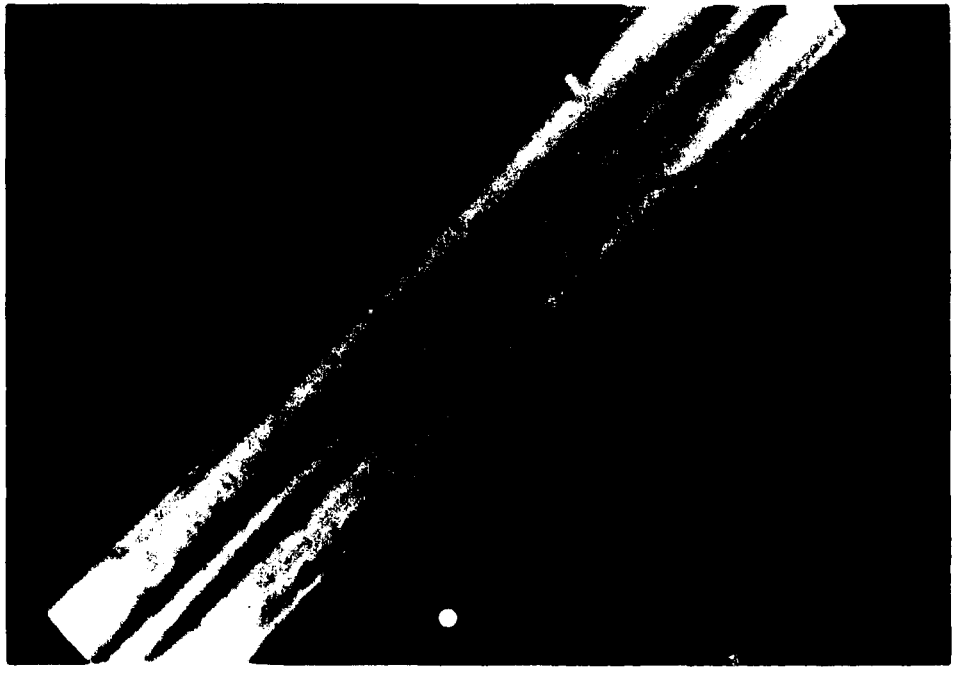

(c)

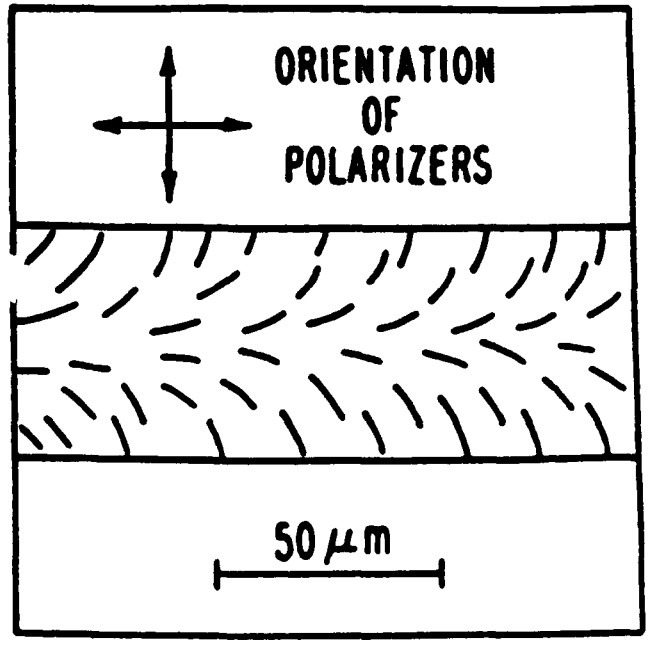

(d)

Figure 2.5 Capillary constrained nematic state (crossed polarizers). Capillary: (a) perpendicular, (b) parallel, (c) 45° to analyzer.

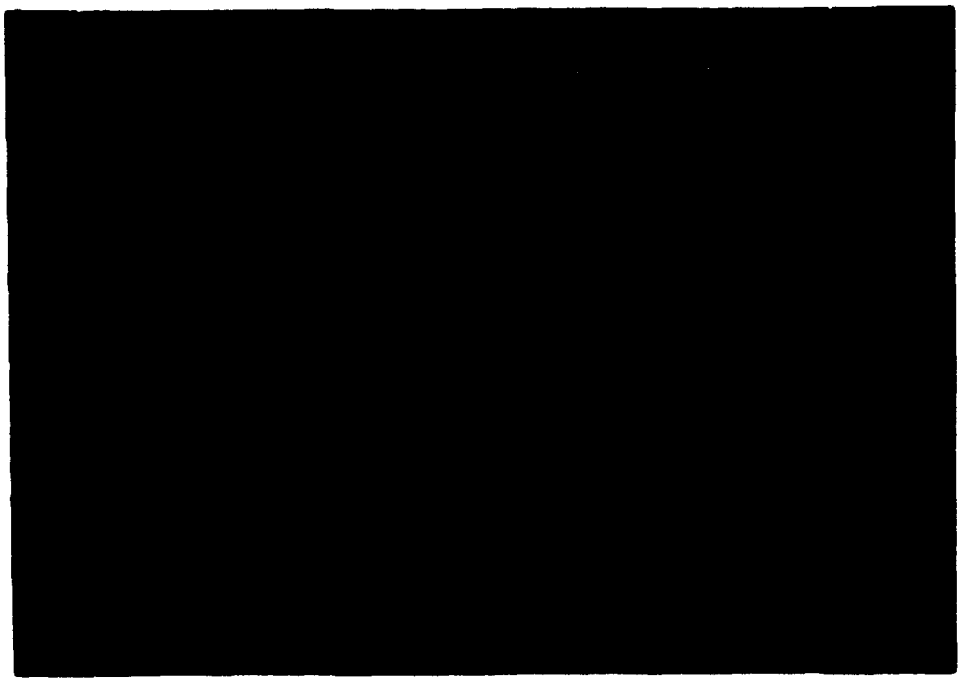

(a)

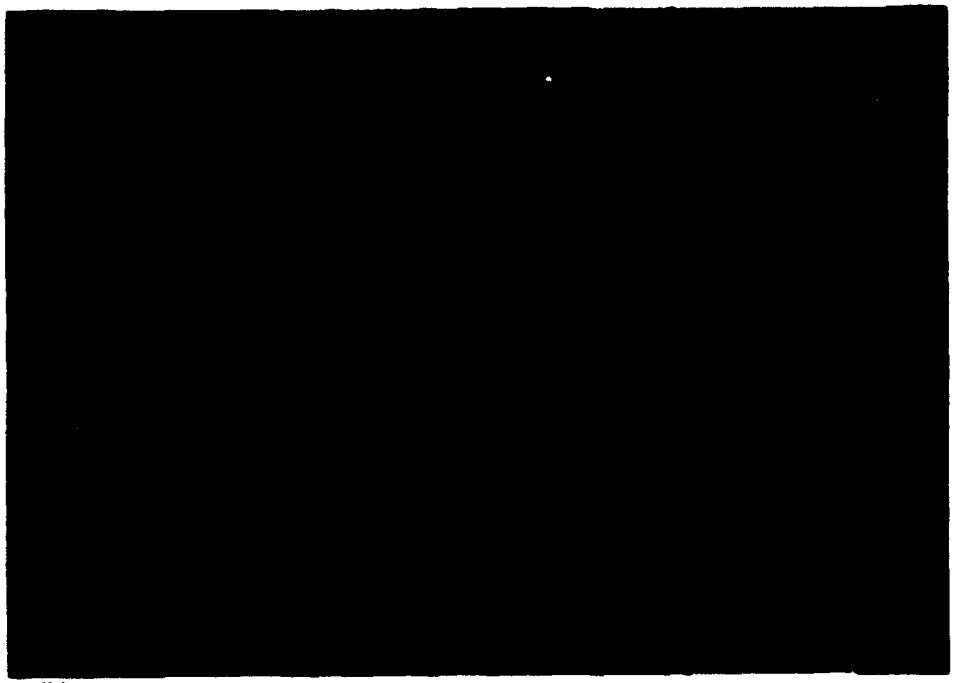

(b)

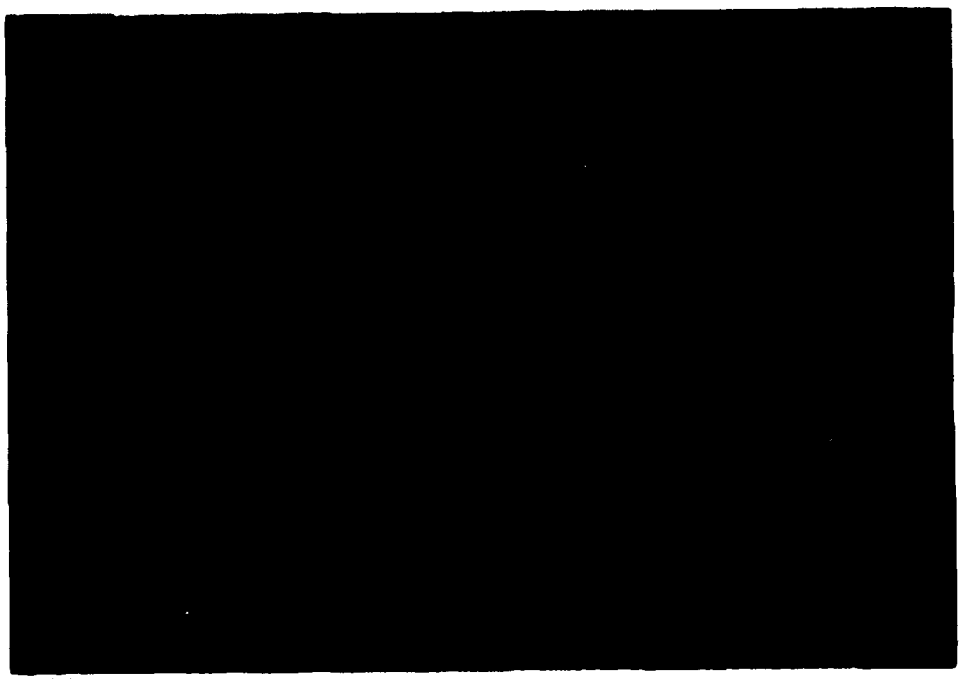

(c)

Figure 2.6 Capillary constrained nematic state (parallel polarizers). Capillary: (a) perpendicular, (b) parallel, (c) 45° to analyzer.

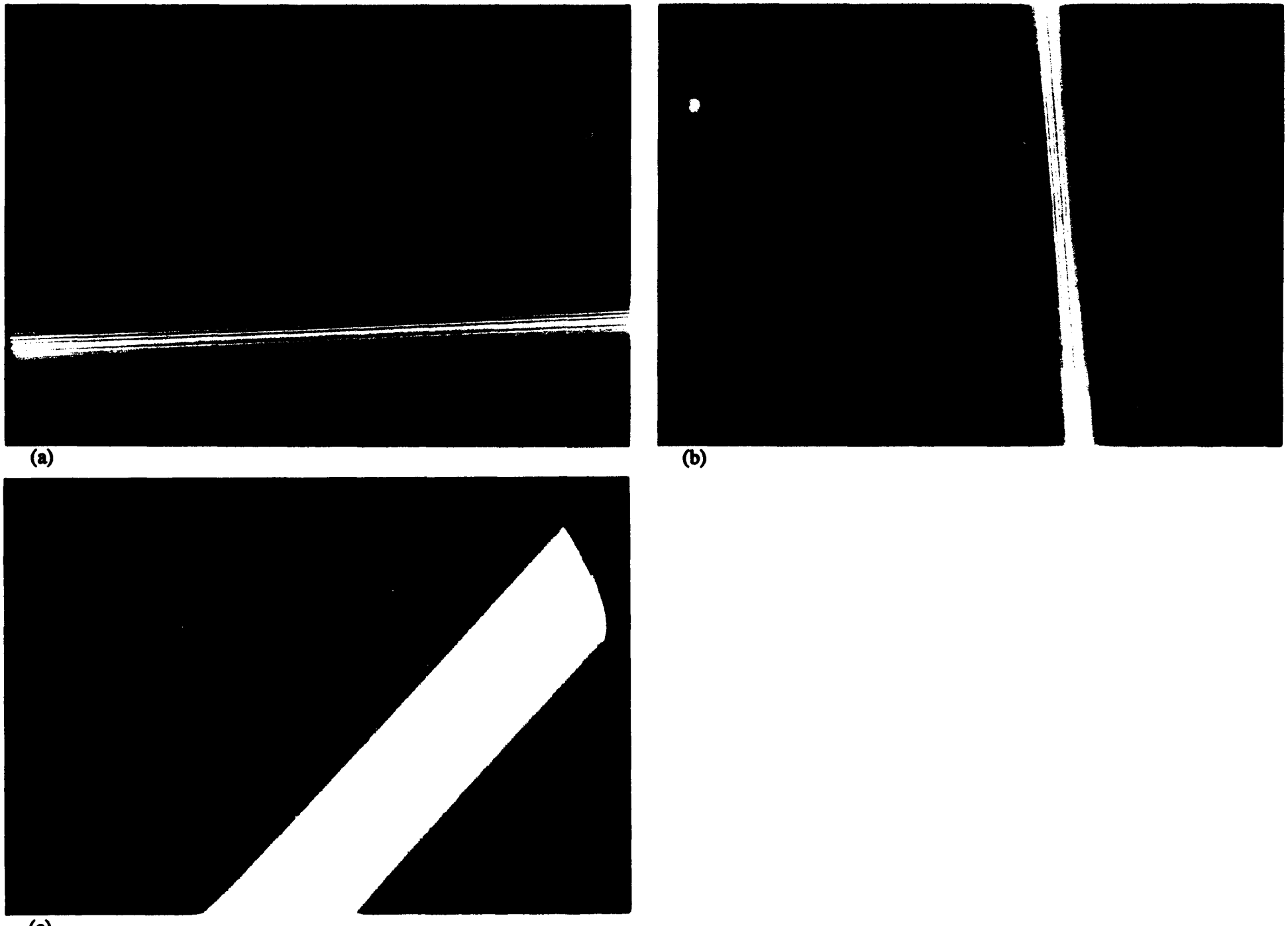

Figure 2.7 Capillary constrained smectic A (crossed polarizers). Capillary: (a) perpendicular, (b) parallel, (c) 45° to analyzer.

(a)

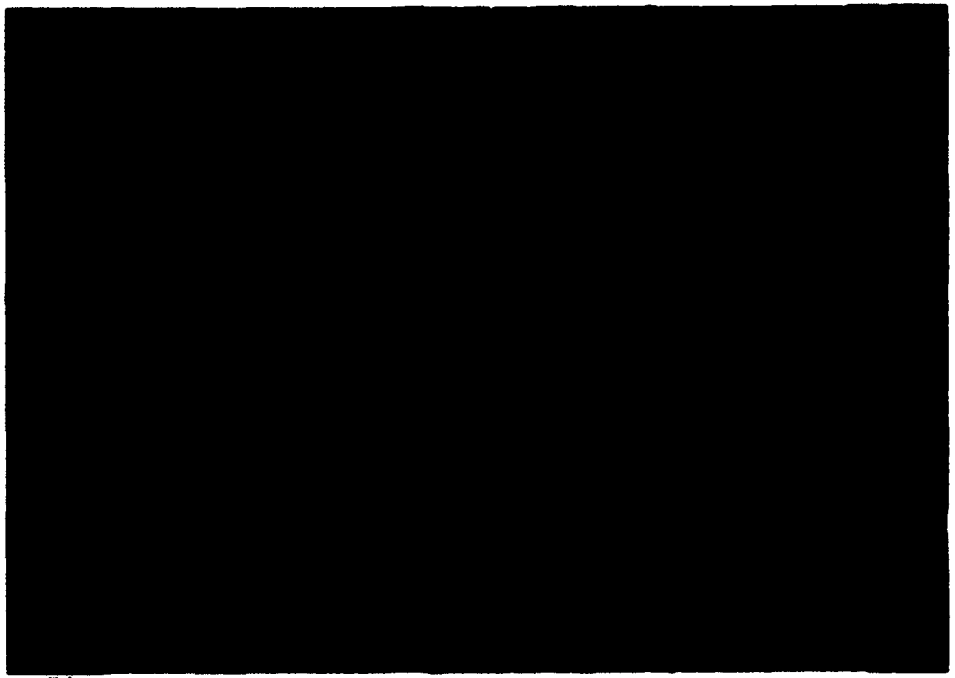

(b)

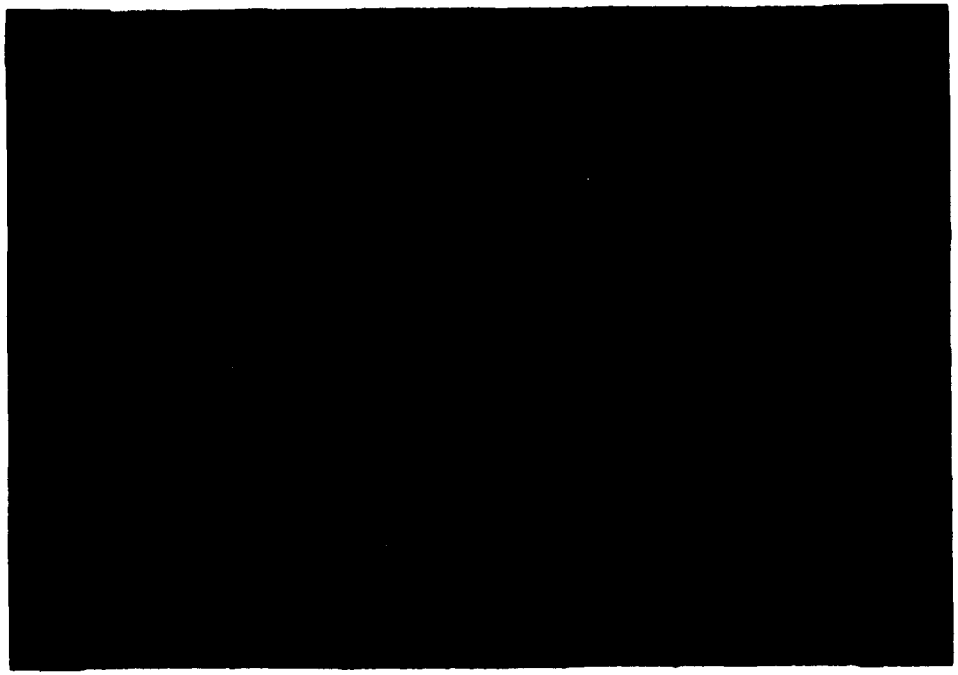

(c)

Figure 2.8 Capillary constrained smectic A (parallel polarizers). Capillary: (a) perpendicular, (b) parallel, (c) 45° to analyzer.

(a)

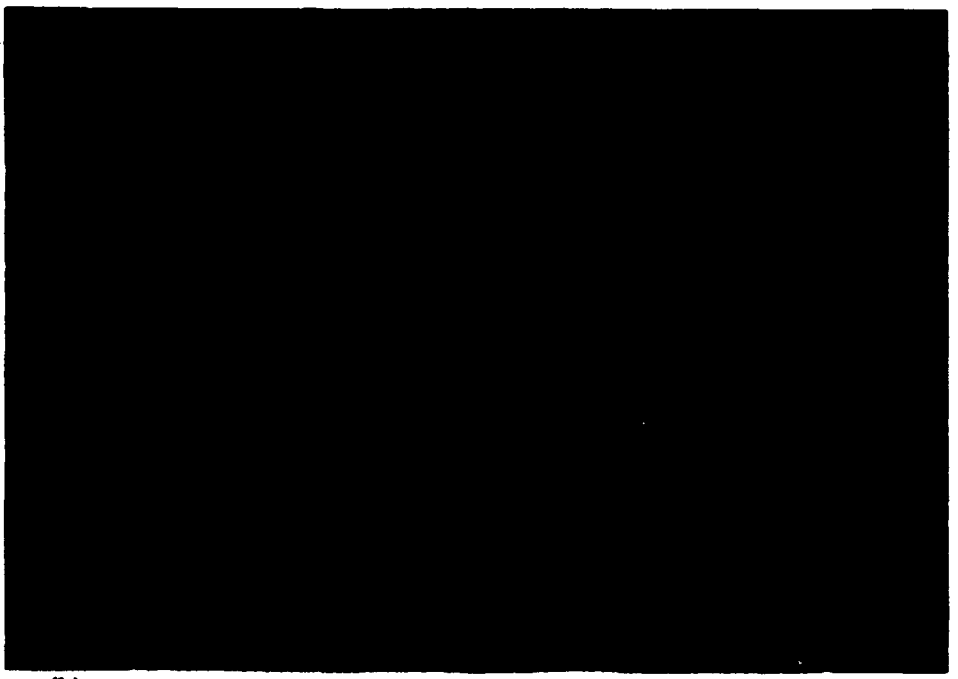

(b)

Figure 2.9 Nickel microtubules centered within 50 μm I.D. capillaries. K24 in smectic A. Parallel polarizers both horizontal in (a) and (b).

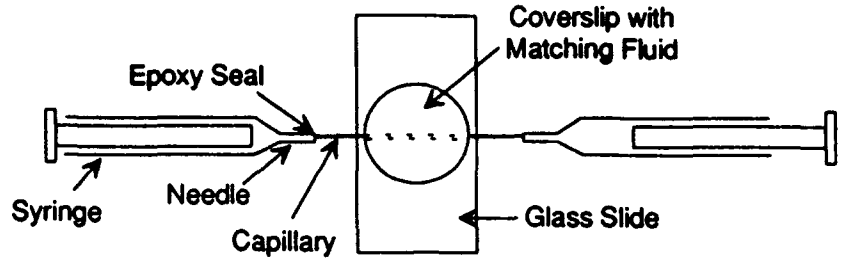

Figure 2.10 Device used for study of the effect of flow on microtubule orientations.

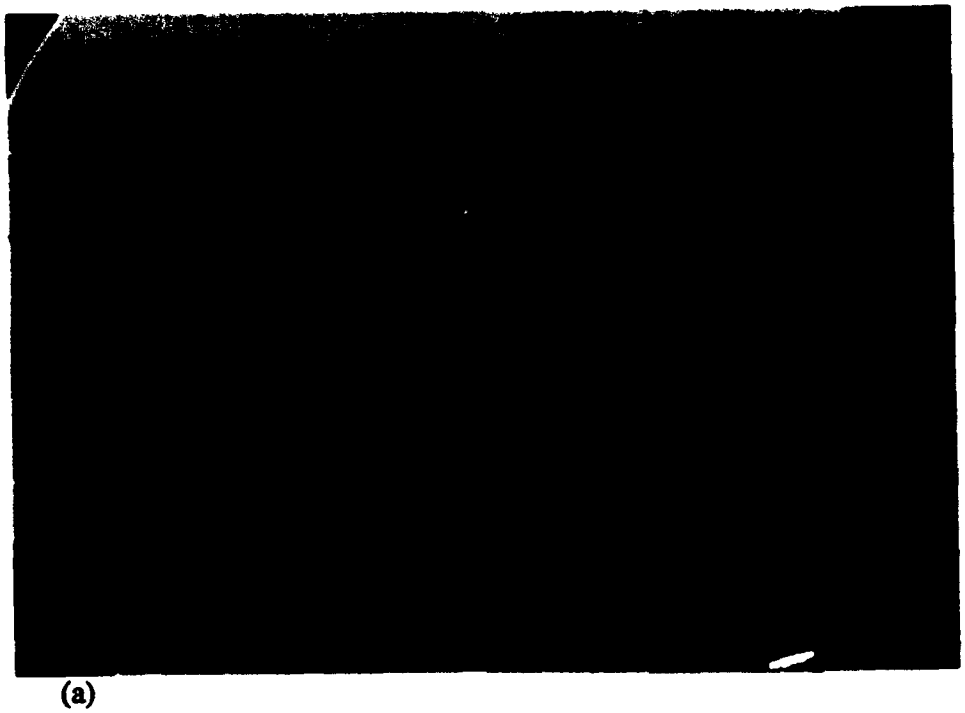

(a)

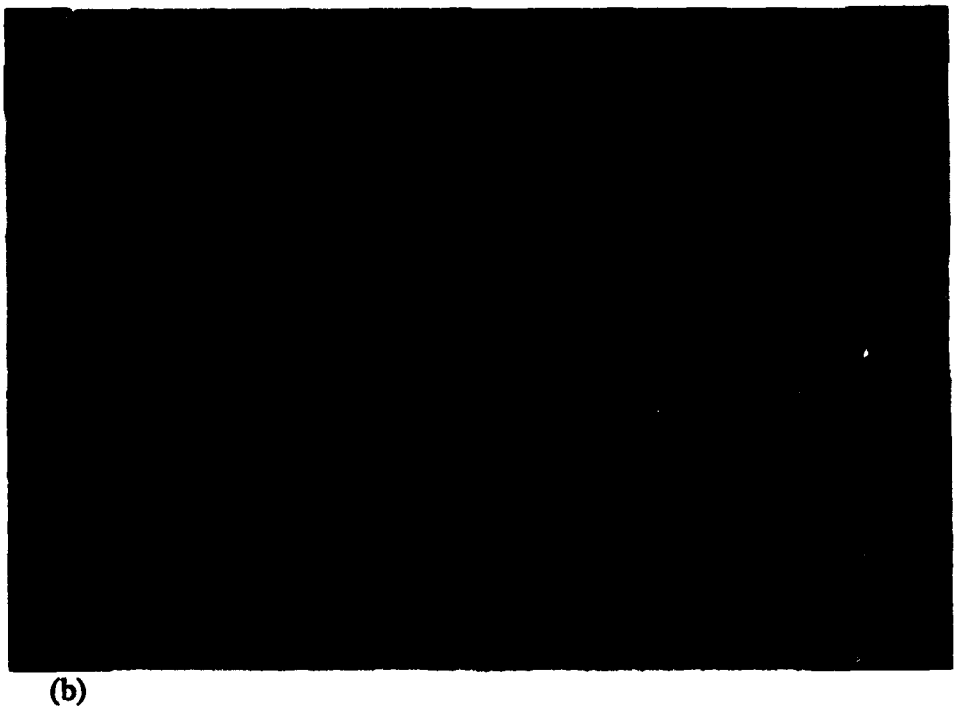

(b)

Figure 2.11 Microtubules flowing in homeotropic nematic liquid crytals in 50 μm I.D. capillaries: (a) before, and (b) after application of pressure. Filling from the nematic state.

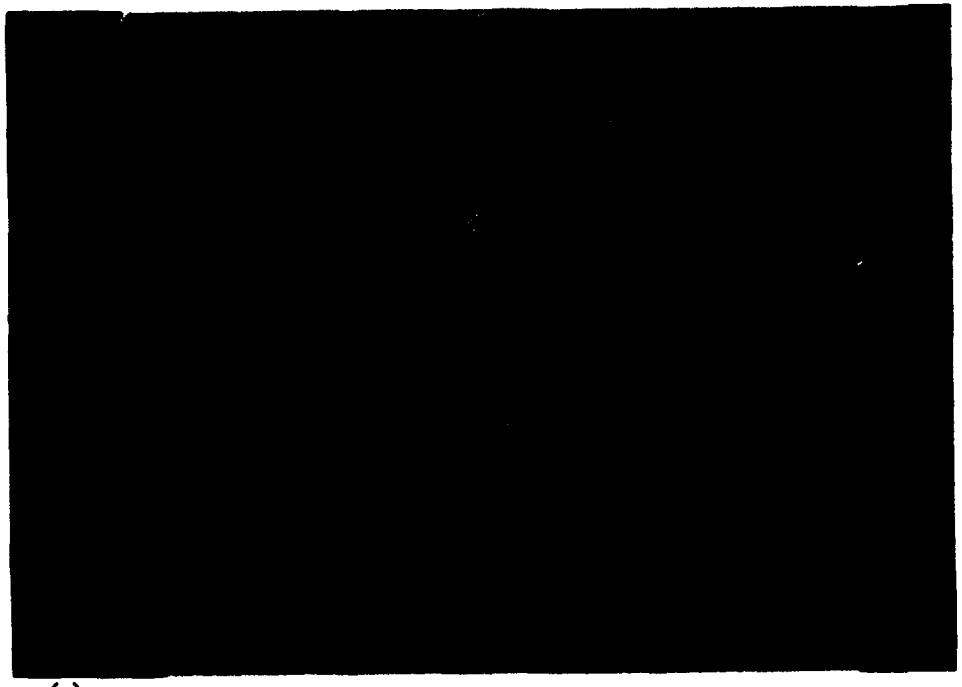

(a)

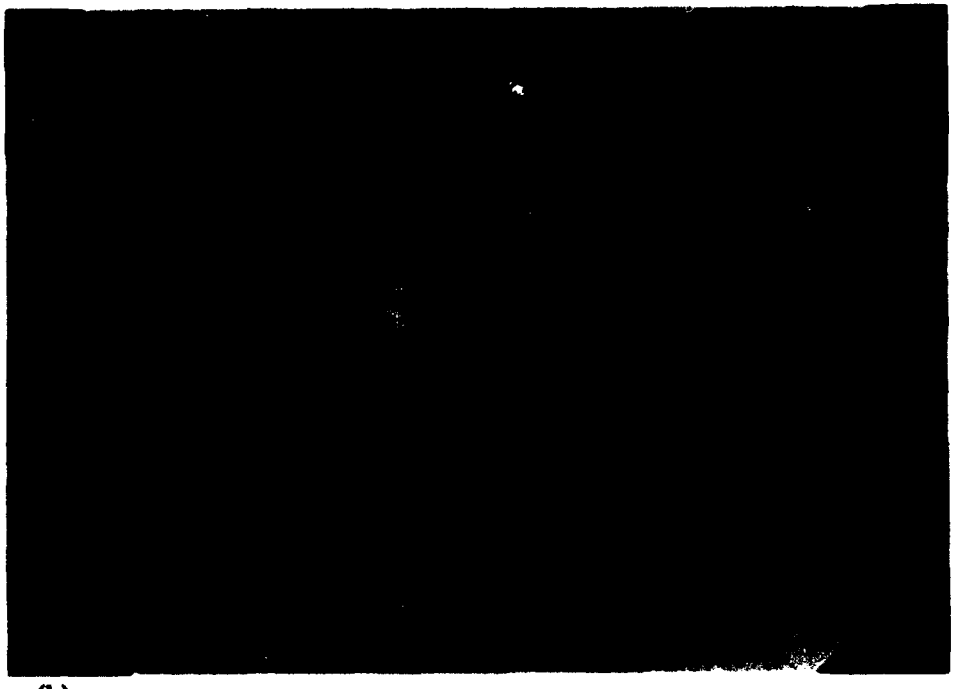

(b)

(c)

Figure 2.12 Flow misorientation of a tubule induced by transition from the (a) smectic, to the (b) nematic, to the (c) isotropic state.

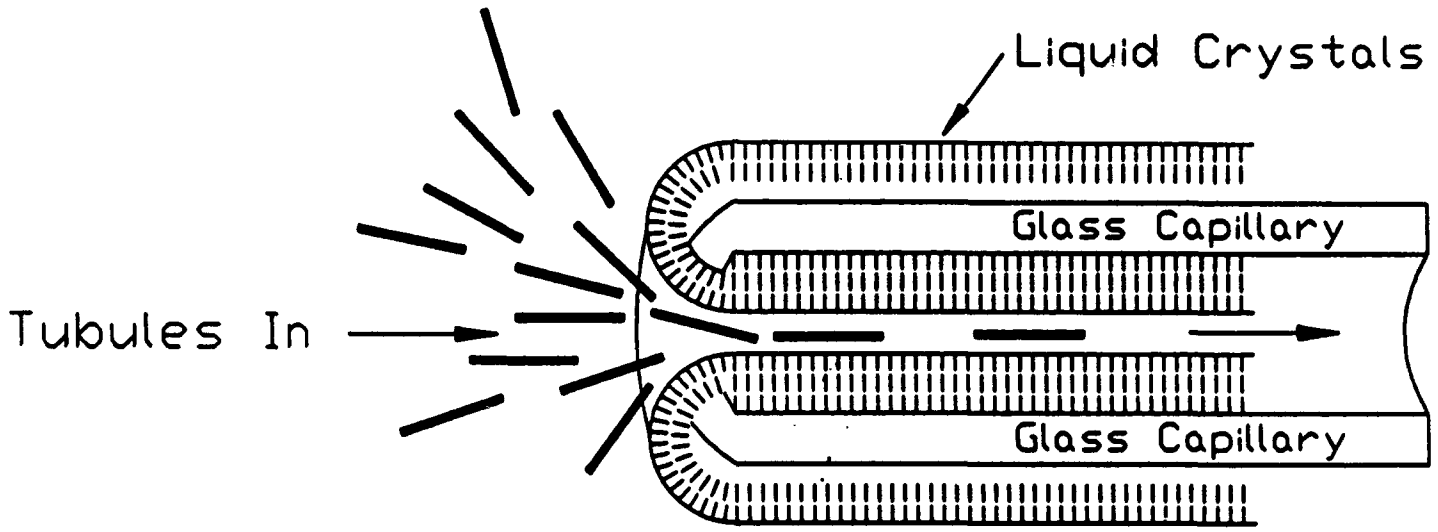

Figure 2.13 **Morphology at the capillary tip that promotes microtubule centering.**

Figure 2.14 Nickel microtubule entering through the center of the cap. smectic A with suction flow applied. Analyzer vertical.

Figure 2.15 Cap containing smectic A liquid crystal with no nickel microtuble. Analyzer vertical.

Figure 2.16 Cap containing smectic A liquid crystal with no nickel microtubule. Analyzer vertical. Crossed polarizers.

(a)

Figure 2.17a Distortions induced when high suction shear rates are applied to cap containing liquid crystal.

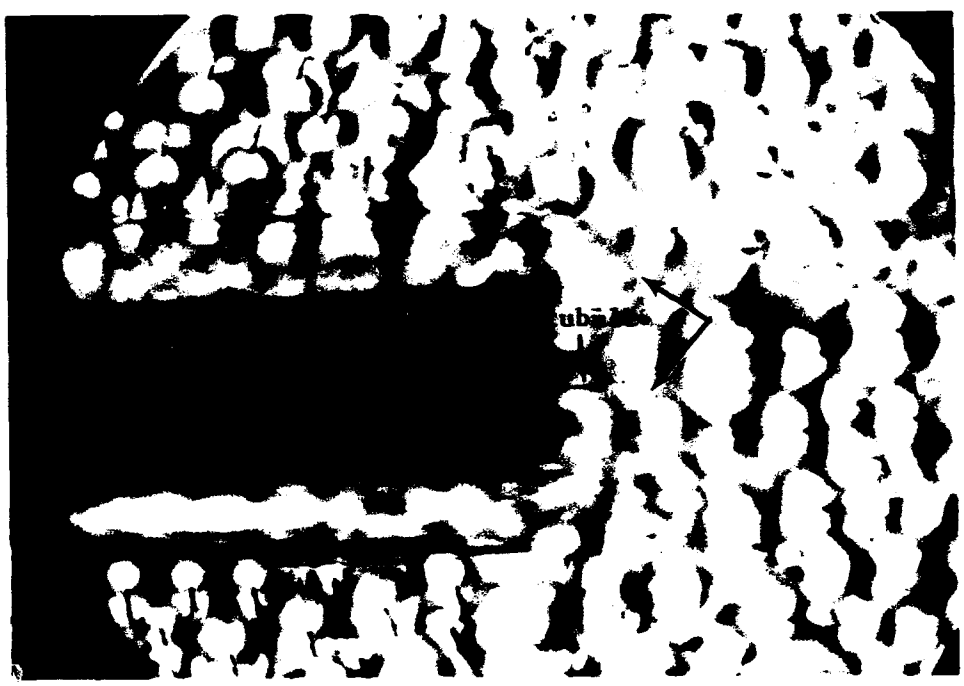

(b)

Figure 2.17b Microtuble shown exiting capillary as pressure is applied.

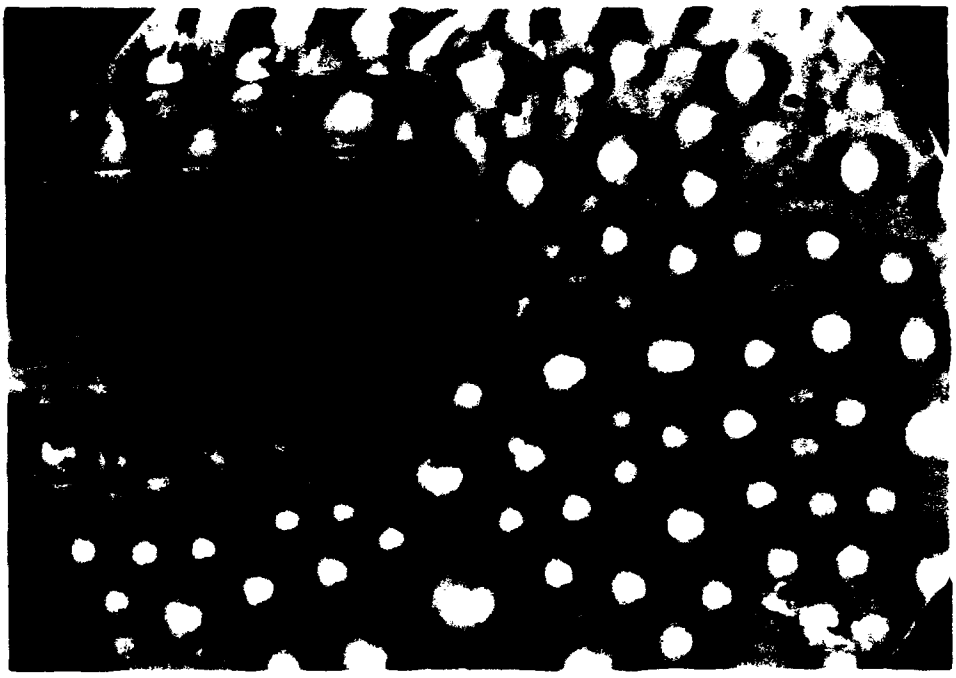

Figure 2.18a Microtubules entering along multiple entrance points.

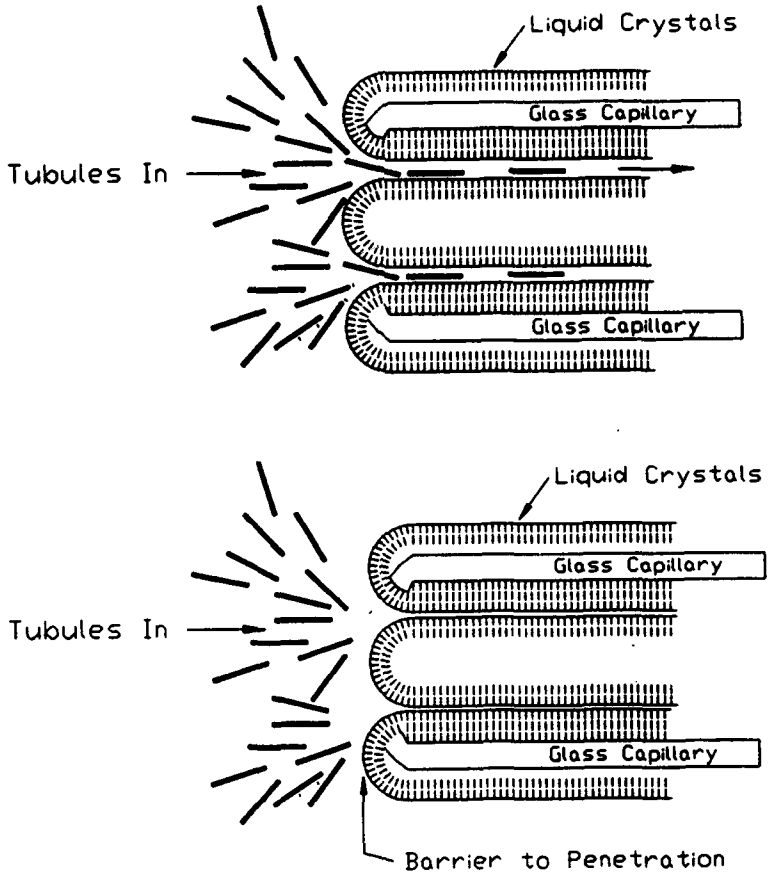

Figure 2.18b Schematic of multiple entrance points in the distorted region at the capillary tip.

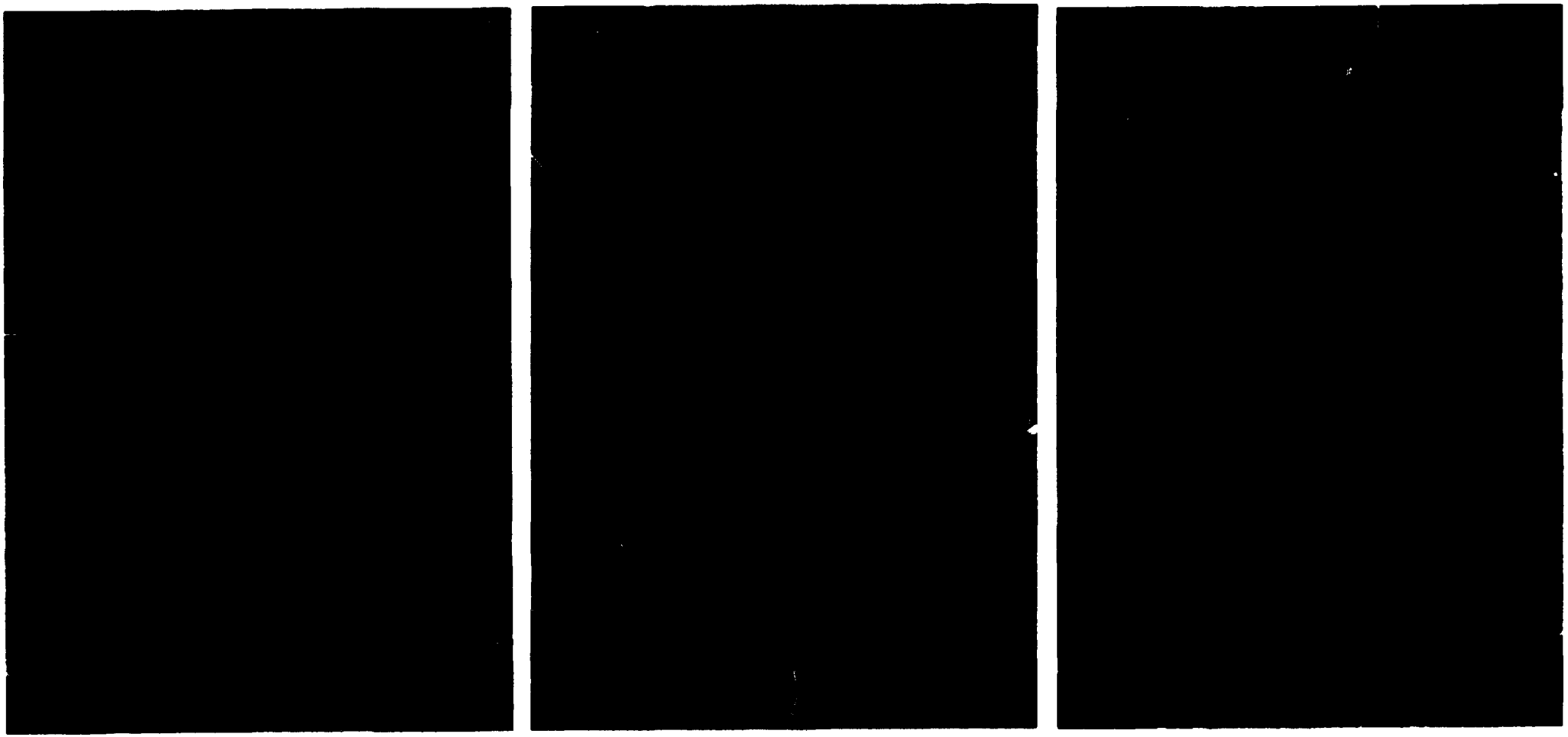

(a) (b) (c)

Figure 2.19 NaC at 24°C observed in light polarized in the vertical direction-no analyzer.

(a) (b)

Figure 2.20 NaC at 24°C observed in light polarized in the vertical direction-90° analyzer.

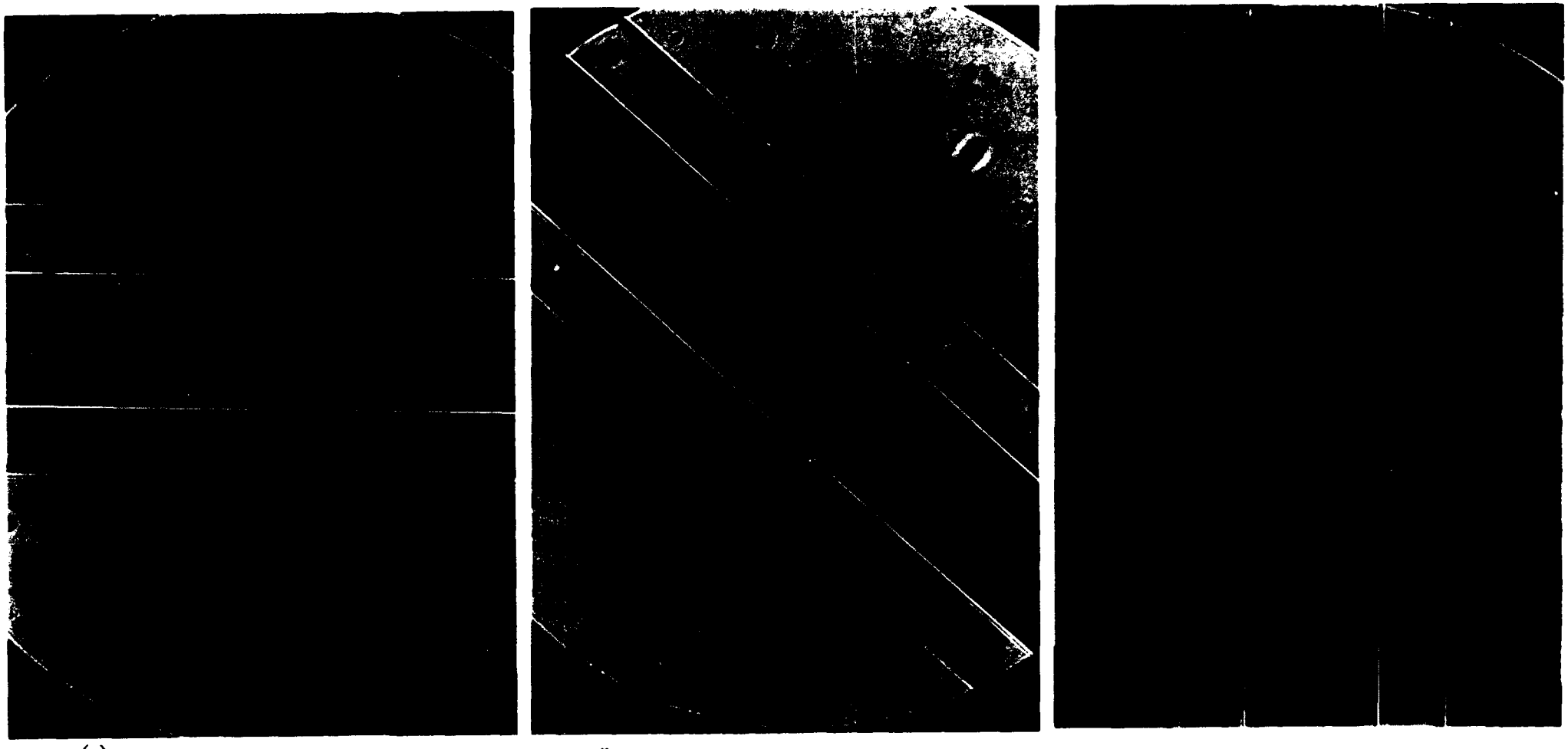

(a) (b) (c)

Figure 2.21 NaC at 24°C observed in light polarized in vertical direction-0° analyzer.

(a) 80°C (b) 50°C (c) 33°C

Figure 2.22 NaC at different temperatures in light polarized in vertical direction-90° analyzer.

(a) analyzer at 90°

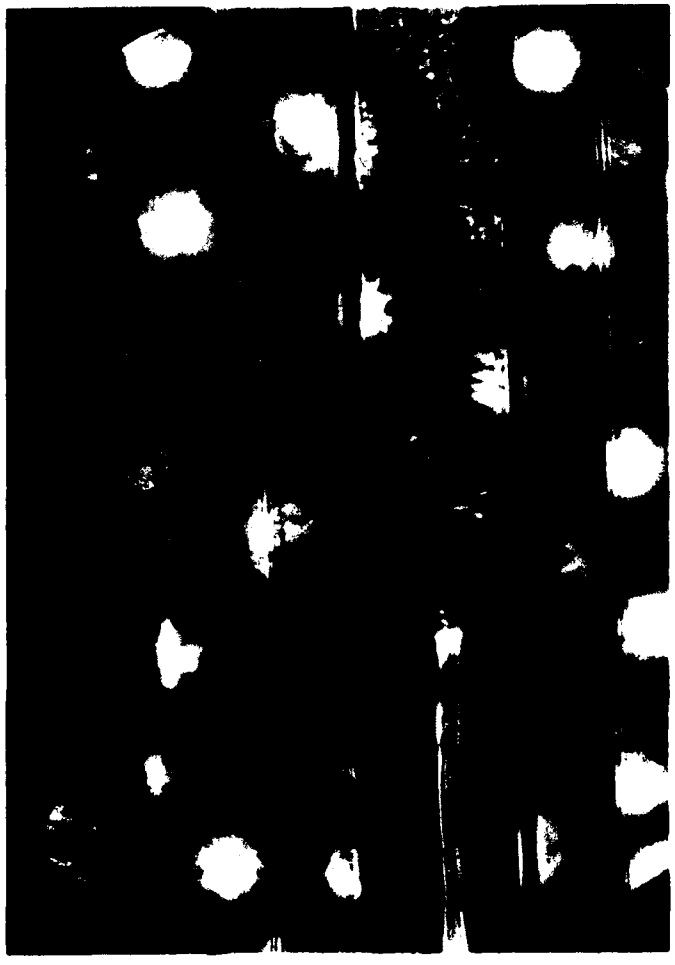

(b) no analyzer

Figure 2.23 NaCl at 65°C in the vicinity of bubble in light polarized in vertical direction.

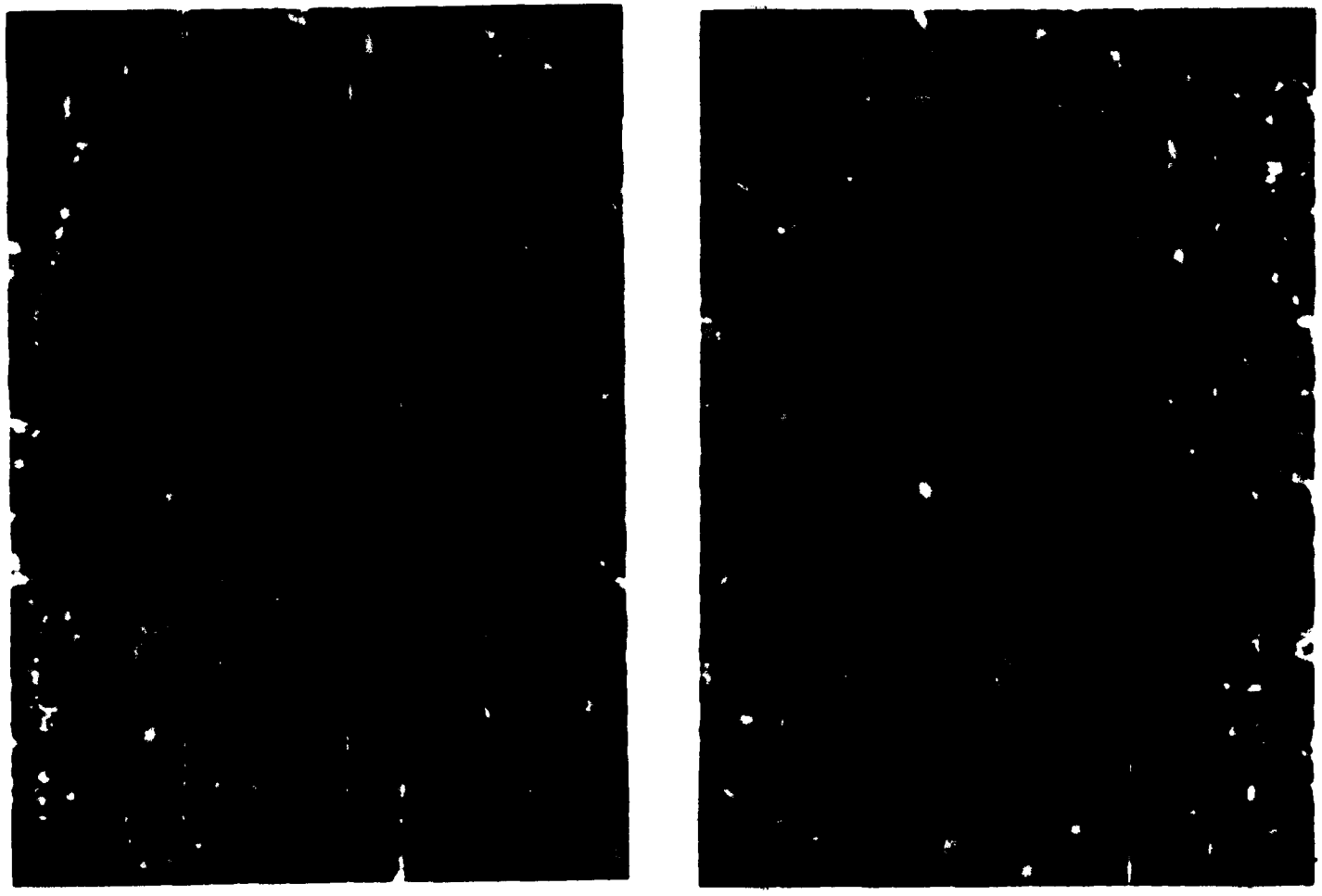

(a) (b)

Figure 2.24 NaC at 65°C showing oriented microtubules in light polarized in the vertical direction.

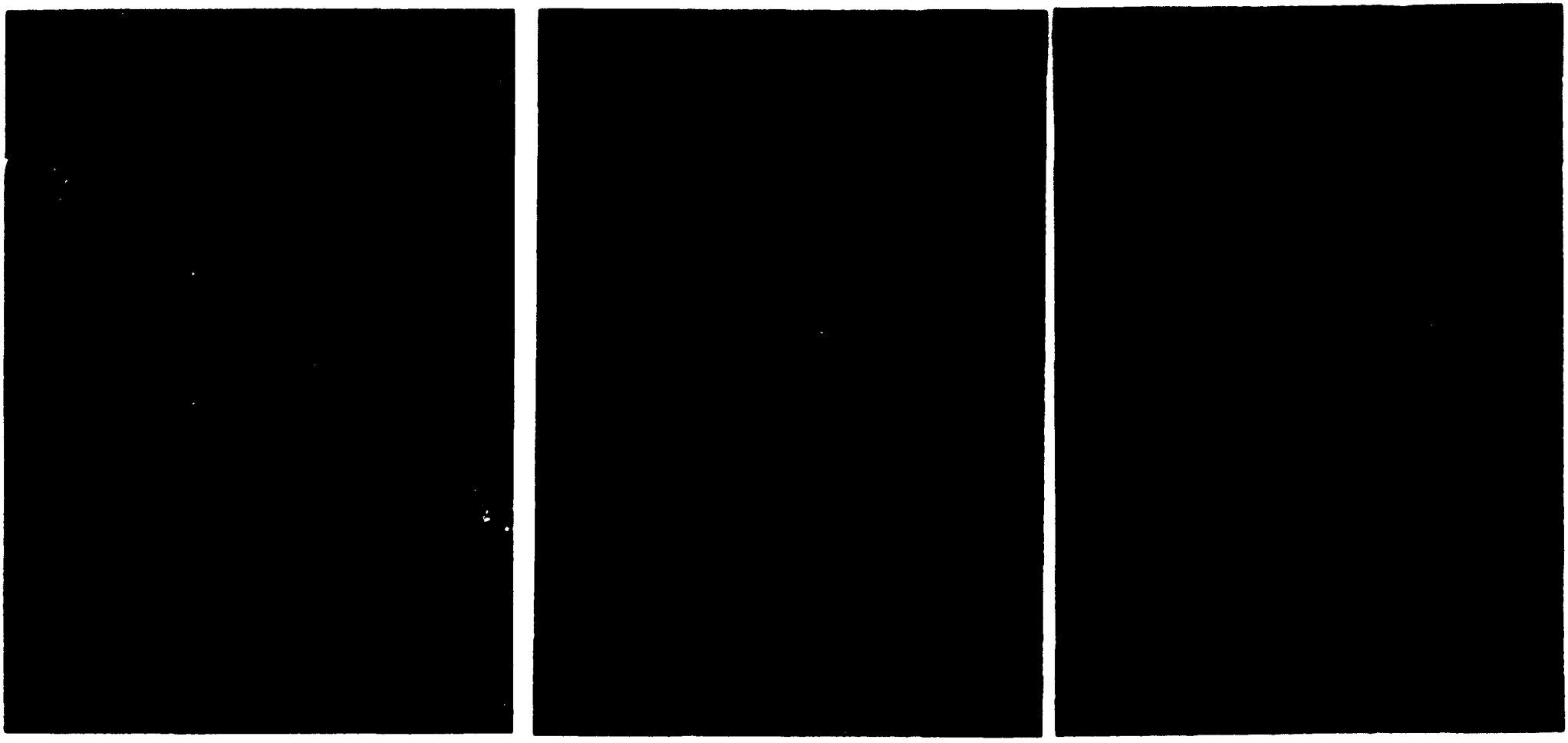

(a) analyzer at 90°

(b) no analyzer

(c) no analyzer

Figure 2.25 LO at 22°C in crystalline state. Light polarized in vertical direction.

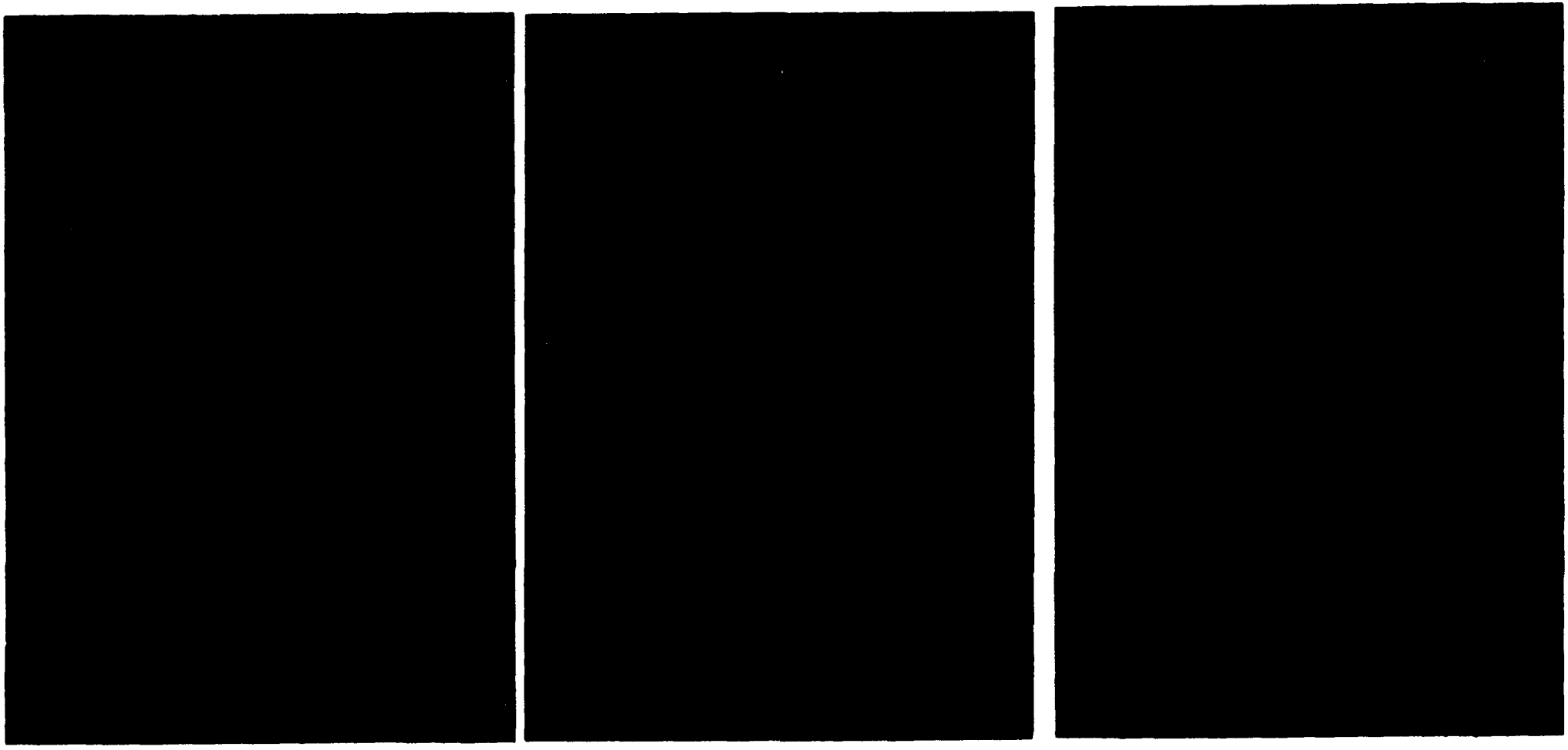

(a) 60°C, no analyzer

(b) 39°C, 90° analyzer

(c) 33°C, 90° analyzer

Figure 2.26 LO at various temperatures. Light polarized in vertical direction.

3. NONLINEAR MATERIALS DEVELOPMENT

3.1 $[(Ru(bpy)_2]_2$ ABPY (PF_6) and $[(Ru(bpy)_2]_2$ BPTZ (PF_6)

Water soluble di-Ru ABPY and di-Ru BPTZ crystals were prepared and purified with a modification of the published literature procedures. The near infrared band extinction coefficient was estimated to be approximately 20,000 M^{-1} cm^{-1} for both materials (Figure 3.1). The large extinction coefficient in the near infrared band is a sign of a large polarizability in the Ru-ligand bond. A strong NLO absorption is thus expected both pre- and post-resonant to this band. A large visibly transparent region is also a requirement for visible eye protection.

The thermal stability of the di-Ru ABPY complex was studied by measuring the change in absorbance at 503 and 752 nm with increasing temperature. No precautions were taken to remove air from the system. The temperature was increased at a rate of 1°C/min. The study showed that the complex is completely stable up to 112°C. This stability is important in view of the temperature increases that can be expected during pre-resonant absorption NLO measurements.

3.2 Coated Microtubules

The overall functioning of the microtubule based optical limiter is based on the use of a cylindrical, hollow semiconductor tube. The nickel-coated phospholipid microtubules developed by NRL serve as templates for the construction of these semiconductor microstructures. Unfortunately, the nickel coating provided by NRL is incompatible with the reagents and procedures used in the synthesis of the semiconductor layer. This is mainly due to the formation of NiSe and NiS during the coating of the tubules in the presence of hydrogen chalcogenides. Therefore, the nickel layer must by either covered or removed. We have elected to coat the nickel microtubules with gold followed by a layer of the II-VI semiconductor, CdSe. From the viewpoint of plasmon enhancement of II-VI semiconductor particle NLO, the ideal structure would be phospholipid-Ag-CdS. We have also employed the NRL method to grow our own tubules so that the II-VI semiconductor can be grown directly on the tubule. We have used scanning electron microscopy (SEM), transmission electron microscopy (TEM), electron diffraction, optical microscopy, and UV-Vis spectroscopy as tools to characterize our coatings.

3.2.1 Phospholipid Microtubule Synthesis

A solution of 5.0 grams of the phospholipid, $DC_{23}PC$, was dissolved in 400 mL of reagent grade ethanol. This solution was stirred and heated to 60°C for 12 hours in order to completely solvate the phospholipid. An additional solution consisting of 600 mL of distilled water and 1000 mL of ethanol was heated to 60°C. These two solutions were then mixed together and held at 60°C for 12 hours in order to assure thermal homogeneity. The solution was then cooled to 30°C and allowed to stand for 14 days.

After 14 days, the microtubules had formed and were dialyzed against 0.1 M HCl using dialysis tubing with a 50,000 molecular weight cutoff (WMCO). This step was necessary to remove unreacted phospholipid and thus stabilize the tubules.

3.2.2 Nickel Coating on Phospholipid Microtubules

The stabilized microtubules were prepared for coating with nickel by suspending them in a catalyst solution. All catalyst and nickel bath reactants were provided by Shipley. The catalyst mixture was prepared by dissolving 20 grams of CATAPREP 404 concentrate in 97 mL deionized water and stirring. Then 3 mL CATAPOSIT 44 catalyst concentrate was added with stirring. This mixture was sonicated for 15 minutes and filtered using a 0.45 μm filter.

A catalyst solution of 20 mL was added to 40 mL of the stabilized microtubles (pH=1) and swirled gently. This was allowed to stand for 2 hours. The volume was doubled with 60 mL water, swirled gently, and then allowed to settle for 4 hours. The supernatant was removed and the microtubules were rinsed with deionized water repeatedly until the pH=5.

The nickel coating solution was made by dissolving 0.20 grams polyvinylpyrrolidone (PVP) in 800 mL water. Then 100 mL of catalyzed tubules were added to the surfactant followed by 100 mL of NIPOSIT solution. This nickel depositing solution was prepared by mixing:

1) 88.5 mL water
2) 4.0 mL NIPOSIT 468 A electroless nickel
3) 5.0 mL NIPOSIT 468 M electroless nickel
4) 2.5 mL NIPOSIT 468 B electroless nickel

The microtubules remained in the NIPOSIT solution for 15 hours. The microtubules were nickel coated since a magnet moved along the glass surface of the flask caused the microtubules to move.

Stabilized untreated microtubules grow to considerable lengths (Figure 3.2a). However, some fracturing occurs during catalyst deposition (Figure 3.2b) and subsequent nickel coating. Even mild centrifugation of long nickel coated tubules (>100 μm) induced significant breakage.

3.2.3 Gold Coating

The first step is immersion, or displacement, coating. In this technique, the base metal is displaced by a metal ion with a lower oxidation potential than the displaced metal ion. No solution based reducing agents are necessary since the base metal acts as a reducing agent. In our system the nickel coating on the microtubule serves as the base metal which is replaced by gold as summarized by this reaction:

$$Ni + 2Au^{+} \rightarrow Ni^{2+} + Au$$

The thickness of the gold deposit using this procedure is limited since the deposition stops when the entire surface of the base metal is coated.

A commercially available immersion coating solution was selected. The solution, OROMERSE "N", is a $K[Au(CN)_2]/NH_4OH$ based solution formulated for nickel substrates. A

typical coating procedure consists of washing the tubules several times with a surfactant and then thoroughly rinsing them several more times with Millipore water. This is followed by a short (30 sec) treatment with 1.0 M HCl to remove unwanted nickel oxide. The clean Ni tubules are then placed in the OROMERSE "N" immersion plating solution for a short period of time ranging from 5 to 65 minutes. Finally, the tubules are rinsed several times to remove the immersion solution.

Figure 3.3 shows the absorption spectra of both the nickel tubules and the nickel tubules coated with gold. The peak at ca. 550 nm corresponds to the gold surface plasmon absorption typically seen in colloidal gold particles. Electron diffraction experimental d-spacings are compared the theoretical d-spacing values for fcc nickel, gold and CdSe in Table 3.1. The nickel and gold crystal structures that initially form on the tubules are not the fcc structure. The do not correlate with either hexagonal gold which has been observed in epitaxial crystallization [1] or known fcc Au-Ni alloys [2]. This suggests to us that the initial nickel coating process introduces significant impurities into the coating.

TABLE 3.1 D_{hkl} OF METAL AND SEMICONDUCTOR COATED MICROTUBULES OBTAINED FROM ELECTRON DIFFRACTION

	Ni	Ni	Au	Au	CdSe	CdSe-Au	Au 300°C
(hkl)	T	E	T	E	T	E	E
(111)	2.02	1.98	2.34	2.83	3.51	3.24	
(200)	1.75	1.58	2.03	2.28	3.08		
						2.84	
						2.52	
(111) Au						2.36	2.34
(220)	1.24	1.25	1.43	1.47	2.14		
(200) Au						2.04	2.03
(311)	1.05	1.05	1.22	1.22	1.82		
						1.69	
(220) Au						1.43	1.43
(311) Au						1.22	1.22

T-theoretical; E-experimental

We do find that annealing the gold coated tubules for 300°C for 4 hours in N_2 converts the gold into the usual fcc structure. None of the original Ni crystal structure is detected in the gold coated tubules.

The process of gold coating often promoted tubule fracture, perhaps due to expansion or contraction stresses incurred during Ni replacement. However, electron microscopy revealed that the tubule surface was much smoother (structure < 50 Å) than the original Ni coated tubules which often appeared quite heterogeneous.

3.2.4 Cadmium Selenide Coating of Gold Nickel Microtubules

Coating of the gold/nickel microtubules with the II-VI semiconductor, CdSe, was accomplished using a procedure developed for the formation of monodispersed particles. CdSe is formed by the slow, controlled generation of selenium anions in a solution of a suitable cadmium salt by the decomposition of selenourea to hydrogen selenide:

$$(H_2N)_2CSe = H_2Se + H_2NCN$$

The equilibrium can be shifted to the right at a pH>4.5. A typical coating solution consisted of 0.007 M cadmium acetate, 0.006 M acetic acid, 0.004 M sodium acetate, and 0.004 M selenourea. The resulting mixture had a pH of ≈5.2 and was purged with nitrogen in order to remove oxygen and carbon dioxide. The gold coated microtubules were then added to the solution and reacted for 10 hours at 70°C. The red colored tubules were then washed with Milli-Q water.

Figure 3.3 also shows the absorption spectra of the CdSe/gold/nickel tubules. It is interesting to note the disappearance of the gold surface plasmon peak at 550 nm and the increase overall absorption below 600 nm.

Selected area electron diffraction originating from the tubules reveals that the CdSe is at least partially crystalline with a strong broad {111} diffraction at 3.24 Å which compares with the theoretical fcc value of 3.51 Å. CdSe associated reflections also appear at 2.84, 2.52, and 1.69 Å. Other experimental reflections at 2.84, 2.36, 2.04, 1.43 and 1.22 Å originate either with the metastable gold crystal structure (2.84 Å) or the usual fcc gold.

The crystal structure that we observed for the CdSe on the gold coated microtubes was obviously not the usual fcc form. Selected area diffraction revealed only amorphous deposits in some cases. Amorphous materials or crystals of a low degree of order are commonly observed [3] upon initial growth at room temperature. The hexagonal phase, another phase that grows under certain conditions, was not observed since the strong (1010) reflection at 3.78 Å was not observed.

The CdSe deposits grown on the tubules were of hemispherical shape with a radius of up to 1000 Å. This of course is much too coarse for optical applications. To minimize light scattering, the preferred crystal size should be on the order of 30-100 Å.

3.2.5 CdS Coating of Unmetallized Phospholipid Microtubules

The phospholipid microtubules were prepared according to the method outlined by NRL workers. The tubules were then exposed to 0.1 M $Cd(NO_3)_2$ for several days and subsequently dialyzed against deionized water to remove uncoordinated Cd ions. We hoped that a significant solution concentration of Cd ions would remain complexed in the tubule center. The dialyzed tubules were then mixed with a 0.01 M stock solution of thioacetamide and the precipitation of CdS onto the microtubule surface observed as a function of time in optical microscopy.

During this coating procedure several observations were made. First, the CdS precipitated as spheroidal colloid particles on the surface of the microtubule. Second, the average

length of the tubules decreased with longer reaction times. Many of the tubules contained only one particle, usually at the end. This suggests that: 1) particles form within the phospholipid wall or surface; 2) the particles continue to grow in a manner that disrupts the physical integrity of the tubule; and 3) the tubules break, leaving the particle at the end.

3.3 Attempted Growth of CdSe in Capillary

The results of Section 2.1 suggested that a considerable mobility was present in the central disclination of the capillary oriented smectic A K24. Therefore, we thought that it might be possible to grow II-VI semiconductor particles directly in the center of the disclination by counterdiffusing reactive organometallic II and VI from opposite ends of the capillary. This concept is illustrated in Figure 3.4.

The reaction used in these procedures is based upon the use of an arrested precipitation method which utilizes an organic soluble Se source [4]. In the model reaction, a cadmium source, $Cd(ClO_4)_2$, is isolated in a reverse micelle solution (heptane/water). After addition of an equimolar amount of $Se(Si(Me)_3)_2$, $Se(TMS)_2$, which can diffuse through the organic heptane phase to the aqueous $Cd(ClO_4)_2$ micelles, reaction to ca. 20-100 Å CdSe particles takes place.

To facilitate the filled capillary reactions, we constructed the device shown in Figure 3.5. Two chambers are mounted on a microscope support stage surrounding a glass slide which can act as a support for the 50 μm capillary. The capillary tubes are then inserted into the chambers through syringe needle tips which have been placed flush with the top surface of the glass slide. With the capillary in place, the interface between the glass slide, glass capillary and syringe needle tip are epoxied to achieve a good seal. The top openings of the chambers can be sealed by inserting rubber septa which permits the chambers to be connected to a vacuum/nitrogen manifold by inserting a syringe through the septa.

Once the filling device has been set up and the chamber filled with the desired liquid crystal solution, the capillary can be filled by either: 1) heating the liquid crystals and allowing them to enter as an isotropic liquid by capillary action, or 2) using a pressure differential between the two chambers. Controlling the temperature (at the capillary) and/or using sequenced filling steps was hoped to provide the ability to limit the reaction of the two components to only a narrow region radially centered in the capillary.

In a typical reaction, one of the chambers was filled with a 10^{-3} M solution of cadmium perchlorate in K24 that was prepared by dissolution of the salt into isotropic K24. Several methods were utilized to introduce the cadmium perchlorate into the capillary. In the first method the empty capillary was filled with the K24-perchlorate isotropic phase. Another method required filling a capillary that had been previously filled with neat K24 in the oriented smectic state. Additional K24 solution was introduced in the hope that the higher flow rates in the central disclination would localize cadmium perchlorate in this region.

Once the capillaries were filled with the K24-perchlorate solution, the chambers were filled with a 10^{-3} M solution of $Se(TMS)_2$, which had been prepared and purified according to literature methods [4], and purged with nitrogen.

We were able to view the progress of the reaction in the microscope after the selenium compound had been introduced. At the beginning of the reaction the K24-cadmium perchlorate filled capillary contained the usual homeotropically ordered liquid crystal with a central disclination. After several hours of exposing the capillary to the $Se(TMS)_2$ solution, yellow red colored spherical regions appeared around the center axis with lateral extents several times the thickness of the disclination. When heated above the isotropic transition temperature, these regions dispersed into the whole domain of the liquid crystal and no distinct particles were seen.

Conceivably, the observed regions could have been collections of the desired submicron CdSe particles since the correct color was observed. However, particle production did not seem uniform along the length of the tubule or concentrated enough in the center for the conditions employed. Considerable work would be required for the appropriate conditions to make this process successful.

3.4 References

1) K. Bahadur and P. V. Sastry, Phy. Soc. Proc., 78, 594 (1961).
2) A. A. deKeijzer and W. G. Burgers, J. Appl. Phys., 33(3), 2820 (1962).
3) F. V. Shallcross, RCA Review, 677 (1963).
4) S. M. Stuczynski, J. G. Brennen, and M. L. Steigerwald, Inorg. Chem., 28(25), 4431 (1989).

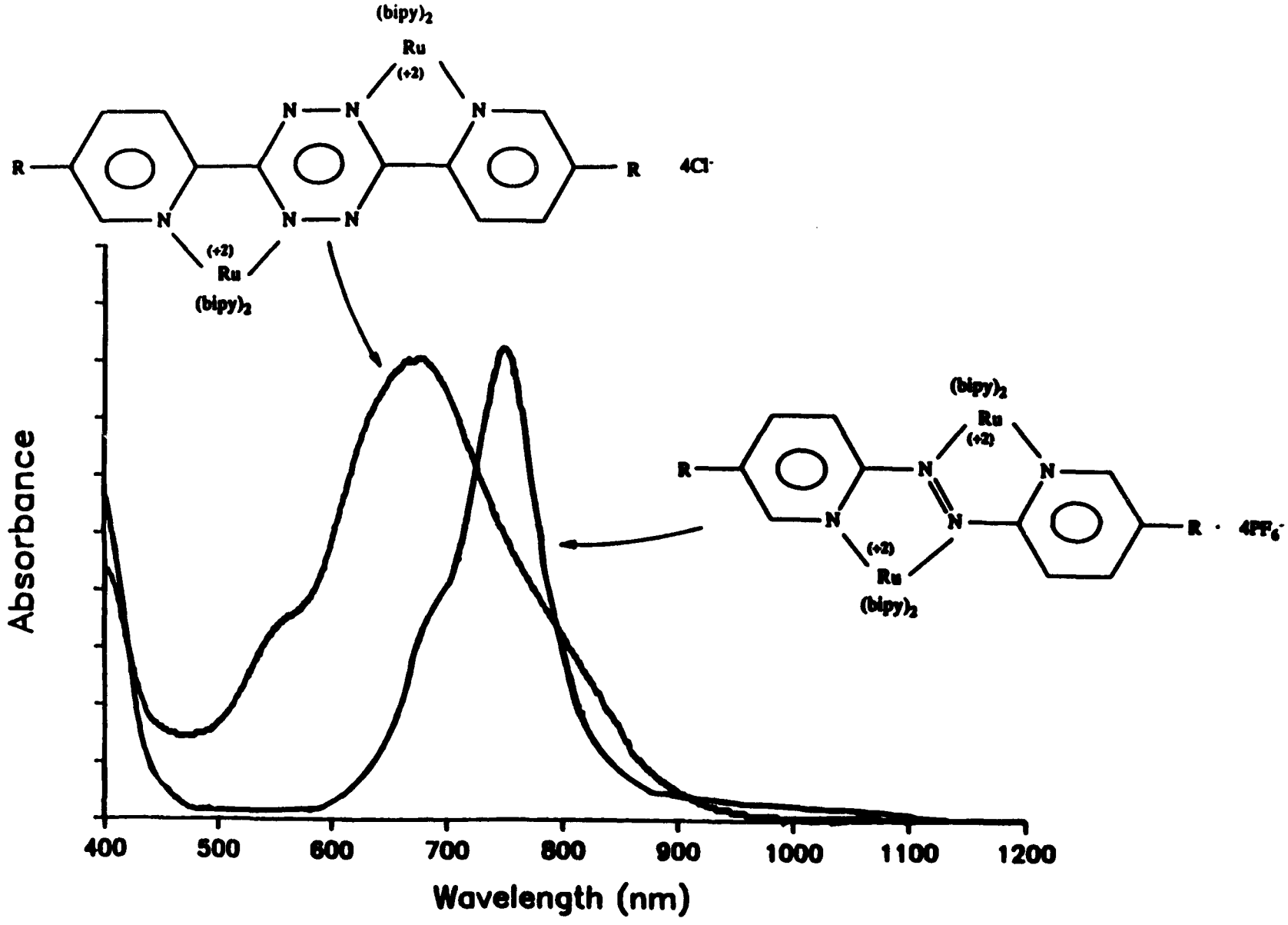

Figure 3.1 Electronic spectrum of Di-RuABPY and Di-RuBPTZ in water.

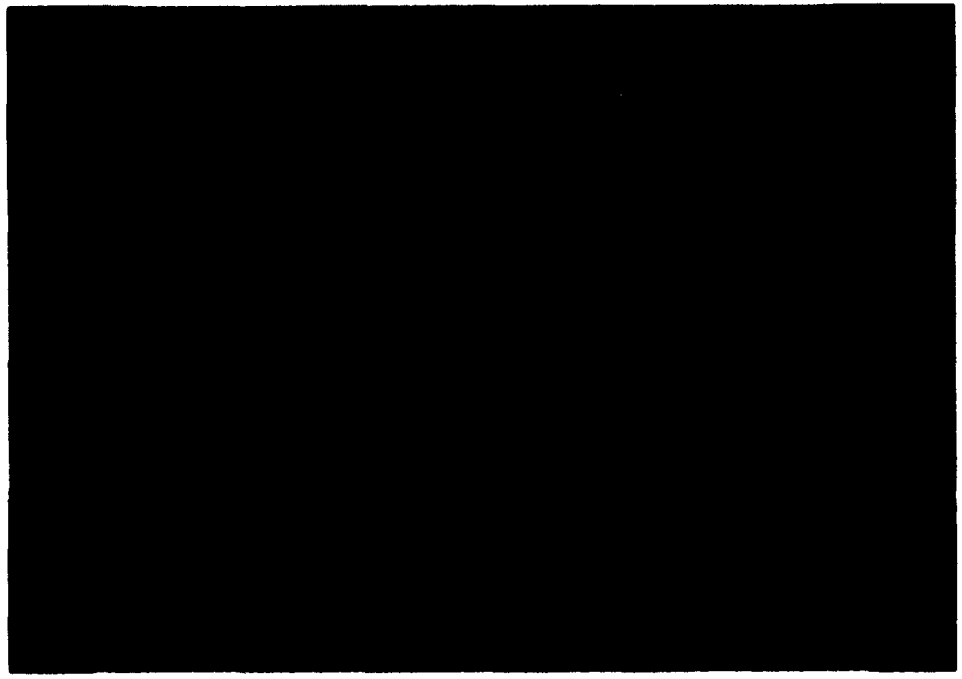

Figure 3.2a Stabilized microtubules untreated.

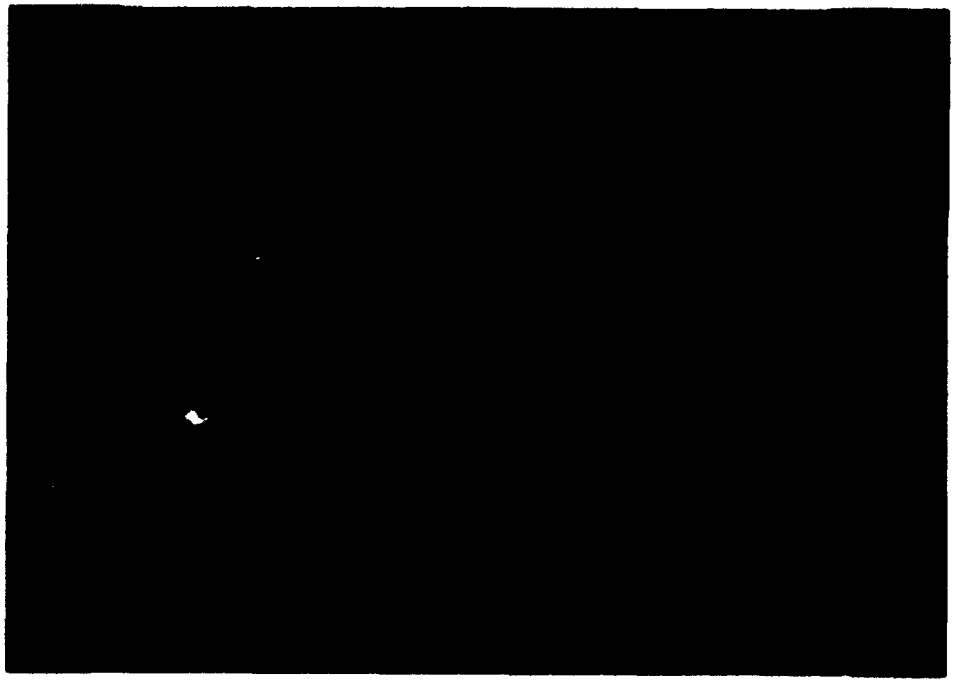

Figure 3.2b Microtubules in the catalyst mixture for 24 hours. Some fragmentation.

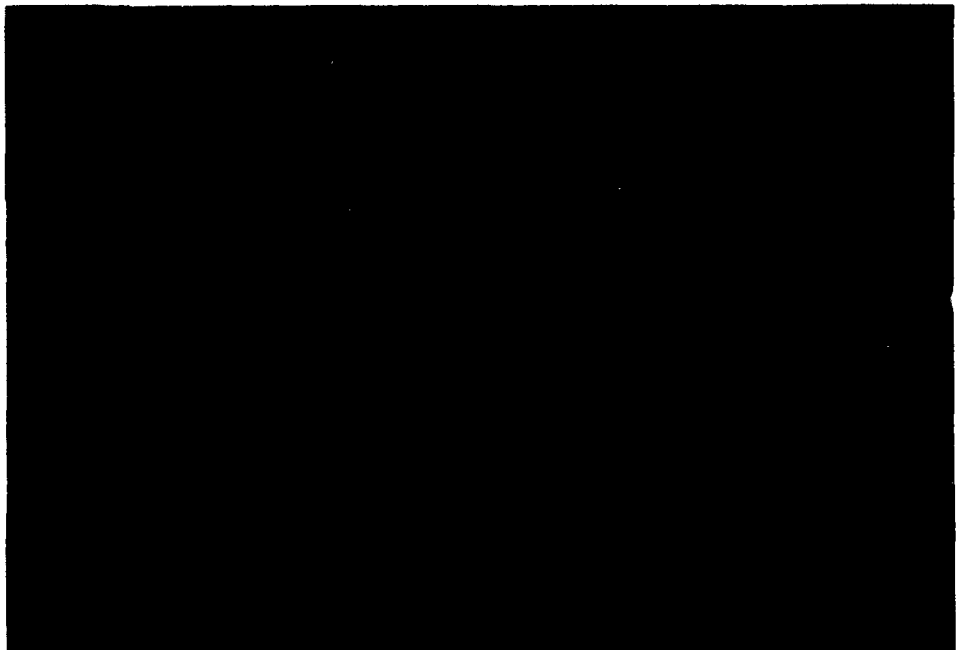

Figure 3.2c Nickel coated microtubules in NIPOSIT bath for 15 hours. Some fragmentation.

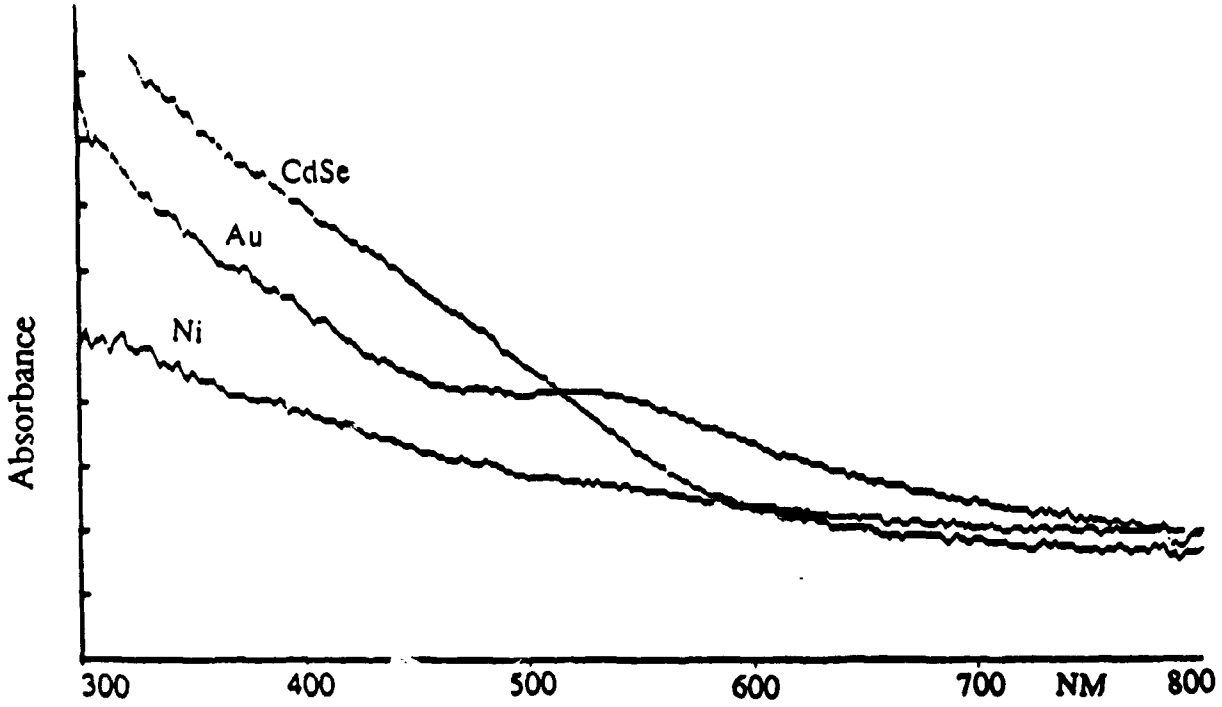

Figure 3.3 Electronic spectra of coated tubules.

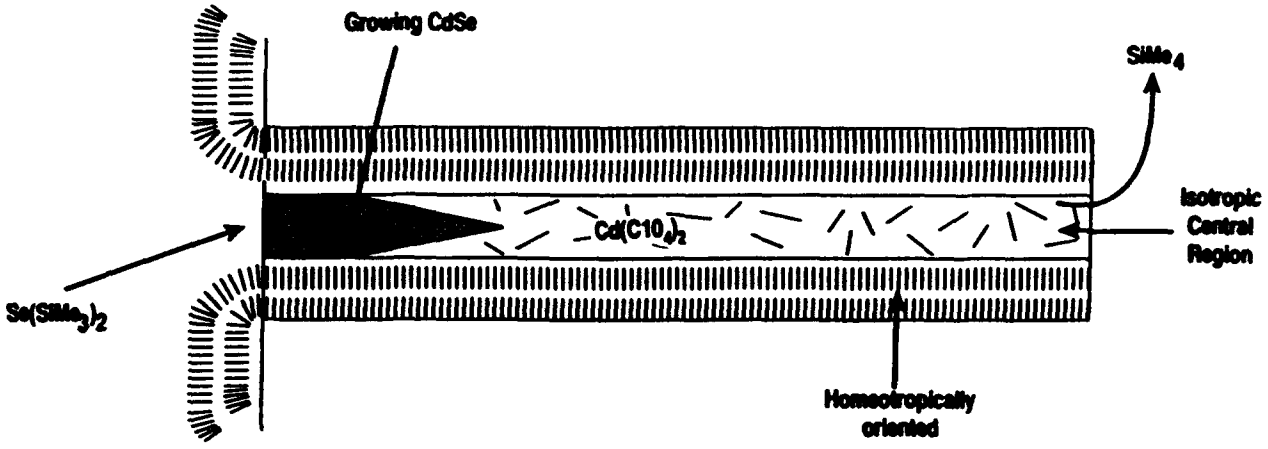

Figure 3.4 Reaction scheme for semiconductor growth in liquid crystal-filled capillary.

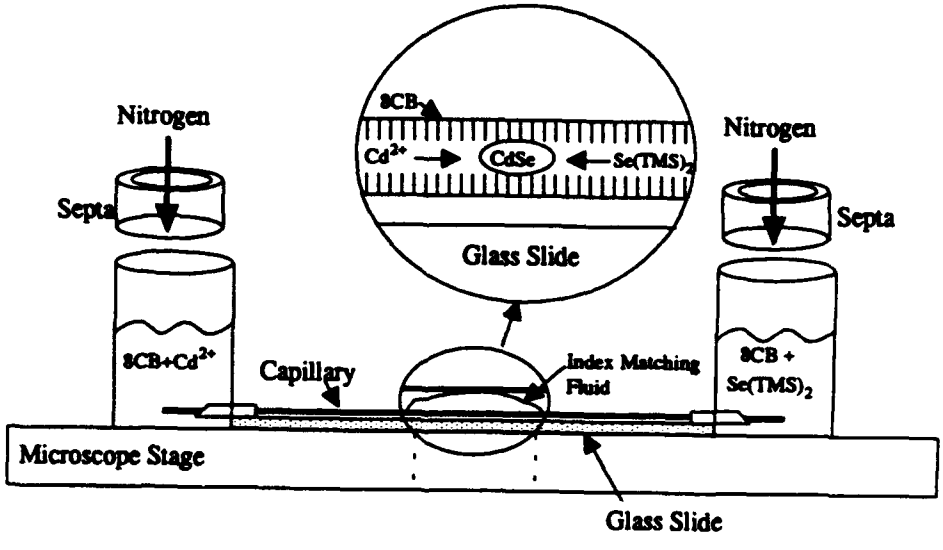

Figure 3.5 Schematic of device used to form precipitated CdSe particles within capillary.

4. NONLINEAR ABSORPTION MEASUREMENTS

4.1 Experimental Measurements

The nonlinear optical measurements were made with a Spectra Physics DCR-1, Nd/YAG laser with amplifier. The Nd/YAG laser is capable of producing short duration pulses (ca. 10 nsec) of 1064 nm radiation with energies as high as 750 μJ/pulse. The beam diameter is approximately 1 cm and is in the donut mode configuration. The void center of the donut is a relatively small portion of the beams cross-sectional area, so the maximum average light intensity that can be obtained from the laser may be estimated to be 75 Mwatts/cm^2. The laser oscillator was operated at approximately 45 lamp joules with the amplifier at 40 lamp joules to minimize the micromode structure superimposed upon the larger scale doughnut structure. A Schott-glass RG850 filter was used directly in front of the laser output to remove laser-discharge light from the beam.

The lens and cuvette are separated by 18 cm so that the beam is brought into focus 33.7 cm behind the sample and the beam spot size on the front of the cuvette is 5 mm (Figure 4.1). A beam diffuser is placed immediately in front of the sample cuvette to generate a uniform beam with peak-valley intensity variations no more than 10%. The detector A, measures the power as it exits the beam attenuator (Newport Corp. Model 935-10 attenuator and a reverse biased UDT PIN-10 photodiode). The detector B comprises a quartz beam splitter located directly behind the cuvette, a 3 mm Schott-NG9-glass-filter attenuator, a 10 cm focal length concave lens located at the entrance to a 4-inch integrating sphere (Lab Sphere) with a reverse biased UDT PIN-10 photodetector located in the integrating sphere as the detector (shielded from direct radiation by an internal baffle). The integrating sphere arrangement was used to collect as much as possible of the exiting radiation from the cuvette. The attenuator setting has been recorded for reference but is not a parameter of interest, because of the power into the cell and the power through the "blank" (solvent) has also been measured. The sensitivity on the boxcar system was 0.2 volts for all of the measurements, with 30 pulse averaging (laser was pulsing at 10 Hz). We did not use the ratioing mode but rather recorded channel A and B separately. The system had very good repeatability and the zero value had minimal drift.

4.2 Results and Discussion

Any measured optical nonlinearity can have three contributions: thermal, reorientational, and electronic [1]. In order to assess the potential for thermal effects during the measurement, the intensity dependent absorption of $NiCl_2$ was measured. Since the aquo complex of nickel ion is expected to have no reorientation or electronic nonlinearity in this regime, any measured intensity dependence of the absorption would have as its source a thermal effect. The data is presented as absorption (ratioed against pure solvent (water, in this case)) and I_{out} vs. I_{in}. Figure 4.2 reveals no intensity dependence to the absorption. We thus are confident that any nonlinear effect measured below A=0.2 is the sum of reorientation and electronic effects.

The absorptive nonlinearity of water and acetonitrile solutions of 2Ru-ABPY and 2Ru-BPTZ were measured at 1060 nm, preresonant (extinction coefficient 900 and 30 $M^{-1}cm^{-1}$, respectively, ε_{max} = ca. 20,000 M^{-1} cm^{-1}) to the strong long wavelength transition (790 nm and 690 nm, respectively). Figures 4.3 and 4.4 both exhibit a large absorptive nonlinearity that saturates above 30 MW/cm^2. The

coefficient, α_1, was estimated by the slope of the initial part of the absorbance intensity curve and the results presented in Table 4.1 along with the results from other materials. Large positive α_1 of order 10^{-4} to 10^{-5} cm/W/M were observed for the Ru complexes with no evidence of photochemical or thermal decomposition after extensive exposure.

TABLE 4.1 NONLINEAR ABSORPTION MEASUREMENTS

Material	Concentration	α_1 (CM/W/M)	A_o
2RU-BPTZ (MECN)	1.8 mM	2.7×10^{-5}	0.05
2RU-BPTZ	0.18	1.1×10^{-5}	0.005
2RU-BPTZ (H_2O)	1.8	6.0×10^{-6}	0.05
2RU-BPTZ	0.18	1.1×10^{-5}	0.005
2RU-ABPY (MECN)	0.18	6.0×10^{-5}	0.18
2RU-ABPY	0.018	3.0×10^{-4}	0.018
SULFORHODAMINE	VS	2.2×10^{-8}	0.125
β-CAROTENE	VS	7.8×10^{-10}	0.125
CARBAZOLE P	0.1	5.0×10^{-6}	0.2
2MO-ABPY	0.02	1.6×10^{-4}	0.225
2MO-BPTZ	0.015	1.6×10^{-4}	0.175
PDMTV 1:1	FILM	2.0×10^{-5}	~0.0
PDMNPV 5:1	FILM	6.0×10^{-6}	~0.0
CdSe	FILM	6.0×10^{-7}	~0.0

$$\alpha_t = \alpha_o + \alpha_1 I$$
$$A_o = \text{ABSORPTION (I=O)}$$

VS = Various cell lengths and solution concentrations.
2RU = $2[Ru(bpy)_2^{++}]$
2MO = $2[Mo(CO)_6]$
PDMTV = Various *p*-phenylene vinylene copolymers synthesized at SwRI.
Carbazole P = $AlCl_3$•N-butyl pyridinium solutions of poly[(N-butyl sulfonate)3,3'carbazyl]benzyl triethylammonium synthesized at SwRI.

Even though thermal effects do not dominate the nonlinear absorption of the 2Ru-ABPY and 2Ru-BPTZ materials, we cannot separate the relative contributions of reorientational and electronic mechanisms with nanosecond pulses. The nonlinear absorption is positive, indicating that the mechanism is much different from the exciton bleaching effects seen in polydiacetylenes. Distinguishing between instantaneous electronic effects and longer term contributions to the nonlinearity such as intersystem crossing to a lower energy triplet with a higher absorption coefficient at the frequency of interest requires narrower pulses.

4.3 References

1) R. W. Hellwarth, Prog. Quant. Electr., 5, 1 (1977).

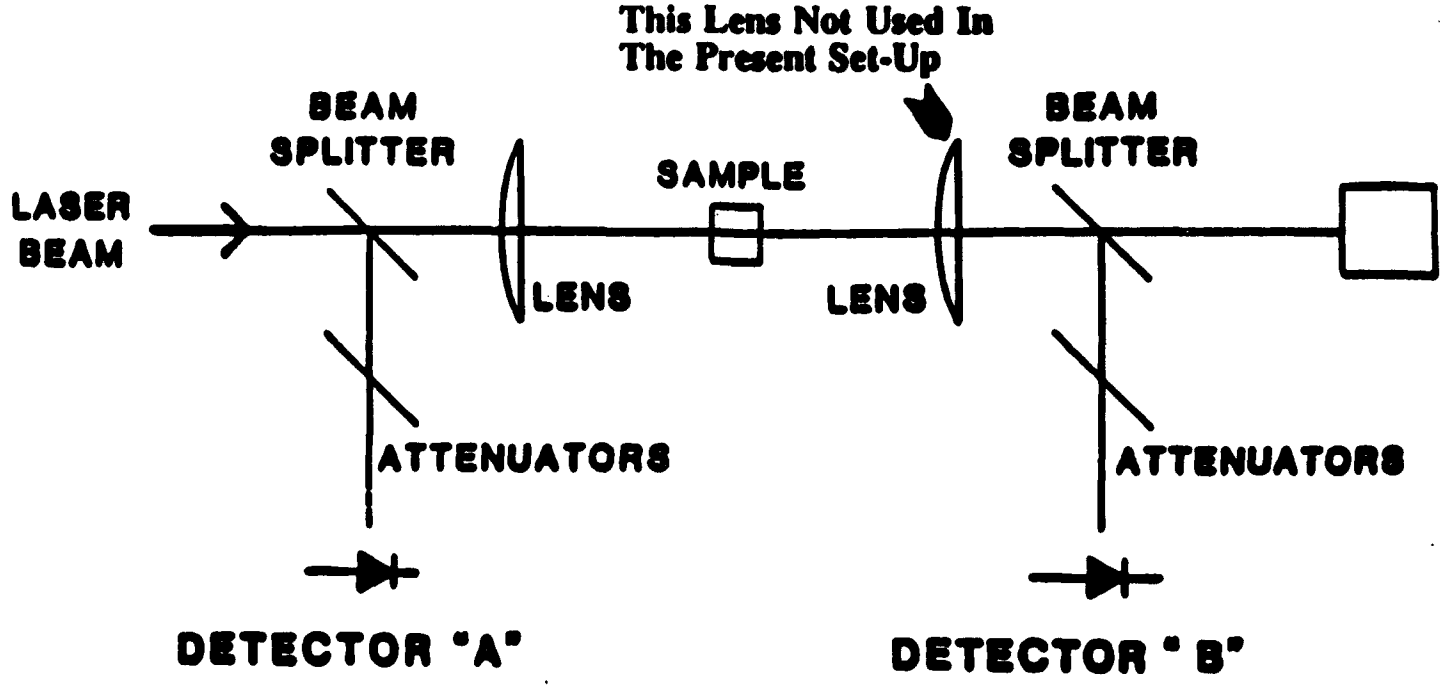

Figure 4.1 Schematic of laser setup for measurement of nonlinear absorption.

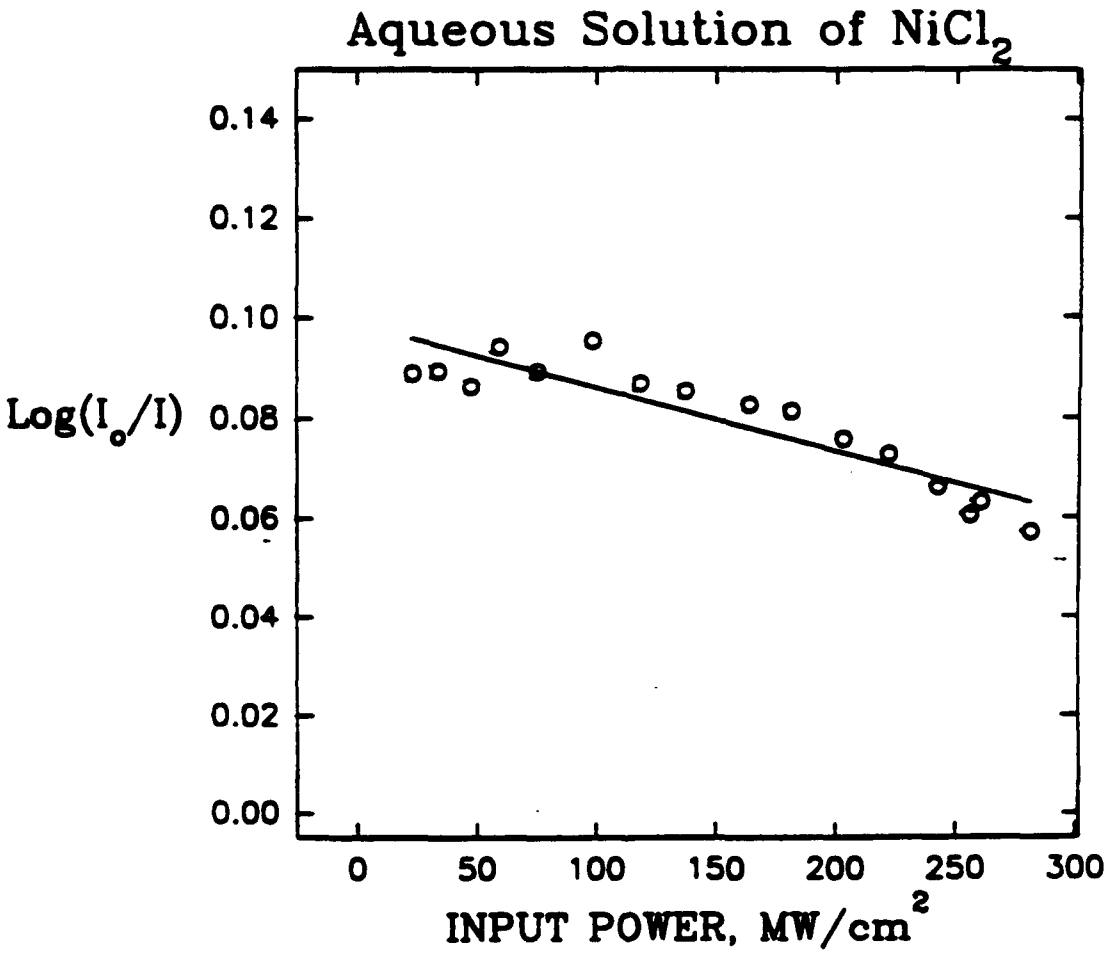

Figure 4.2 Intensity dependence of the absorbance of an aqueous $NiCl_2$ solution.

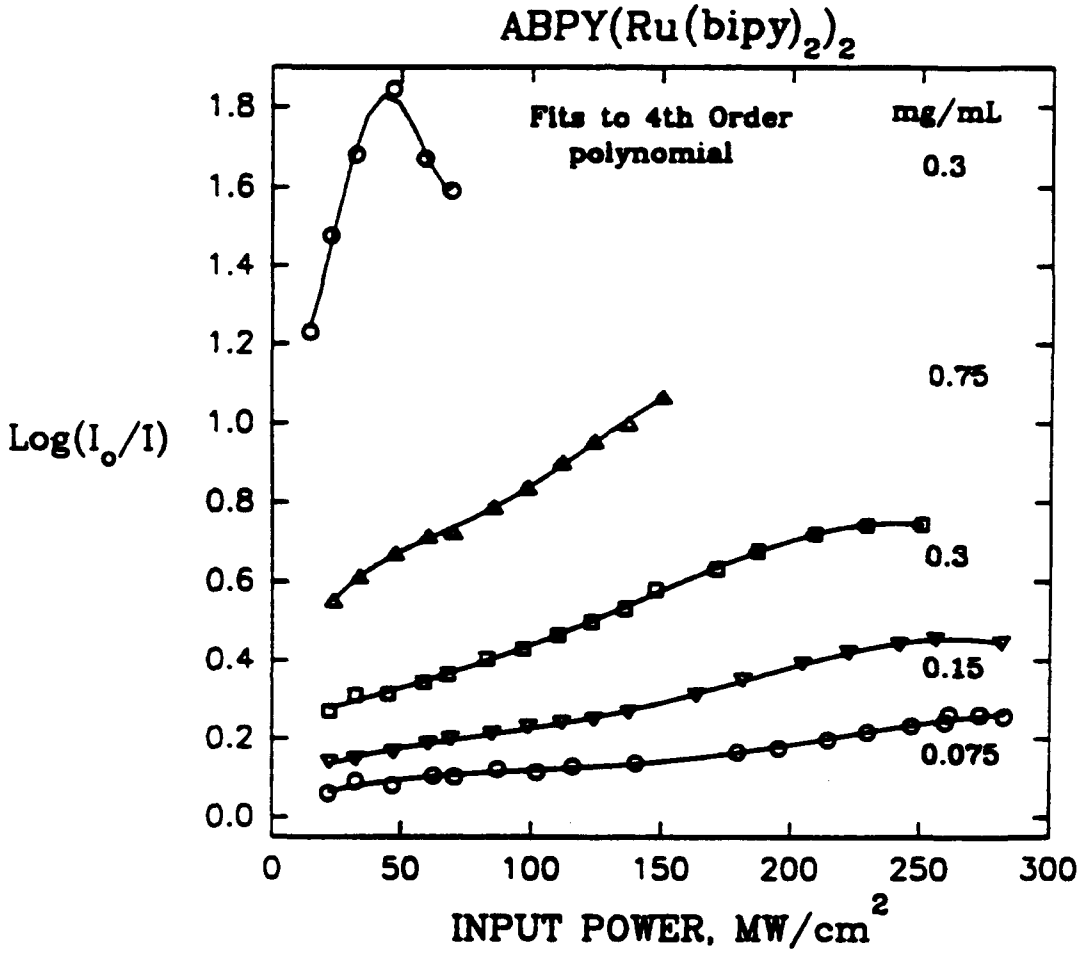

Figure 4.3 Concentration and intensity dependence of absorbance of 2RuABPY-acetonitrile.

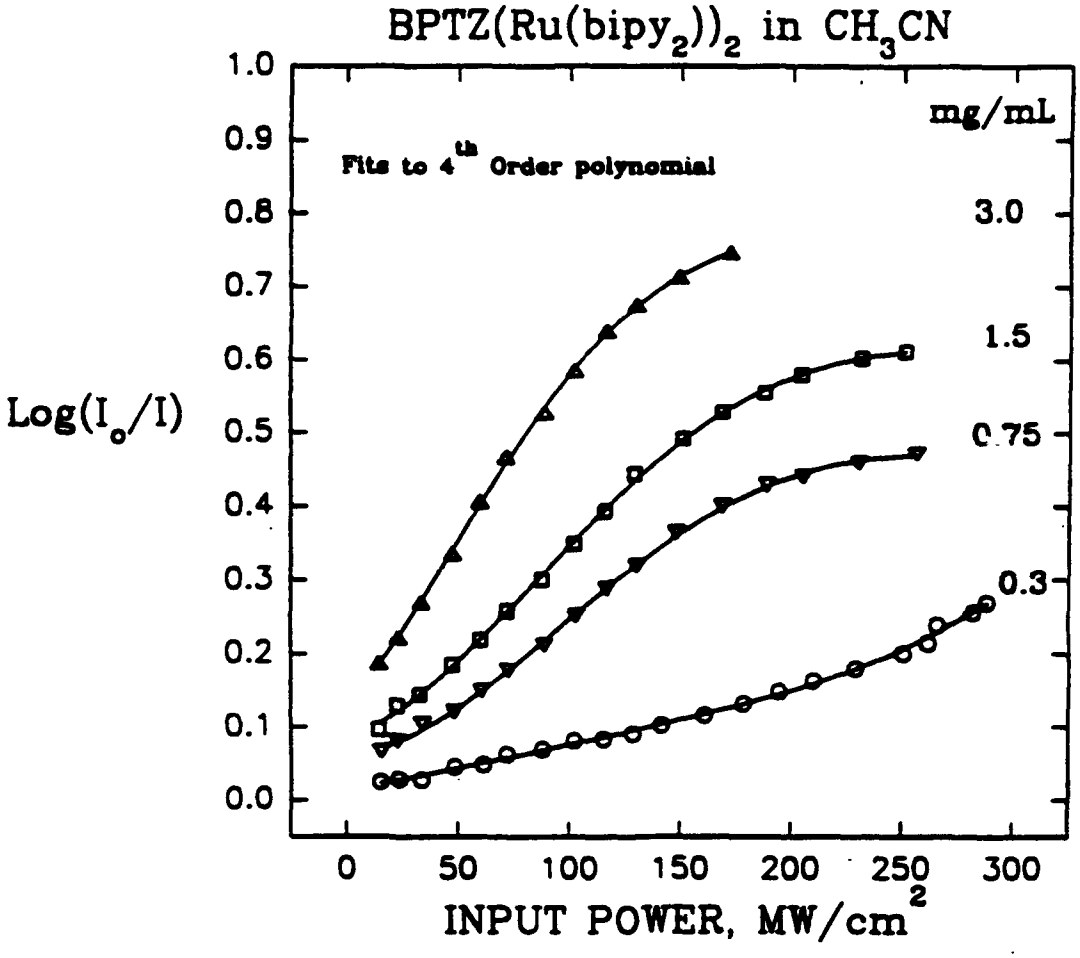

Figure 4.4 Concentration and intensity dependence of absorbance of 2RuBPTZ-acetonitrile.

5. WAVEGUIDING CHARACTERISTICS OF TUBULE STRUCTURES

5.1 Introduction

The success in precise self centering of microtubules in a matrix of liquid crystal and the potential to coat phospholipid tubules with metal and semiconductor deposits has suggested the light propagation properties of a guide with this structure be explored. Intuitively, we started with the supposition that the very high refractive index of the cladding would tend to dominate the characteristics of the guide.

5.2 Formulation

In a single cylindrical, microchannel plate cell, the configuration will consist of the cell itself and the microtubule centered inside it. Deposited onto the outside of the microtubule will be a sheath of nonlinear material, with index of refraction $n_w(I_w)$ dependent on the intensity I_w of light inside it. Between the sheath and the walls of the microchannel plate cell will be a liquid crystal material with a radial (r)-dependent index of refraction $n_m(r)$ that has a tendency to dip in value in the proximity of the sheath or of the microchannel plate walls. Another liquid crystal material will be inside the microtubule core and will be characterized by index $n_c(r)$, which will be graded towards lower values as the microtubule wall is approached. Once the nonlinear sheath is formed around the microtubule wall, the microtubule wall can be removed chemically if necessary, leaving only the sheath. This simpler configuration has been the model for theoretical work under this project. The configuration is effectively an optical wave guide.

In particular, an index of refraction profile has been chosen as follows:

$$n(r) = \begin{cases} n_c(1 - a_c r^2)^{1/2}, & 0 \le r < r_1, \\ n_w(I_w)(1 - a_w r^2)^{1/2}, & r_1 \le r < r_2, \\ n_m[1 + a_m(1 - (r/r_m)^2)]^{1/2}, & r_2 \le r \le r_m \end{cases} \quad (1)$$

This results in a profile as shown in Figure 5.1. It will be noted that there is not a dip in $n_m(r)$ as the nonlinear sheath is approached from larger r. More will be said about the effect of this approximation later after the effect of grade constants a_c, a_w, and a_m has been explored.

The effect of index profile (Equation 1) on the steady state solution will be presented here. The solution will be presented in the scalar approximation, which means that distinctions between E_x, E_y, and E_z (the components of the electric field vector) and the additional complication of solving for H_x, H_y, and H_z (the components of the magnetic intensity) will be ignored. Instead, a generic solution of the relevant wave equation will be presented. Also, the presence of a gradient term $\nabla n(r)$ in the wave equation will be ignored, which means that electric field and magnetic intensity will be treated as if they are uncoupled from each other. Under such conditions, the electromagnetic wave equation can be written as

$$\nabla^2\psi + (\omega^2/c^2)n_i(r)\psi = 0 \tag{2}$$

where $n_i(r)$ is index of refraction for a particular region of r. To solve, the solution $\psi(r, \phi, z)$ must be solved by matching across boundaries for different regions of r. The azimuthally-symmetric solution applies here, namely

$$\psi = E_i(r)e^{i\beta_i z} \tag{3}$$

where the z-direction is along the waveguide axis. Thus, the wave equation to be solved is

$$\frac{1}{r}\frac{d}{dr}\left(r\frac{dE_i}{dr}\right) + [k_i^2(1-\alpha_i r^2) - \beta_i^2]E_i = 0 \tag{4}$$

where

$$k_i^2 = \begin{cases} (\omega^2/c^2)n_c^2, & 0<r<r_1, \\ (\omega^2/c^2)n_w^2, & r_1<r<r_2, \\ (\omega^2/c^2)n_m(1+a_m), & r_2\le r\le r_m \end{cases} \tag{5}$$

and where $\alpha_i = a_c$, a_w, and $[a_m/(1+a_m)]/r_m^2$ respectively in the three regions of r. Equation 4 has the generic solution [1]

$$E_p^{(i)}(r) = \frac{A_p^{(i)}}{\sqrt{\pi}\,w_i} L_p\left(\frac{r^2}{w_i^2}\right)\exp\left(-\frac{r^2}{2w_i^2}\right) \tag{6}$$

where $A_p^{(i)}$ is an arbitrary amplitude and

$$w_i^2 = 1/\sqrt{\alpha_i}\,k_i \tag{7}$$

and where $L_p(x)$ is a Laguerre polynomial [2] of degree p. The different p corresponds to different optical modes. The wave vector β_i is also found to be p-dependent as

$$\beta_p^{(i)} = [k_i^2 - 2(2p+1)/w_i^2]^{1/2}, \quad p = 0, 1, 2,... \tag{8}$$

After matching solutions across the various boundaries, one finds that the solution to index profile (Equation 1) is given by $\psi_p^{(c)}(r)$, $\psi_p^{(w)}(r)$, and $\psi_p^{(m)}(r)$ for the three different regions, where

$$\psi_p^{(c)}(r) = \left(\frac{A_p^{(w)} e^{i\beta_p^{(w)} z}}{\sqrt{\pi}\, w_w}\right) M_p^{(c)} L_p\left(\frac{r^2}{w_c^2}\right) \exp\left(-\frac{r^2}{2w_c^2}\right) \tag{9a}$$

$$\psi_p^{(w)}(r) = \left(\frac{A_p^{(w)} e^{i\beta_p^{(w)} z}}{\sqrt{\pi}\, w_w}\right) L_p\left(\frac{r^2}{w_w^2}\right) \exp\left(-\frac{r^2}{2w_w^2}\right) \tag{9b}$$

$$\psi_p^{(m)}(r) = \left(\frac{A_p^{(m)} e^{i\beta_p^{(m)} z}}{\sqrt{\pi}\, w_w}\right) M_p^{(m)} L_p\left(\frac{r^2}{w_m^2}\right) \exp\left(-\frac{r^2}{2w_m^2}\right) \tag{9c}$$

where the boundary-dependent constants $M_p^{(c)}$ and $M_p^{(m)}$ are given by

$$M_p^{(c)} = \frac{L_p(r_1^2/w_w^2)}{L_p(r_1^2/w_c^2)} \exp\left[-\frac{r_1^2}{2}\left(\frac{1}{w_w^2} - \frac{1}{w_c^2}\right)\right] \tag{10a}$$

$$M_p^{(m)} = \frac{L_p(r_2^2/w_w^2)}{L_p(r_2^2/w_m^2)} \exp\left[-\frac{r_2^2}{2}\left(\frac{1}{w_w^2} - \frac{1}{w_m^2}\right)\right] \tag{10b}$$

It is noted that the *wave number* $\beta_p^{(w)}$ of the guided wave passing through the guide combination is *controlled by the optical parameters of the nonlinear material.* This means that the wave number *depends on the intensity* I_w *of the wave*, since from Equations 5, 7, and 8,

$$\beta_p^{(w)} = \frac{\omega}{c}[n_w^2(I_w) - 2(2p+1)\sqrt{\bar{a}_w}\, c/(\omega n_w(I_w))]^{1/2} \qquad (11)$$

where

$$I_w = \frac{|A_p^{(w)}|^2}{\pi w_w^2}\left(L_p\left(\frac{\bar{r}^2}{w_w^2}\right)\right)^2 \exp\left(\frac{\bar{r}^2}{w_w^2}\right) \qquad (12)$$

is independent of z, and where $r = (r_1 + r_2)/2$.

The different p represents different optical modes and the full solution will consist of a superposition of the different p-modes.

In the steady state solved here, the amplitudes in the core and in the medium outside the nonlinear sheath are z-independent and time-independent. This will not be the case in a pulse situation.

In a pulse situation, energy will be transferred outwardly as the pulse spreads outwardly in its motion down the guide. As the pulse loses intensity, the rate of transfer is affected because of the intensity-dependent $n_w(I_w)$. Hence, a z-dependence and time-dependence are introduced in the propagation of the pulse. This is particularly the case if the outside medium also acts as an absorbing medium (i.e., as an energy sink).

5.3 Numerical Results

Numerical computations have been carried out for p-mode intensity $\psi_p^* \psi_p$ as a function of r for different values of the optical parameters in the different regions. Of particular interest is the dependence of the relative intensity outside the core on index $n_w(I_w)$, the index of the nonlinear sheath. Also important is dependence on the thickness of the nonlinear sheet and dependence on the grade constants.

Generally, intensity as a function of r exhibits a central peak in the core and secondary peaks outside the sheath. The mode index p is an index of the number of secondary peaks outside the sheath (e.g., p=4 means 4 secondary peaks outside the sheath).

Ranges of n_w occur in which the *central peak is quenched* relative to the secondary peaks, even to the point where the central peak completely disappears. The *range* Δn_w *of these "antiresonances" is controlled by the thickness of the sheath, with the breadth* Δn_w getting larger with sheath thickness. The higher p-modes, with more peaks outside the core, tend to be "leakier", with more intensity tending to be concentrated outside the core, especially for p=2 on. Thus, the guide should *not* be configured to a monomode situation. The secondary peaks can also be quenched by

shifting n_w of the antiresonance range. Hence, the antiresonance needs to be carefully tuned. This *tuning* is controlled by n_c and n_m and the grade constants. An intensity-dependent $n_w(I_w)$ can thus drive the optical system *toward or away from antiresonance*. This is possible even in a situation where several modes are superposed.

The effect of the grade constants on individual modes are chiefly on the breadth, position, and amplitudes of the individual peaks. As grade constant a_m is increased, the secondary peaks shift toward the sheath, become narrower, and increase in relative intensity. If a_m is increased too much, the central peak gets too narrow and the first secondary peak crosses through the sheath, and the situation reverses and the secondary peaks decrease in relative intensity. Thus, there is an *optimal grade a_m which enhances the relative intensity outside the core.* The effect of a reverse grade (mentioned earlier) in the proximity of the sheath should be such as to prevent the first secondary peak from crossing the sheath and to enlarge the range of a_m that can enhance the relative intensity outside the core.

Appendix A has a detailed discussion (with figures) showing details of the effects described above.

At present the most extensive calculations have been completed at a wavelength of 600 nm as described above. However some preliminary calculations at 430 nm have revealed similar features. Antiresonant modes formed at the same refractive index parameters but at different p. This indicates that a single waveguide could be used as a broad band limiting device.

5.4 Conclusions

The important conclusions of the theoretical part are that:

1) A thin 200-500 Å sheath of very high refractive index material surrounding a core of much lower index can dominate the waveguide properties of a coaxial guide.

2) A difference of only 0.2 in the wall refractive index can induce "antiresonant modes" which have no intensity in the central regions to convert to "resonant" modes with a strong central intensity.

Therefore, the following strategy is suggested. Light is injected into the guide so as to predominantly excite the antiresonant modes which have little intensity in the central region of the guide. The practical way this might be done is by blocking the front end of the central guide so as to prevent the excitation of any mode with a strong central peak. In order to inject light into the guide, some linear combination of mode intensities must be found that matches the light intensity profile at the front of the guide.

Using Figure A20 in Appendix A, a uniform illumination of the annular liquid crystal region would selectively launch antiresonant modes p=2,3. Low intensity light will proceed down the outer, liquid crystal portion of the guide and exit at the back end.

Since mode 3 has a significant intensity in the tubule wall, the refractive index of the wall will bleach as the leading edge of the pulse proceeds down the guide. At high intensity, 10,000 W/cm^2, the refractive index of the wall will decrease to 2.6 through absorption bleaching. Since all modes of sufficiently low order $p<6$ have strong central peaks (see for example Figure A3), virtually all of the radiation will be localized in the tubule and absorbed in the back end.

The heat generated by optical absorption will be dissipated into the liquid crystal matrix. If the temperature increases sufficiently, a transition into the highly scattering nematic state will be induced, further blocking the beam transmission. Since the liquid crystal is self-healing and the central tubule waveguide is self-centering, relaxation to a damage free initial state will occur in a short time.

5.5 References

1) M. S. Sodha and A. K. Ghatak, Inhomogeneous Wave Guides (Plenum, NY, 1977), p. 164.

2) G. Arfken, Mathematical Methods for Physicists (Acad. Press, Orlando, FL, 1985), pp. 721-5.

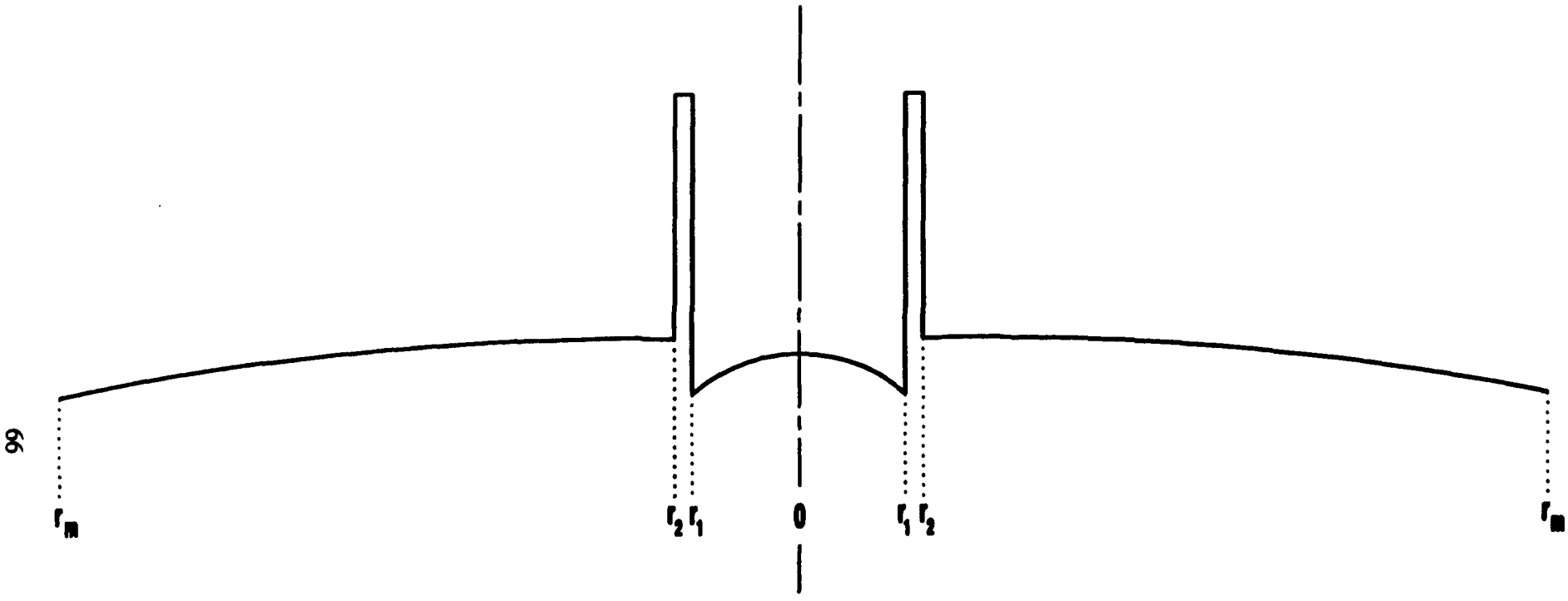

Figure 5.1 Radial profile of index of refraction.

6. CONCLUSIONS

We were successful in finding that both water-alcohol-surfactant based lamellar and nonaqueous smectic A liquid crystals would homeotropically orient in 50-100 μm diameter capillaries, leaving a mobile isotropic phase isolated along the axis of the capillary. In both cases microtubules could be oriented in the center and parallel to the long axis of the capillary by incorporation of the tubules into the liquid crystal reservoir prior to capillary filling. The tubules remained centered in this fashion for weeks. In principle, the desired coaxial waveguide could be constructed in this fashion. However, during the filling operation, even metal coated tubules were fractured in the regions of high shear stress at the capillary entrance. Unoriented small fragments then were observed distributed throughout the cross section of the capillary. The centering of the tubules depended critically on the end surface roughness at the capillary inlet. Under favorable conditions the liquid crystal coated the inlet with a cap (homeotropic orientation parallel to the capillary axis) with a central region of low shear viscosity through which the tubule could pass.

Coating of either Ni or Au coated tubules with the desired fine grained CdS or CdSe particles proved to be quite difficult as did the production of CdS particles on uncoated phospholipid tubules. Unusual crystal structures, nonuniform particle size and tubule breakage were the most common defects.

Because of the structural problems with the tubules, we tried to eliminate them altogether by attempting to generate CdSe particles directly in the central isotropic core of the K24 filled guide by coreaction of cadmium perchlorate and $Se(TMS)_2$. CdSe particles did seem to form near the isotropic zone but with a much larger lateral extent that was unsuitable for waveguide fabrication.

The successful preparation of the homeotropically oriented, water-based lamellar liquid crystals encouraged permits the incorporation of water-soluble NLO materials in the waveguide. We measured the nonlinear optical properties of alcohol and water soluble 2Ru-ABPY and 2Ru-BPTZ for possible encapsulation in the central isotropic solution phase. As predicted from theoretical calculations, a large reversible, nonlinear absorption coefficient of ca. 10^{-4} - 10^{-5} cm/W/M was found at 1060 nm for a 5-nsec pulse width, preresonant to the strong near IR transition. The visible region of the spectrum was not explored but large coefficients were expected here also.

The steady state solution of the wave equation for a coaxial waveguide (4 μm diameter) containing a central microtubule (0.5 μm diameter) coated with a material with a nonlinear refractive index predicts that either a positive or negative refractive index change on the order of 0.1 in the tubule coating will lead to optical limiting.

In conclusion, the usefulness of biologically based tubules as a substrate for semiconductor growth and/or fabrication of coaxial waveguides is limited. Of greater promise is the observation that an apparently isotropic solution phase core spontaneously appears in capillary oriented, water-based lamellar liquid crystals. Incorporation of water soluble NLO materials such as surfactant stabilized Ag-CdS particles or 2Ru-BPTZ, 2Ru-ABPY metal ligand complexes in this zone could lead to the required waveguide structure.

APPENDIX A

DETAILED PRESENTATION OF NUMERICAL RESULTS

APPENDIX A

DETAILED PRESENTATION OF NUMERICAL RESULTS

Figs. 1A-6A and Figs. 7A-12A describes similar sets of data, expect that in the first group n_c = 1.25 and n_m = 1.40 whereas in the second group n_c = 1.40 and n_c = 1.25. For both sets, the nonlinear sheath is thin (0.02μ thick) and in both cases, the index of refraction n_w of the sheath is varied across the values n_w = 3.4, 2.8, 2.7, 2.6, 1.6. The grade constants are fixed at $a_c = 0.2 \times 10^{12} m^2$, $a_w = 0.1 \times 10^{12} m^2$, and $a_m = 0.125 m^2$. The frequency of the light is $f = 5 \times 10^{14} sec^{-1}$, which is a visible light frequency. The pertinent boundary radii are r_1 = 0.25μ, r_2 = 0.27μ, and r_m = 2.00μ.

In Figs. 1A-6A (for which n_c = 1.25, n_m = 1.40, the following details are seen, taken mode by mode:

- p = 0: There is a slight shifting of relative intensity to outside the core ($r > r_1$) as n_w gets smaller from 3.4 to 1.6. The amplitude of the central peak also grows simultaneously from 0.713 to 1.035 as n_w goes from 3.4 to 1.6.

- p = 1: A secondary peak outside the core at 1.06μ grows in relative intensity as n_w goes from 3.4 to 1.6. The relative intensity shifts away from the core a little more noticeably than p = 0.

- p = 2: Two secondary peaks exist outside the core at r = o.79μ and r = 1.58μ. An intensity shift sharply upward exists at the sheath. *The central peak quenches at n_w = 2.8.* In this case, the relative intensity is almost entirely outside the core, but the total intensity is small, peaking at a value of 0.008 at the boundary of the nonlinear sheath. At n_w = 3.4, the central peak intensity is restored to 0.162 and is four times the size of the first side peak. At n_w = 2.6, the central peak is restored to 0.035 and is about ten times the size for the first side peak. Below n_w = 2.4, the relative intensity begins to shift gradually toward the outside away from the core. The dramatic quenching of the central peak will be called an *"antiresonance"*. If tuning n_w to an antiresonance is to be useful, adjustments will need to be made in other parameters, so that the total intensity of the first side peak is larger in value. Note that at n_w = 2.4, the intensity outside the core is quenched. Thus, as one goes through an antiresonance (where the central peak is quenched) to lower n_w, the central peak increases while the secondary peaks first quench then start to increase slowly in relative intensity.

- p = 3: Three peaks are seen outside the core at R = 0.64μ, 1.22μ, and 2μ. There is a gradual increase in relative intensity outside the core from n_w = 3.2 to 2.4. The intensity outside the core is quenched at n = 1.6, pointing to an antiresonance in the range $1.6 \le n_w < 2.4$.

- p = 4: Four peaks outside the core, but one is beyond $r = r_m$ = 2μ. An antiresonance is very near n_w = 1.6, since the secondary peaks have grown considerably in relative intensity and the central peak has diminished considerably in total intensity. The secondary peaks for $r < r_m$ are at 0.56μ, 1.05μ, and 1.60μ.

- p = 5: Five peaks outside the core. The first secondary peak overlaps into the sheath. Peak locations for $r < r_m$ are at 0.52μ, 0.94μ, 1.39μ, and 1.89μ. In the p = 5 case, the secondary peaks have noticeably more relative intensity than other modes and are increasing in relative intensity from n_w = 3.4 to n_w = 1.6. a possible antiresonance seems to exist below n_w = 1.6.

In Figs. 7A-12A (for which $n_c = 1.40$, $n_m = 1.25$), the behavior is surprisingly quite similar. Some differences do exist between this and the first case. In detail, the behavior is as follows:

- p = 0: The relative intensity is shifted toward the core slightly compared to $n_c = 1.25$, $n_w = 1.40$ (i.e. with n_m reduced below n_c, less light gets out of the core). Again, there is a slight shift of relative intensity out of the core as n_w goes from 3.4 to 1.6.

- p = 1: The single secondary peak outside the core is shifted to a larger r, namely r = 1.14μ, compared to the case of $n_c = 1.25$, $n_w = 1.40$. Thus, *a change in n_m and n_c affect the positions of the secondary peaks*. The side peak again grows in relative intensity as n_w goes from 3.4 to 1.6. At the same time the central peak grows in absolute intensity from 0.188 to 1.39, indicating that there may be an antiresonance above $n_w = 3.4$.

- p = 2: Two secondary peaks exist outside the core at r = 0.82μ and r = 1.68μ (again shifted to larger r). An antiresonance appears at $n_w = 2.4$. For lower n_w, the side peaks return and gradually begin to grow in relative intensity as n_w is lowered.

- p = 3: This is very sticking. The intensity in the case is always quenched outside the core for all n_w investigated.

- p = 4: Secondary peak positions are at 0.59μ, 1.13μ, and 1.68μ (again shifted to larger r). Probably a fourth peak exists for $r>r_m$. There is a gradual increase of relative intensity away from the core as n_w goes from 3.4 to 1.6 until finally, at $n_w = 1.6$, an antiresonance is clearly eminent, as seen by the drop in total intensity to 0.015.

- p = 5: Four peaks at 0.55μ, 1.00μ, 1.25μ, and 2.00μ (again shifted to larger r) are seen for $r<r_m$ and another should exist for $r>r_m$. All these peaks increase in relative intensity as $n_w = 1.6$ is approached from larger values, suggesting an antiresonance below $n_w = 1.6$.

In general, for this second data set with n_m reduced relative to n_c, the relative intensity shifts toward the core while the secondary peaks shift away from the core.

In the next data set, the nonlinear sheath has its thickness Δr increased to 0.05μ (from 0.02μ). The index of refraction set $n_c = 1.25$, $n_m = 1.40$ is chosen in Figs. 13A-18A. All other parameters are kept the same as before. Again $n_w = 3.4$, 2.8, 2.6, 2.4, and 1.6. Modes p = 0, 1, ..., 5 are again investigated.

- p = 0: Compared to Δr = 0.02μ, there is a general shifting of relative intensity toward the core. However, the relative intensity shift as n_w goes from 3.4 to 1.6 is actually greater than in the Δr = 0.02μ case. In effect, the thicker nonlinear sheath means that changes observed before are now magnified.

- p = 1 Again, the relative intensity shifts away from the core as n goes from 3.4 to 1.6. The side peak at r = 1.08μ (about the same position as for Δr = 0.02μ) changes in size by ΔI = 0.07 as compared with side peak for Δr = 0.02μ sheath, which changed in size by ΔI = 0.05 Again, *changes appear to be enhanced by the thicker sheath*. The antiresonance for p = 1 appears to shifted down to $n_w \approx 3.7$-3.8 since the side peak is quenched at $n_w = 3.4$.

- p = 2 Two peaks appear at r = 0.77μ, 1.58μ (approximately same positions as for Δr = 0.02μ sheath). The antiresonance at $n_w = 2.8$ gives an almost total quenching of the central peak while at the same time showing a *much larger secondary peak in total intensity* by two orders of magnitude. This is a welcome enhancement of the antiresonance effect. Quenching of the side peaks occurs at $n_w = 2.4$ as before. the

quenching of the side peaks is still apparent at $n_w = 1.6$, where two tiny amplitude peaks have returned.

- p = 3 Three secondary peaks are found at r = 0.65μ, 1.22μ, and 2.0μ. Again, the peaks are enhanced when at maximum size. The intensity outside the core is again quenched at $n_w = 1.6$, pointing to an antiresonance in the range $1.6 \leq n_w \leq 2.4$.

- p = 4: Three peaks are seen at r = 0.58μ, 1.07μ, and 1.62μ. A fourth peak should be found at $r > r_m$. An antiresonance again occurs at $n_w = 1.6$, only here the quenching of the central peak is clearly seen. An order of magnitude enhancement is seen in the total intensity of the first secondary peak at antiresonance.

- p = 5: Four peaks are found at r = 0.5μ, 0.92μ, 1.38μ, and 1.87μ, and one is apparently beyond $r_m = 2\mu$. An antiresonance is seen at $n_w = 1.6$ (which is not the case with the thinner sheath). The system is still near antiresonance at $n_w = 2.4$, with considerable relative intensity still in the side peaks even at $n_w = 2.6$ and 2.8, but finally subsiding at $n_w = 3.4$. *The antiresonance for the thicker sheath apparently has a much greater breadth in n_w.*

Figures 19A-20A show what happens when the *grade constants are increased.* The index of refraction profile shows an obvious grading now, as expected.

In particular, for the case when a_c is increased from $0.2 \times 10^{-12} m^{-2}$ to $0.75 \times 10^{-12} m^{-2}$ and a_m from 0.125 to 0.625, the following details apply to the case of a 0.05μ sheath and $n_w = 2.8$, $n_c = 1.25$, and $n_m = 1.4$.

- p = 0: The central peak decays much more smoothly with no sharp discontinuity in slope at r_1 or r_2. Less relative intensity is concentrated outside the core.

- p = 1: A shift in position of the side peak toward the core to r = 0.74μ is seen. (Compare with r = 1.08μ before.) The central peak practically decays to almost zero inside the core, and does not link to the outside region through the sheath in an efficient way. The result is a diminished secondary peak.

- p = 2: The sharp cusp seen in the sheath in earlier plots is greatly diminished. The central peak is totally quenched. *Side peaks are at a much larger total intensity and are shifted in toward the core* (r = 0.54μ, 1.08μ vs. r = 0.77μ, 1.58μ for the lesser graded case before). Grading of the outside medium apparently enhances side peaks (i.e. *heightens antiresonance*).

- p = 3: The central peak is quenched relative to side peaks (at r = 0.41μ, 0.83μ, 1.33μ), which are again shifted toward the core and are relatively much larger than in the lesser graded case.

- p = 4: The central peak ends at r = 0.17μ and intensity starts to rise toward the first side peak before the boundary is reached at the sheath at r = 0.25μ, producing in effect a shoulder on the first side peak. The four peaks at r = 0.35μ, 0.70μ, 1.08μ, and 1.55μ are all evident and clearly shifted toward the core, as compared with the lesser graded case. The relative intensities of the secondary peaks are much larger than in the lesser graded case.

- p = 5: The central peak ends at r = 0.15μ and as intensity rises toward the sheath, the effect is to produce a bifurcated first side peak. Averaging across the bifurcation, the first

side peak is at r = 0.32μ. Other secondary peaks are at 0.63μ, 0.93μ, 1.29μ, 1.73μ. This time however the side peaks are reduced in size relative to the central peak.

Figure 20A represents a change in a_c but not in a_m, so that the grade constants are $a_c = 1.25 \times 10^{-12} m^2$, $a_w = 0.1 \times 10^{-12} m^2$, and $a_m = 0.625$. It is found that the peaks in the outside medium don't change position and don't change relative heights until p = 5. In the core, the central peak is narrower and the intensity rise toward the sheath results in a trifurcated first side peak. It is clear that *the key grade constant is* a_m, which controls the positions and relative heights of the secondary peaks.

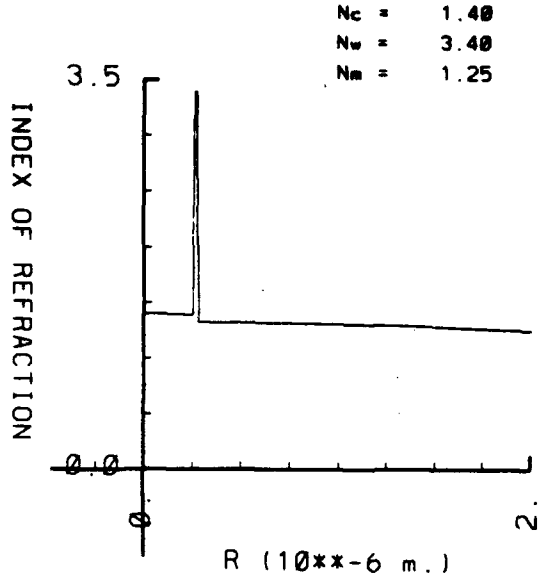
Nc = 1.40
Nw = 3.40
Nm = 1.25
3.5
INDEX OF REFRACTION
0.0
0.
2.
R (10**-6 m.)

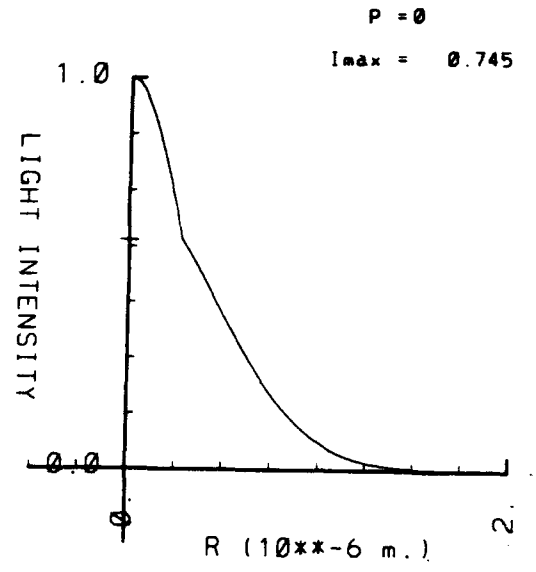
P = 0
Imax = 0.745
1.0
LIGHT INTENSITY
0.0
0.
2.
R (10**-6 m.)

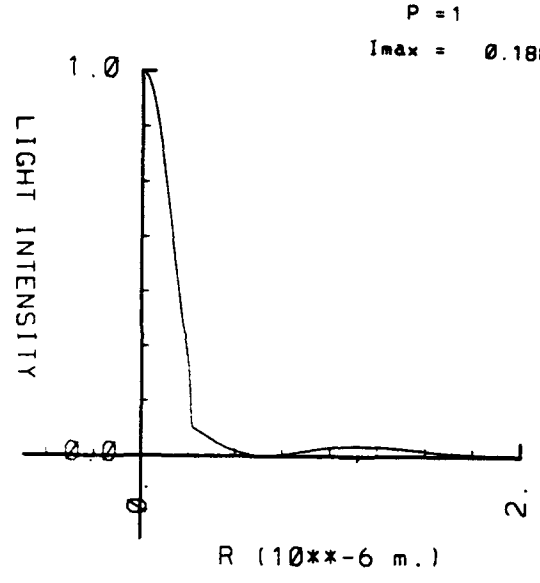
P = 1
Imax = 0.188
1.0
LIGHT INTENSITY
0.0
0.
2.
R (10**-6 m.)

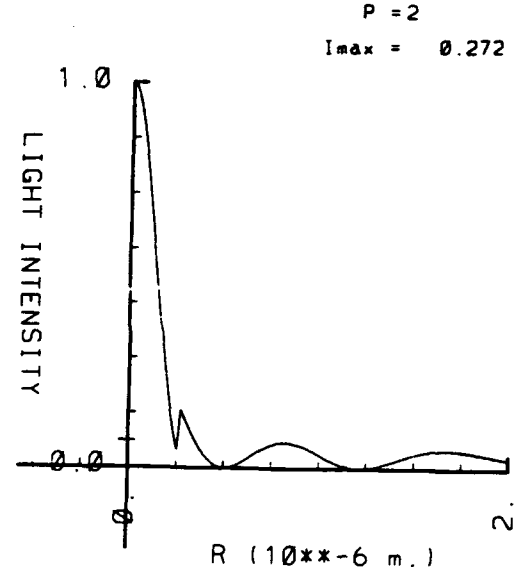
P = 2
Imax = 0.272
1.0
LIGHT INTENSITY
0.0
0.
2.
R (10**-6 m.)

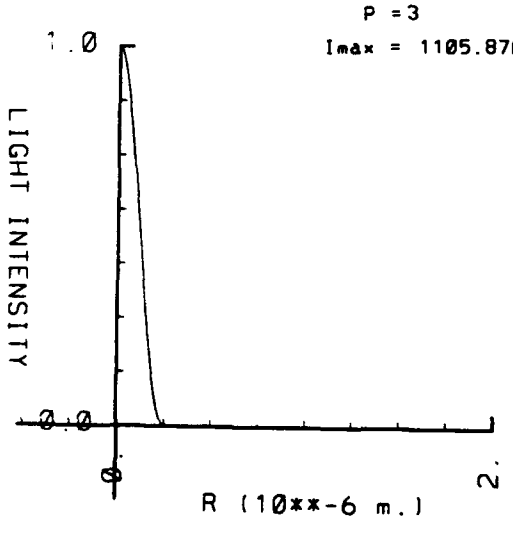
P = 3
Imax = 1105.870
1.0
LIGHT INTENSITY
0.0
0.
2.
R (10**-6 m.)

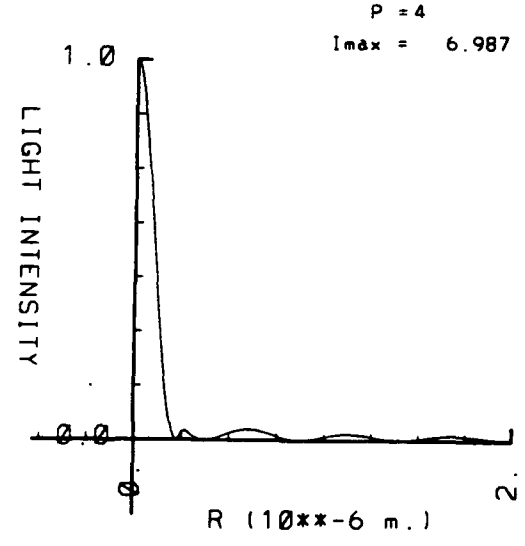
P = 4
Imax = 6.987
1.0
LIGHT INTENSITY
0.0
0.
2.
R (10**-6 m.)

Figure 1A

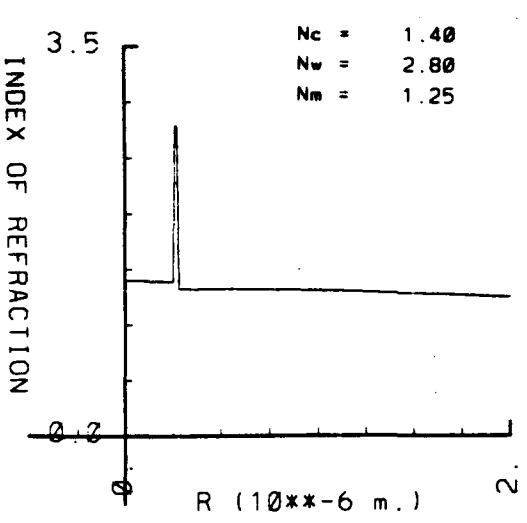
3.5
Nc = 1.40
Nw = 2.80
Nm = 1.25
INDEX OF REFRACTION
0.0
0.
R (10**-6 m.)
2.

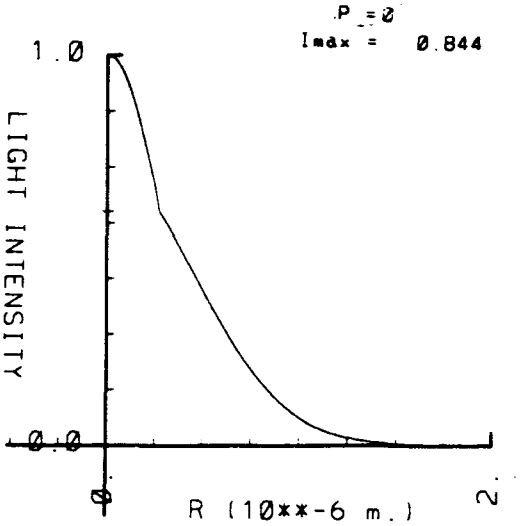
P =0
Imax = 0.844
1.0
LIGHT INTENSITY
0.0
0.
R (10**-6 m.)
2.

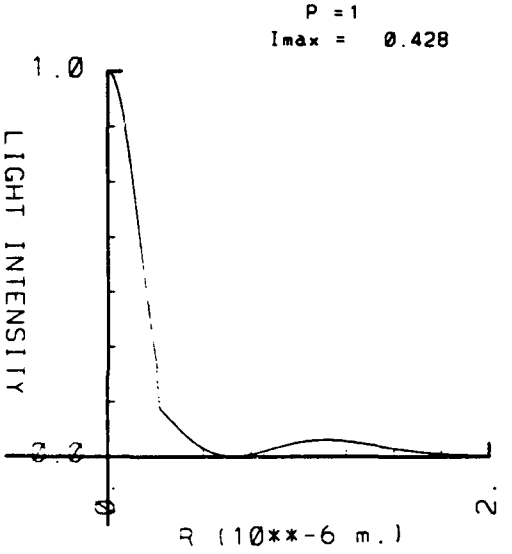
P =1
Imax = 0.428
1.0
LIGHT INTENSITY
0.0
0.
R (10**-6 m.)
2.

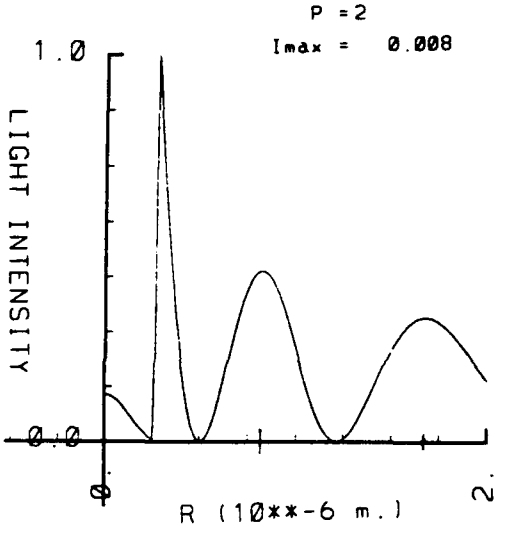
P =2
Imax = 0.008
1.0
LIGHT INTENSITY
0.0
0.
R (10**-6 m.)
2.

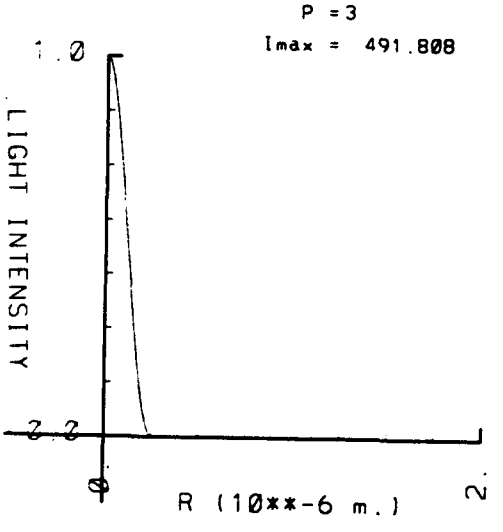
P =3
Imax = 491.808
1.0
LIGHT INTENSITY
0.0
0.
R (10**-6 m.)
2.

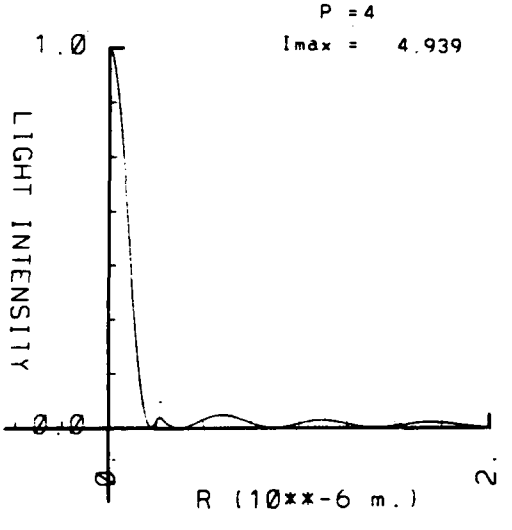
P =4
Imax = 4.939
1.0
LIGHT INTENSITY
0.0
0.
R (10**-6 m.)
2.

Figure 2A

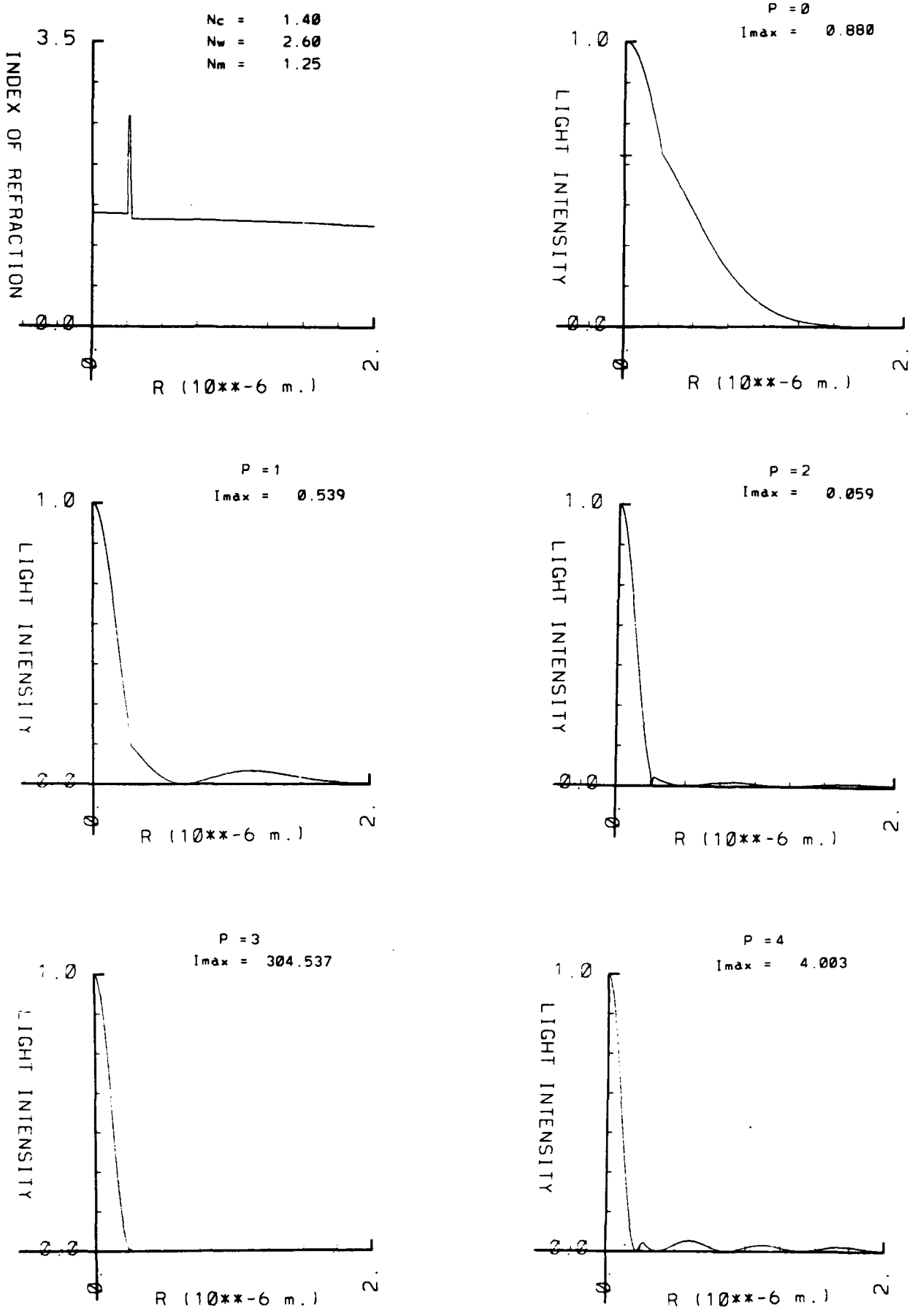
Nc = 1.40
Nw = 2.60
Nm = 1.25
3.5
INDEX OF REFRACTION
0.0
0.
2.
R (10**-6 m.)
P = 0
Imax = 0.880
1.0
LIGHT INTENSITY
0.0
0.
2.
R (10**-6 m.)
P = 1
Imax = 0.539
1.0
LIGHT INTENSITY
0.0
0.
2.
R (10**-6 m.)
P = 2
Imax = 0.059
1.0
LIGHT INTENSITY
0.0
0.
2.
R (10**-6 m.)
P = 3
Imax = 304.537
1.0
LIGHT INTENSITY
0.0
0.
2.
R (10**-6 m.)
P = 4
Imax = 4.003
1.0
LIGHT INTENSITY
0.0
0.
2.
R (10**-6 m.)

Figure 3A

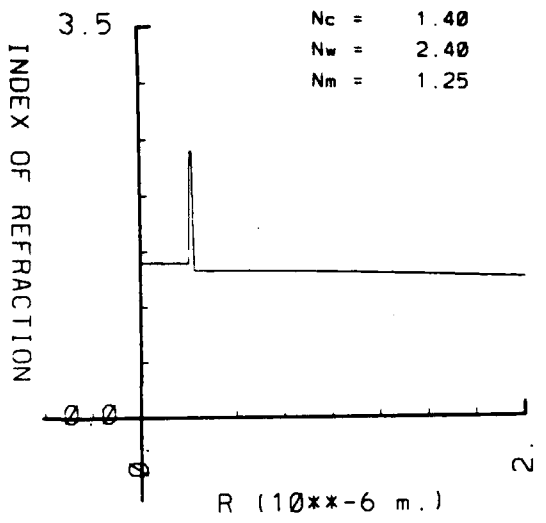
3.5
Nc = 1.40
Nw = 2.40
Nm = 1.25
INDEX OF REFRACTION
0.0
0.
2.
R (10**-6 m.)

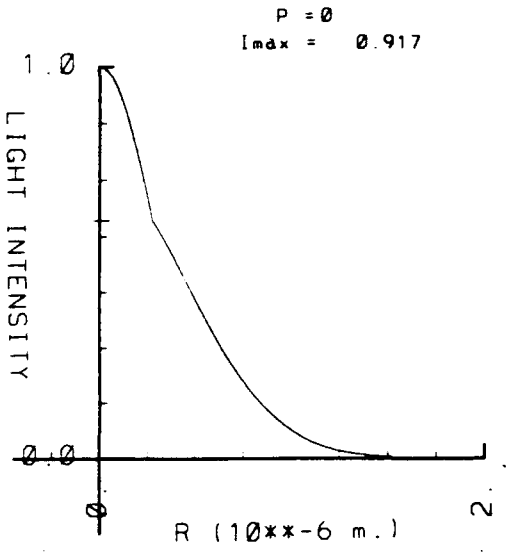
P =0
Imax = 0.917
1.0
LIGHT INTENSITY
0.0
0.
2.
R (10**-6 m.)

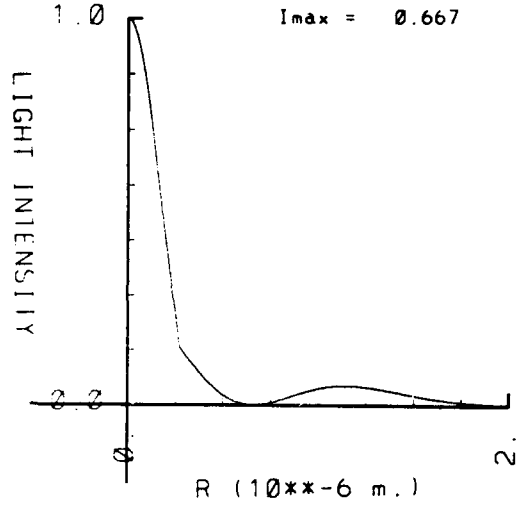
1.0
Imax = 0.667
LIGHT INTENSITY
0.0
0.
2.
R (10**-6 m.)

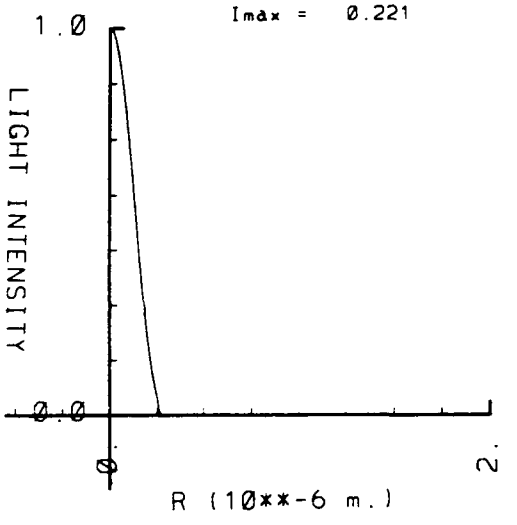
1.0
Imax = 0.221
LIGHT INTENSITY
0.0
0.
2.
R (10**-6 m.)

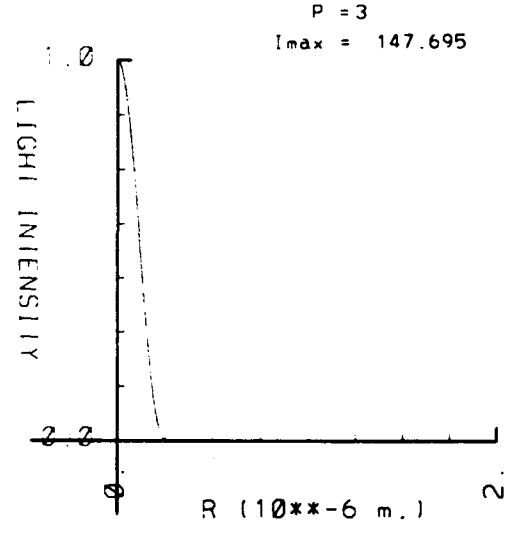
P =3
Imax = 147.695
1.0
LIGHT INTENSITY
0.0
0.
2.
R (10**-6 m.)

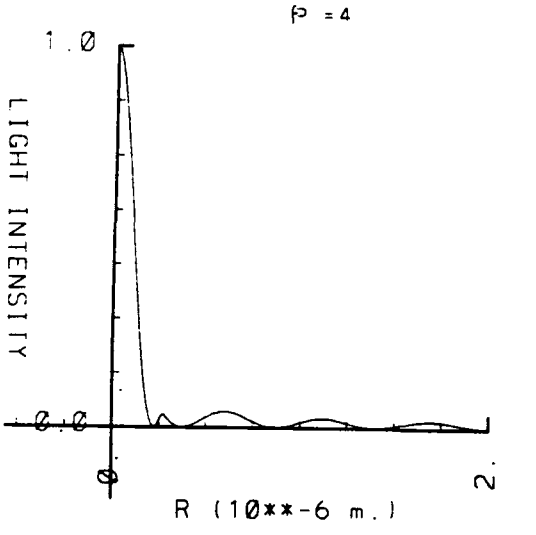
P =4
1.0
LIGHT INTENSITY
0.0
0.
2.
R (10**-6 m.)

Figure 4A

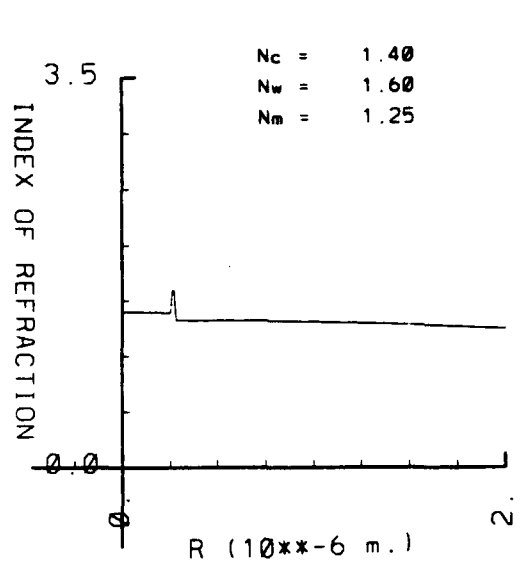
Nc = 1.40
Nw = 1.60
Nm = 1.25
3.5
INDEX OF REFRACTION
0.0
0.
2.
R (10**-6 m.)

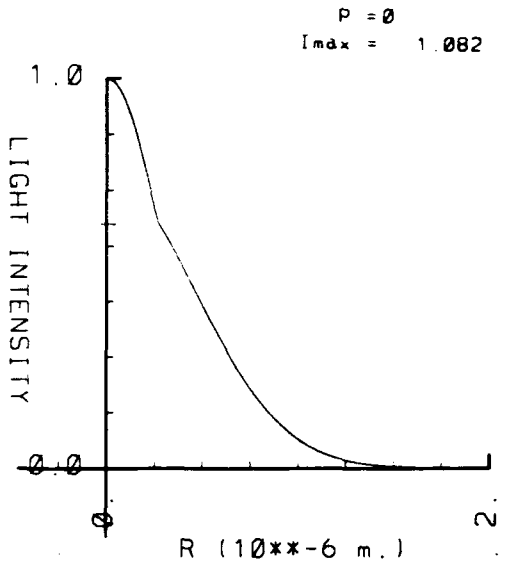
P = 0
Imax = 1.082
1.0
LIGHT INTENSITY
0.0
0.
2.
R (10**-6 m.)

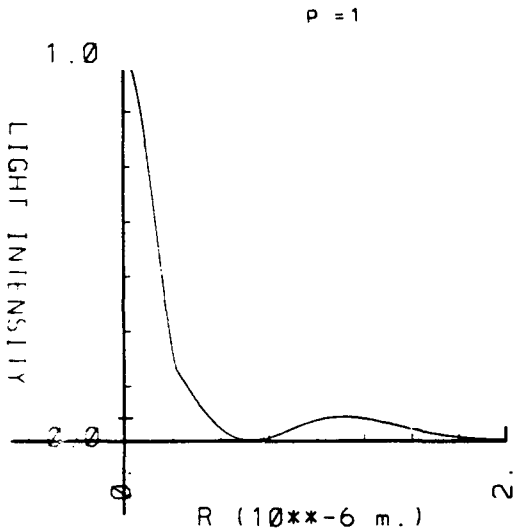
P = 1
1.0
LIGHT INTENSITY
0.0
0.
2.
R (10**-6 m.)

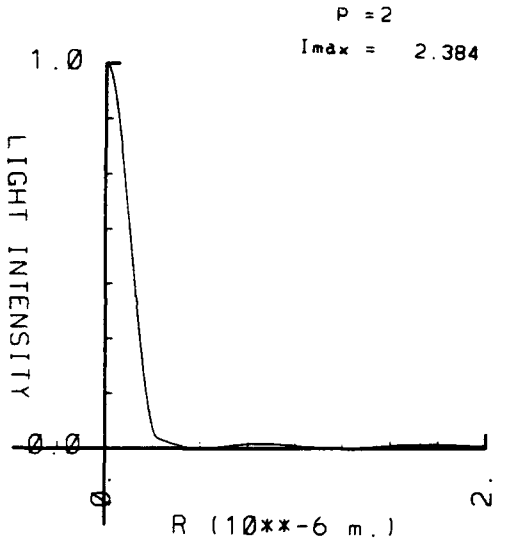
P = 2
Imax = 2.384
1.0
LIGHT INTENSITY
0.0
0.
2.
R (10**-6 m.)

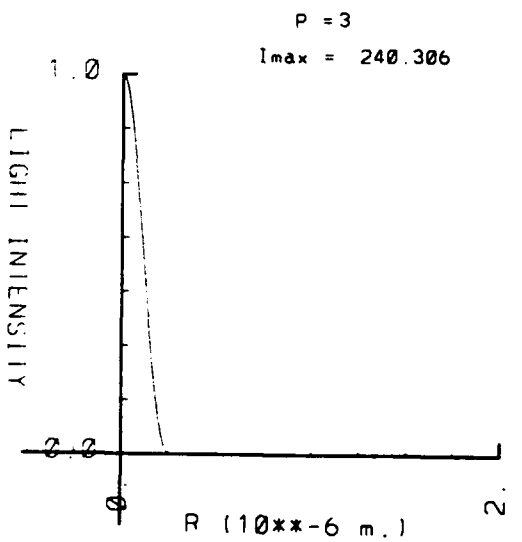
P = 3
Imax = 240.306
1.0
LIGHT INTENSITY
0.0
0.
2.
R (10**-6 m.)

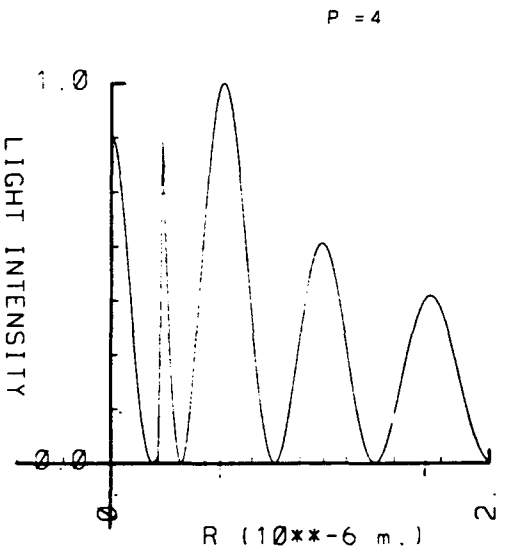
P = 4
1.0
LIGHT INTENSITY
0.0
0.
2.
R (10**-6 m.)

Figure 5A

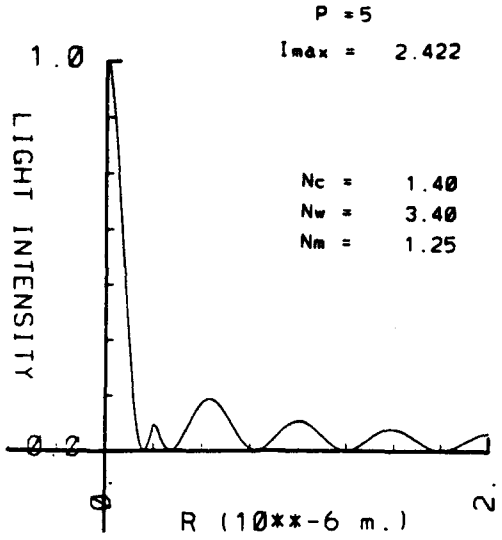

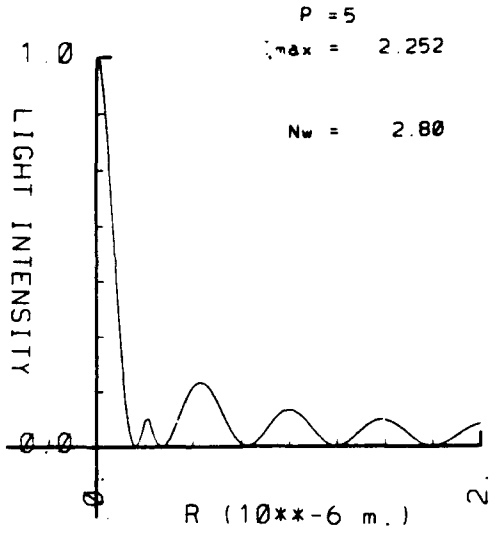

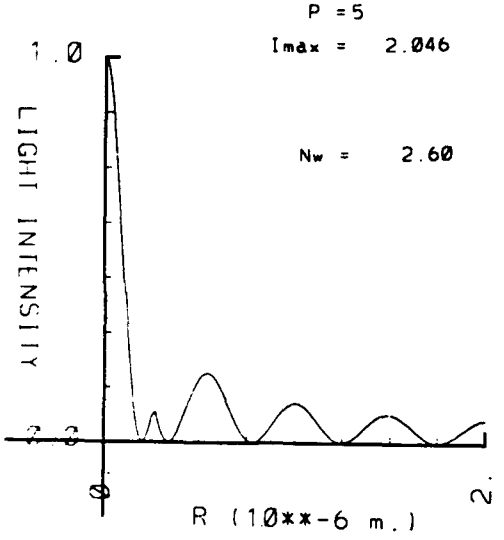

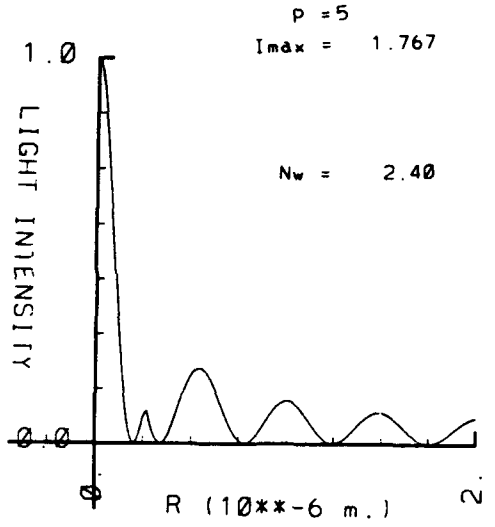

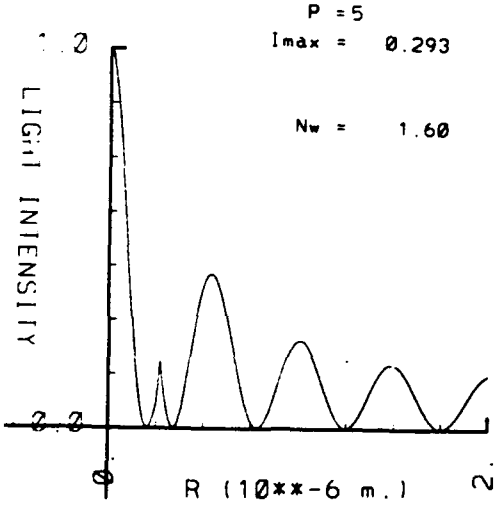

1.d-12*Ac=0.2000 m.**-2
1.d-12*Aw=0.1000 m.**-2
Am =0.1250

R1 = 0.250 microns
R2 = 0.270 microns
Rm = 2.000 microns

omega= 3.142 fmsec**-1

Figure 6A

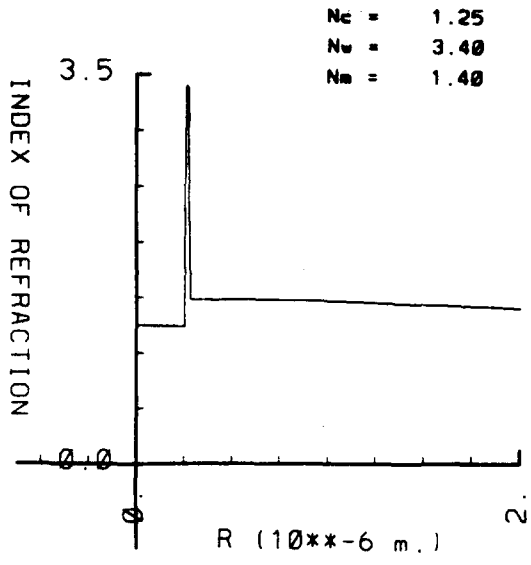
Nc = 1.25
Nw = 3.40
Nm = 1.40
3.5
INDEX OF REFRACTION
0.0
0.
2.
R (10**-6 m.)

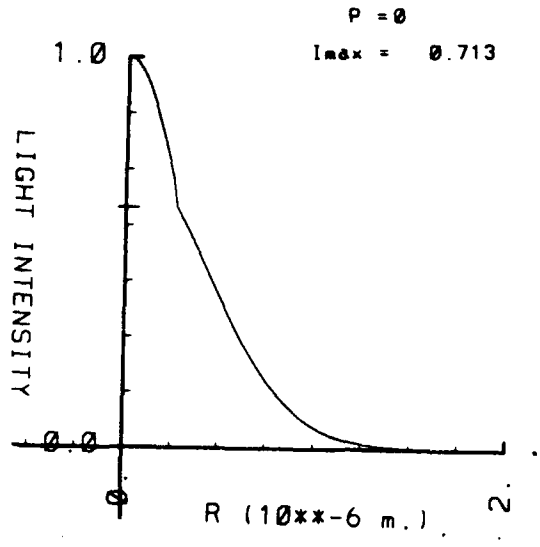
P = 0
Imax = 0.713
1.0
LIGHT INTENSITY
0.0
0.
2.
R (10**-6 m.)

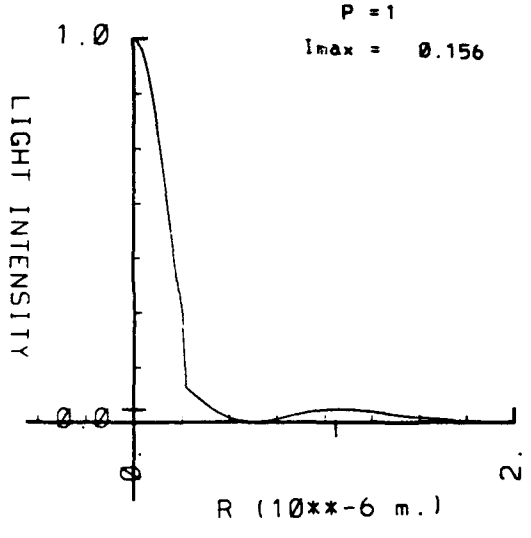
P = 1
Imax = 0.156
1.0
LIGHT INTENSITY
0.0
0.
2.
R (10**-6 m.)

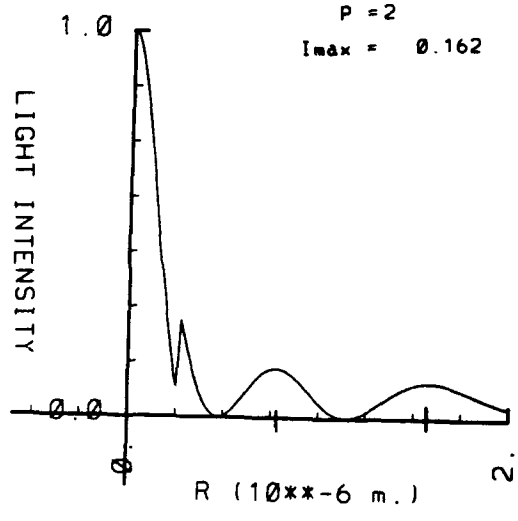
P = 2
Imax = 0.162
1.0
LIGHT INTENSITY
0.0
0.
2.
R (10**-6 m.)

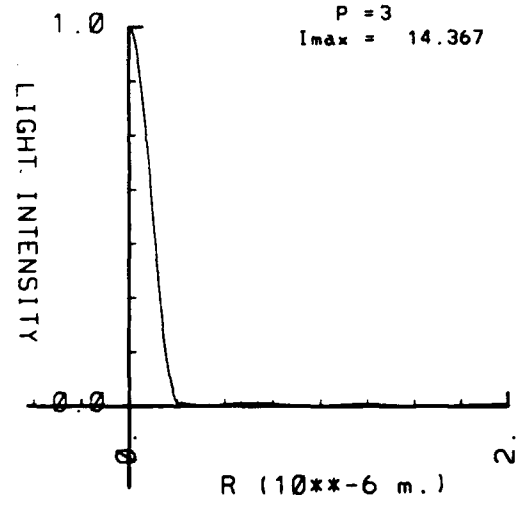
P = 3
Imax = 14.367
1.0
LIGHT INTENSITY
0.0
0.
2.
R (10**-6 m.)

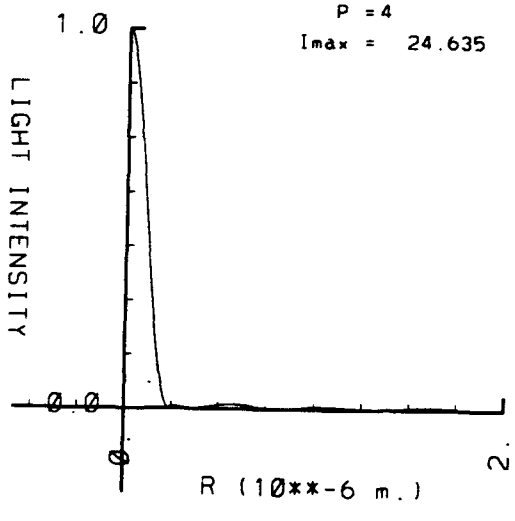
P = 4
Imax = 24.635
1.0
LIGHT INTENSITY
0.0
0.
2.
R (10**-6 m.)

Figure 7A

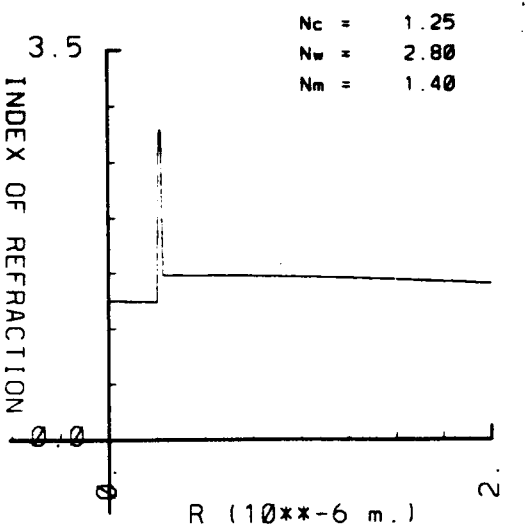
Nc = 1.25
Nw = 2.80
Nm = 1.40
3.5
INDEX OF REFRACTION
0.0
0.
R (10**-6 m.)
2.

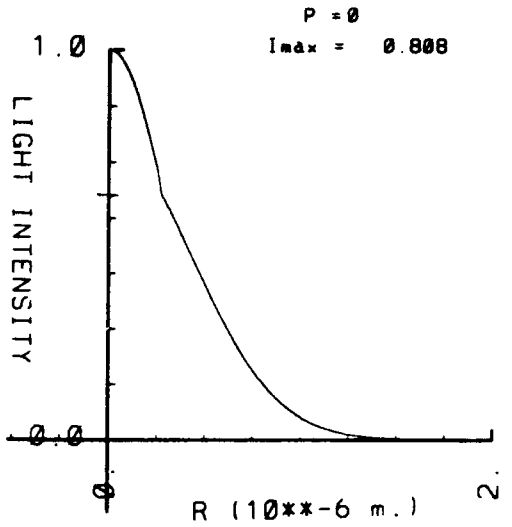
P = 0
Imax = 0.808
1.0
LIGHT INTENSITY
0.0
0.
R (10**-6 m.)
2.

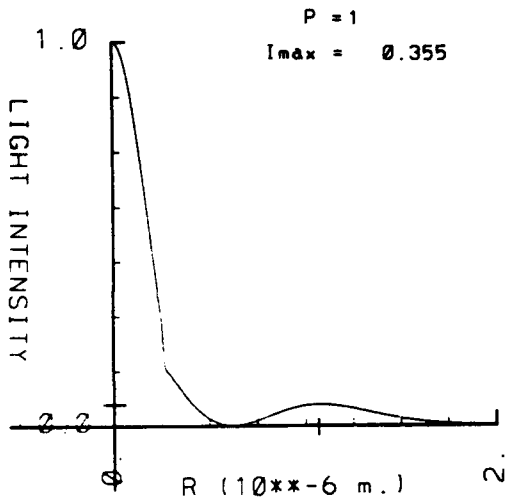
P = 1
Imax = 0.355
1.0
LIGHT INTENSITY
0.0
0.
R (10**-6 m.)
2.

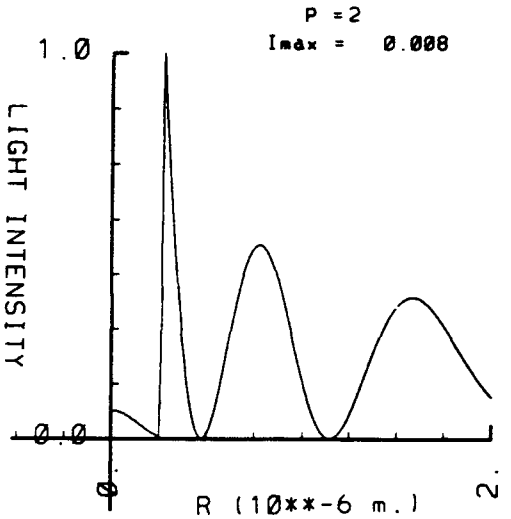
P = 2
Imax = 0.008
1.0
LIGHT INTENSITY
0.0
0.
R (10**-6 m.)
2.

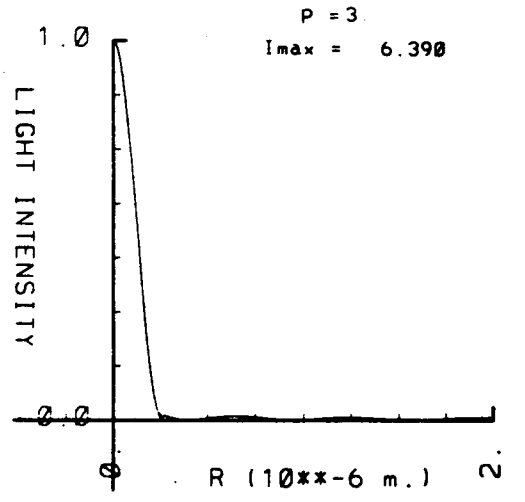
P = 3
Imax = 6.390
1.0
LIGHT INTENSITY
0.0
0.
R (10**-6 m.)
2.

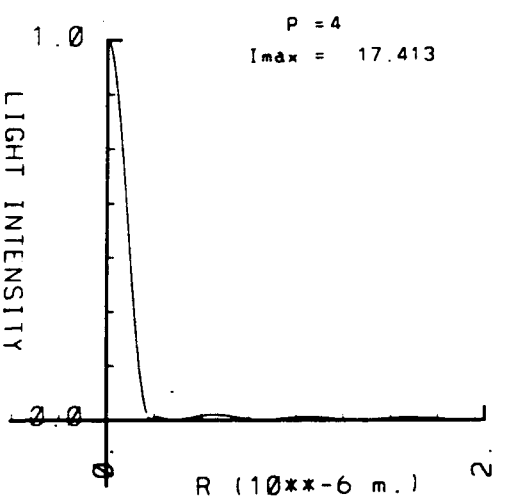
P = 4
Imax = 17.413
1.0
LIGHT INTENSITY
0.0
0.
R (10**-6 m.)
2.

Figure 8A

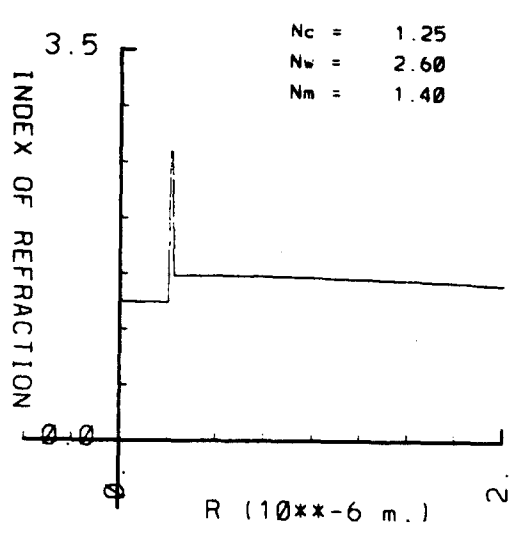
Nc = 1.25
Nw = 2.60
Nm = 1.40
3.5
INDEX OF REFRACTION
0.0
0
R (10**-6 m.)
2.

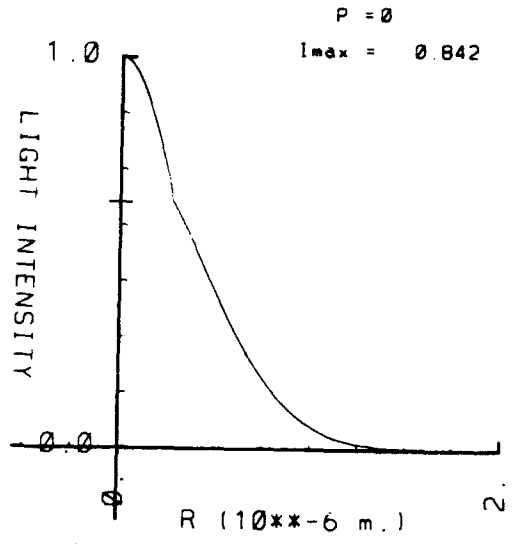
P = 0
Imax = 0.842
1.0
LIGHT INTENSITY
0.0
0
R (10**-6 m.)
2.

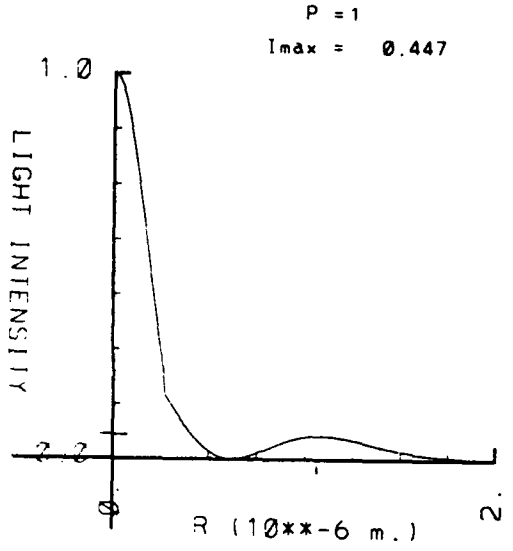
P = 1
Imax = 0.447
1.0
LIGHT INTENSITY
0.0
0
R (10**-6 m.)
2.

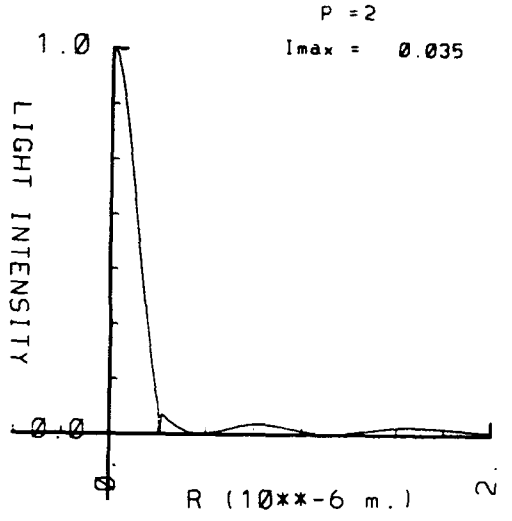
P = 2
Imax = 0.035
1.0
LIGHT INTENSITY
0.0
0
R (10**-6 m.)
2.

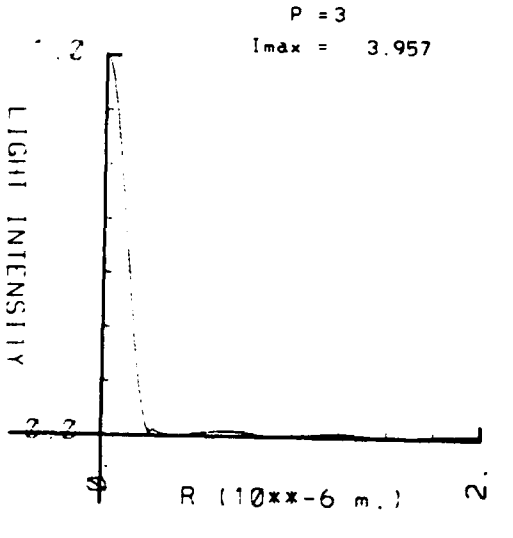
P = 3
Imax = 3.957
LIGHT INTENSITY
0.0
0
R (10**-6 m.)
2.

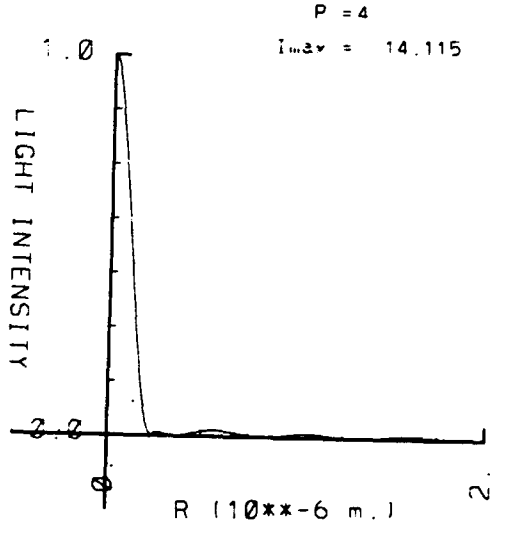
P = 4
Imax = 14.115
1.0
LIGHT INTENSITY
0.0
0
R (10**-6 m.)
2.

Figure 9A

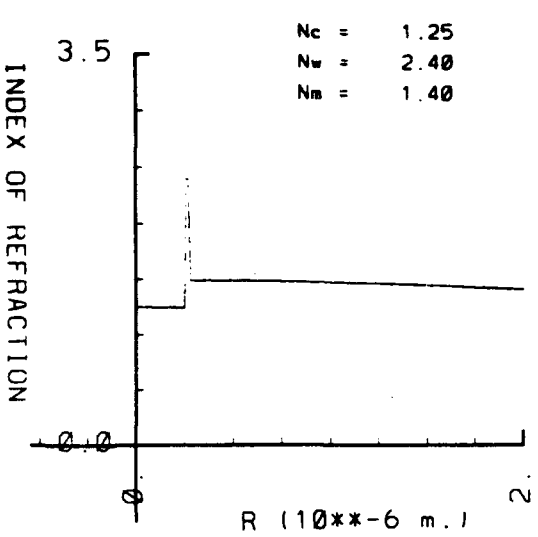
Nc = 1.25
Nw = 2.40
Nm = 1.40
INDEX OF REFRACTION
3.5
0.0
0.
2.
R (10**-6 m.)

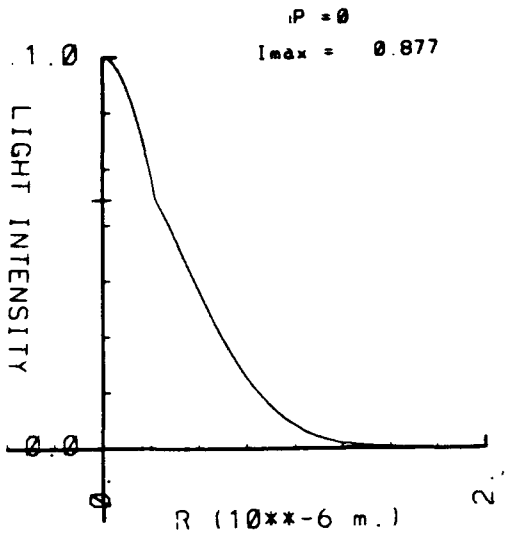
P =0
Imax = 0.877
LIGHT INTENSITY
1.0
0.0
0.
2.
R (10**-6 m.)

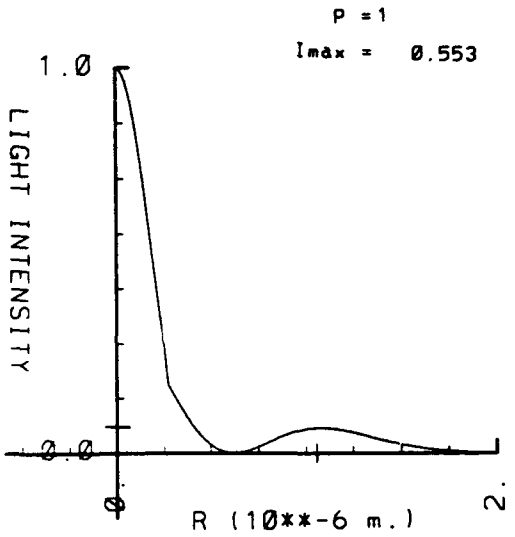
P =1
Imax = 0.553
LIGHT INTENSITY
1.0
0.0
0.
2.
R (10**-6 m.)

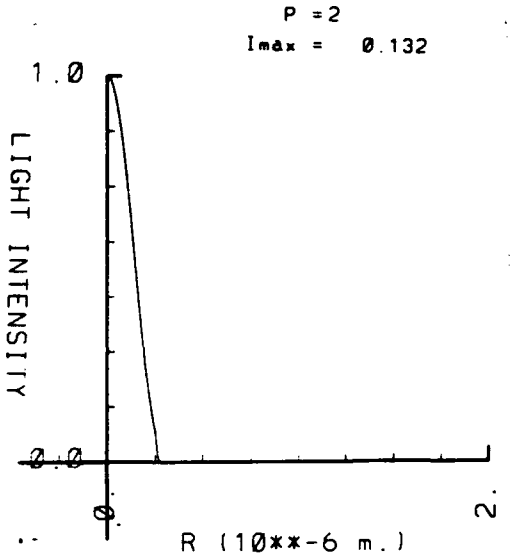
P =2
Imax = 0.132
LIGHT INTENSITY
1.0
0.0
0.
2.
R (10**-6 m.)

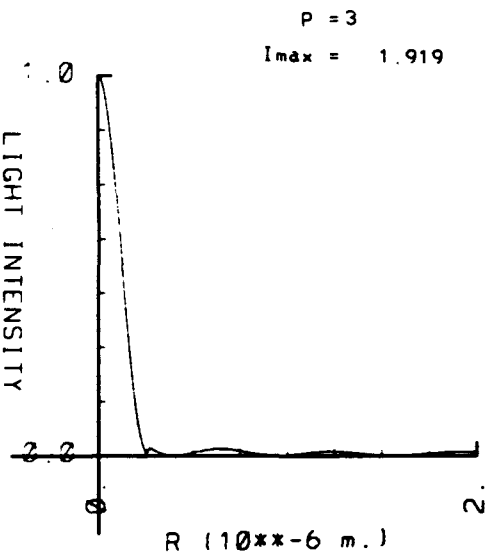
P =3
Imax = 1.919
LIGHT INTENSITY
0.0
0.
2.
R (10**-6 m.)

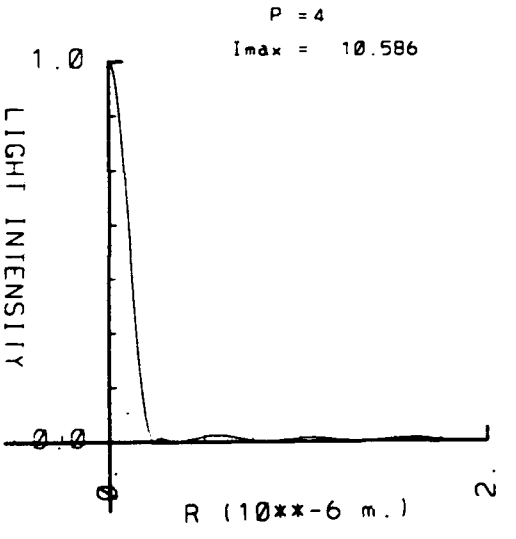
P =4
Imax = 10.586
LIGHT INTENSITY
1.0
0.0
0.
2.
R (10**-6 m.)

Figure 10A

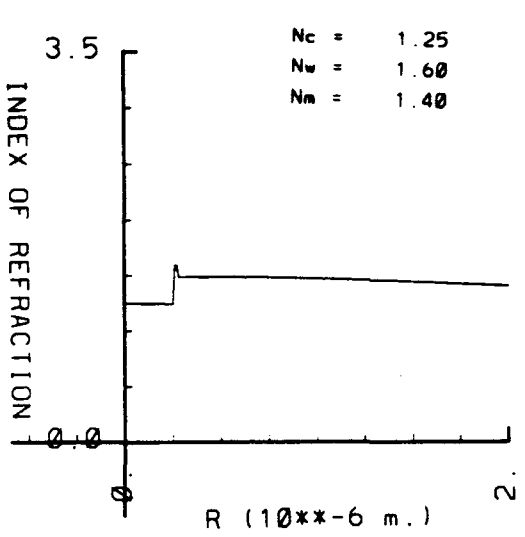
Nc = 1.25
Nw = 1.60
Nm = 1.40
3.5
INDEX OF REFRACTION
0.0
0.
2.
R (10**-6 m.)

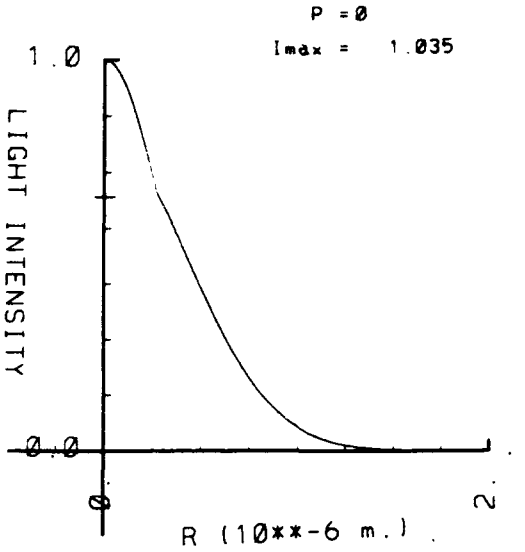
P = 0
Imax = 1.035
1.0
LIGHT INTENSITY
0.0
0.
2.
R (10**-6 m.)

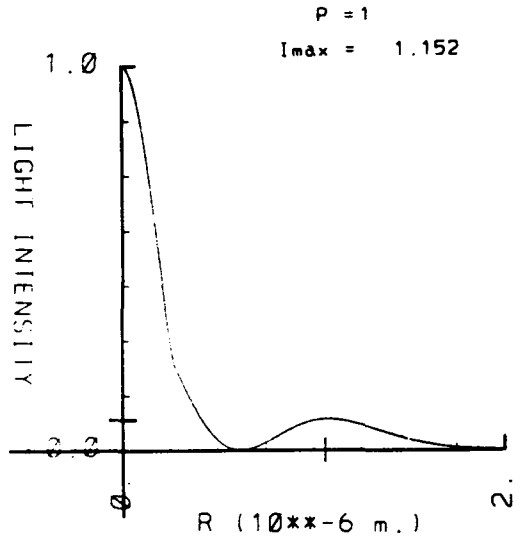
P = 1
Imax = 1.152
1.0
LIGHT INTENSITY
0.0
0.
2.
R (10**-6 m.)

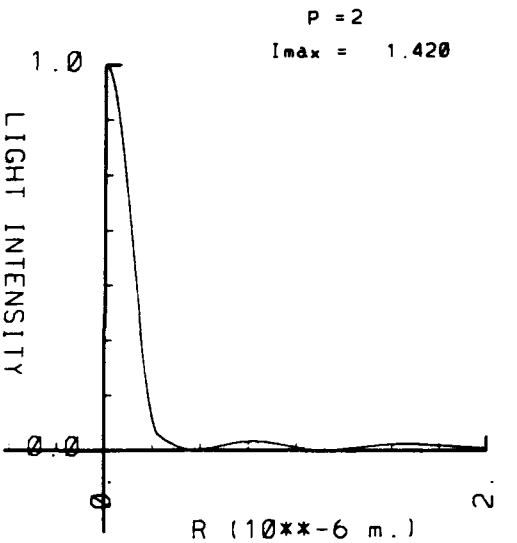
P = 2
Imax = 1.420
1.0
LIGHT INTENSITY
0.0
0.
2.
R (10**-6 m.)

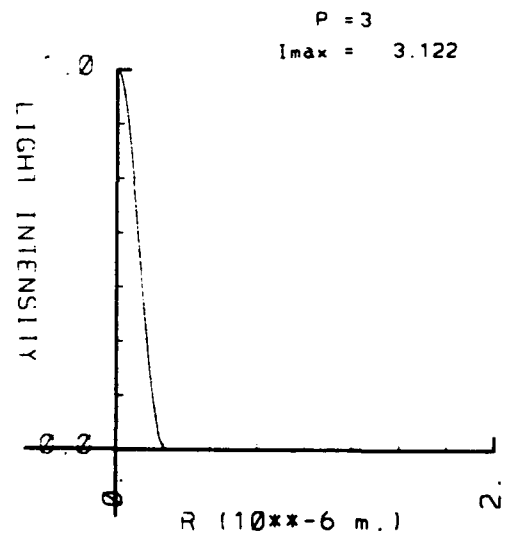
P = 3
Imax = 3.122
1.0
LIGHT INTENSITY
0.0
0.
2.
R (10**-6 m.)

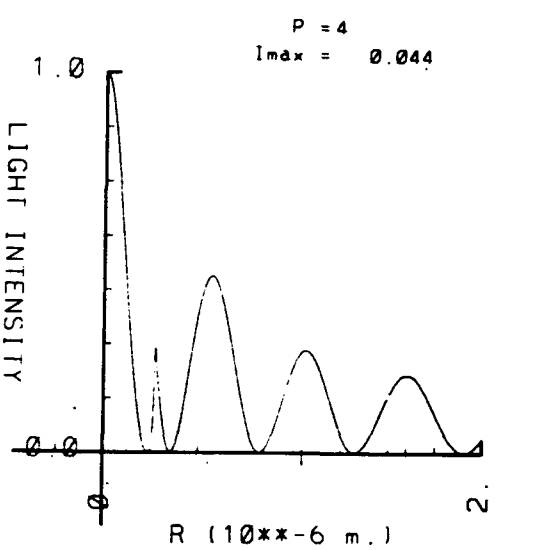
P = 4
Imax = 0.044
1.0
LIGHT INTENSITY
0.0
0.
2.
R (10**-6 m.)

Figure 11A

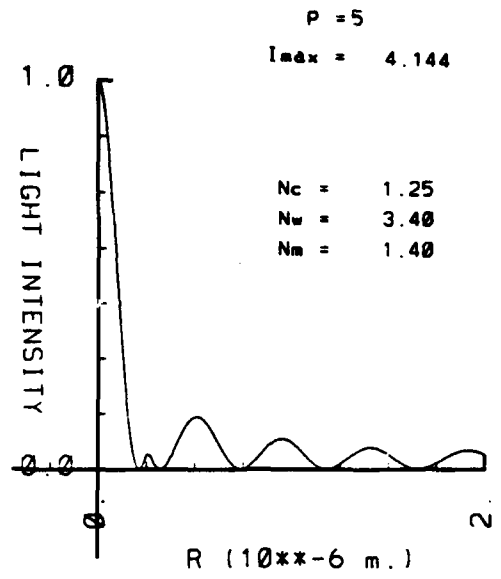

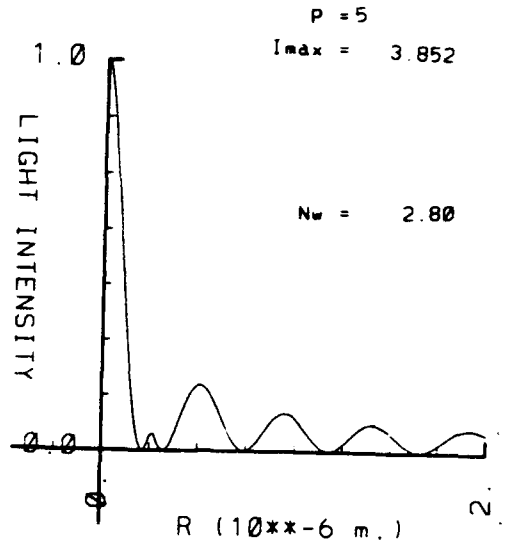

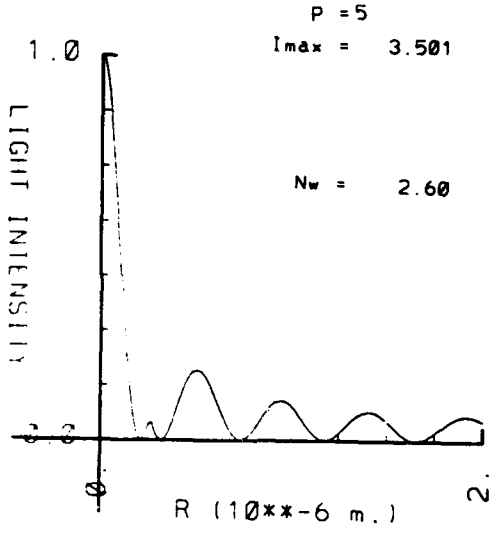

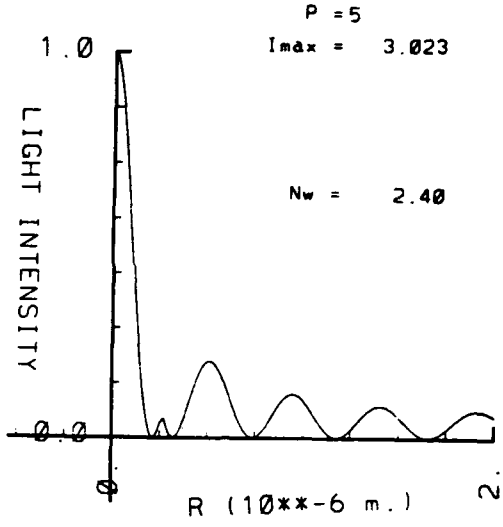

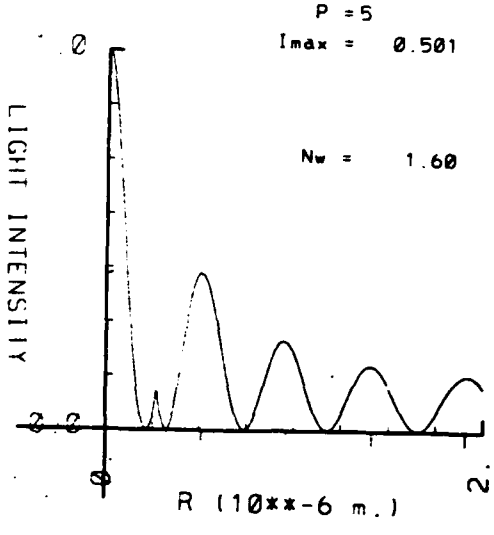

1.d-12*Ac=0.2000 m.**-2
1.d-12*Aw=0.1000 m.**-2
Am =0.1250

R1 = 0.250 microns
R2 = 0.270 microns
Rm = 2.000 microns

. omega= 3.142 fmsec**-1

Figure 12A

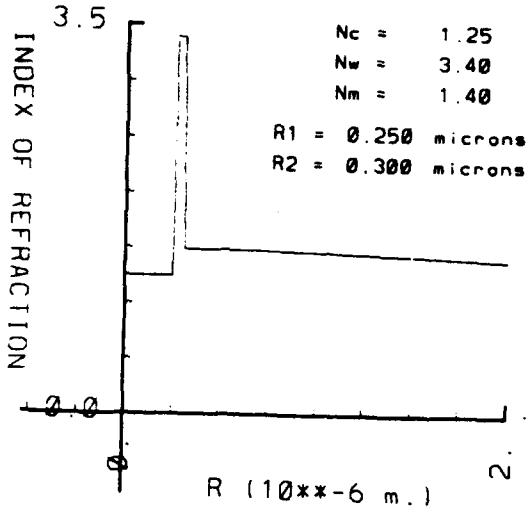
3.5
INDEX OF REFRACTION
Nc = 1.25
Nw = 3.40
Nm = 1.40
R1 = 0.250 microns
R2 = 0.300 microns
0.0
0.
2.
R (10**-6 m.)

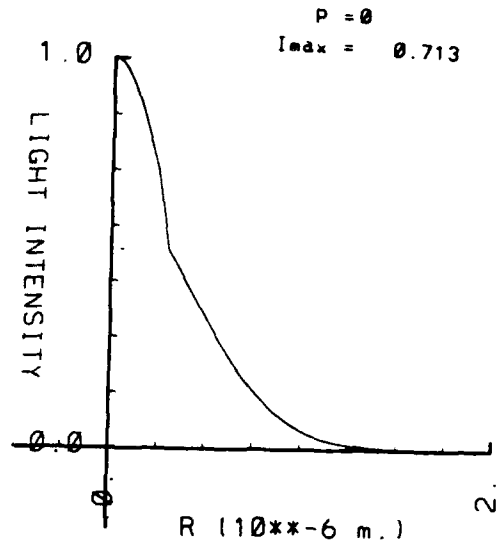
P = 0
Imax = 0.713
1.0
LIGHT INTENSITY
0.0
0.
2.
R (10**-6 m.)

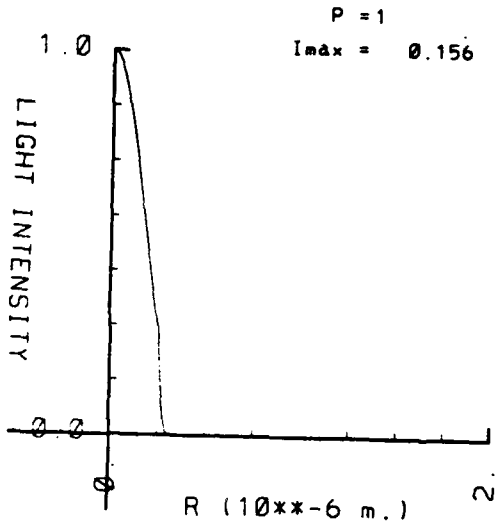
P = 1
Imax = 0.156
1.0
LIGHT INTENSITY
0.0
0.
2.
R (10**-6 m.)

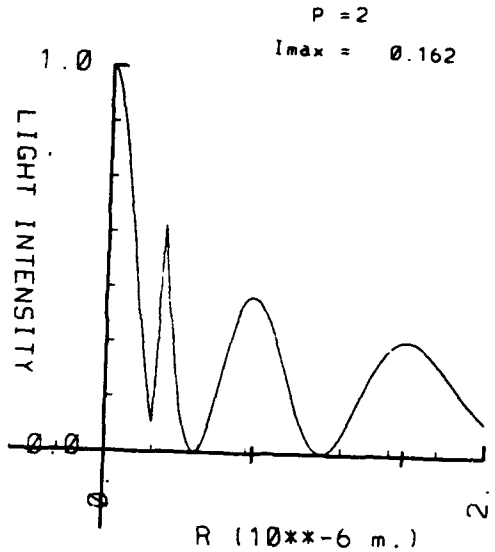
P = 2
Imax = 0.162
1.0
LIGHT INTENSITY
0.0
0.
2.
R (10**-6 m.)

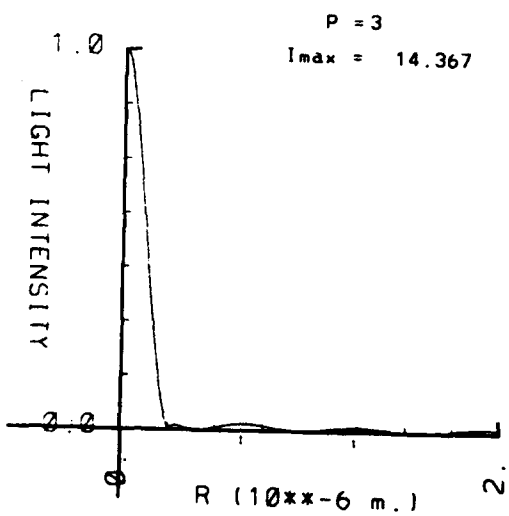
P = 3
Imax = 14.367
1.0
LIGHT INTENSITY
0.0
0.
2.
R (10**-6 m.)

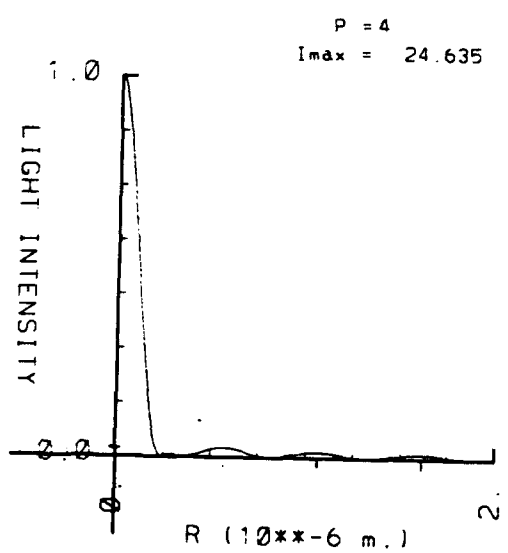
P = 4
Imax = 24.635
1.0
LIGHT INTENSITY
0.0
0.
2.
R (10**-6 m.)

Figure 13A

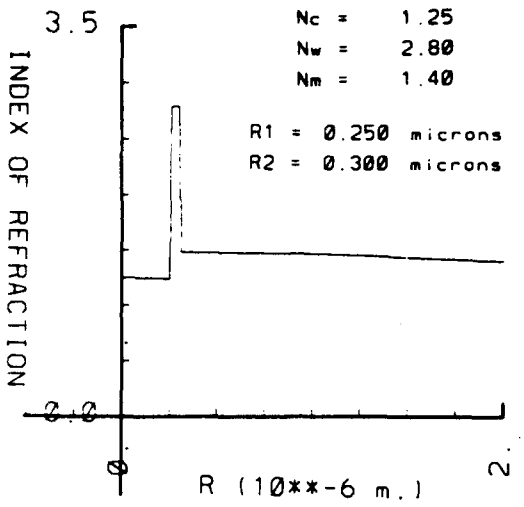
3.5
Nc = 1.25
Nw = 2.80
Nm = 1.40
R1 = 0.250 microns
R2 = 0.300 microns
INDEX OF REFRACTION
0.0
0.
2.
R (10**-6 m.)

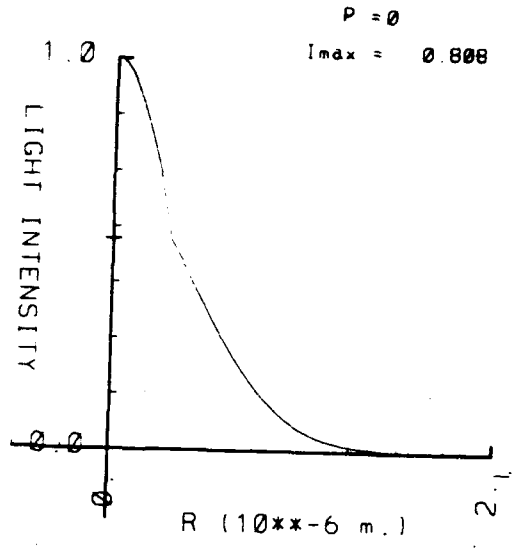
P = 0
Imax = 0.808
1.0
LIGHT INTENSITY
0.0
0.
2.
R (10**-6 m.)

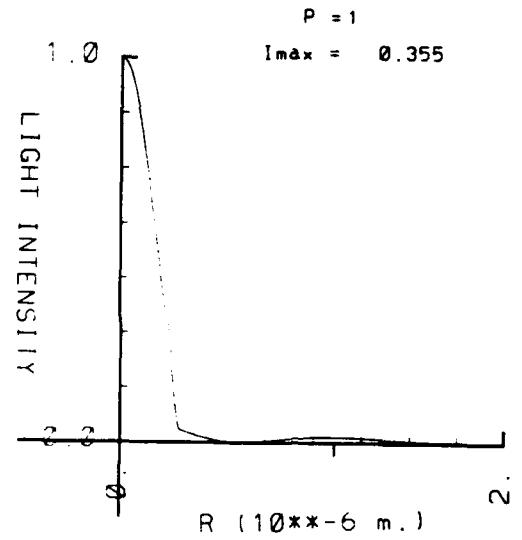
P = 1
Imax = 0.355
1.0
LIGHT INTENSITY
0.0
0.
2.
R (10**-6 m.)

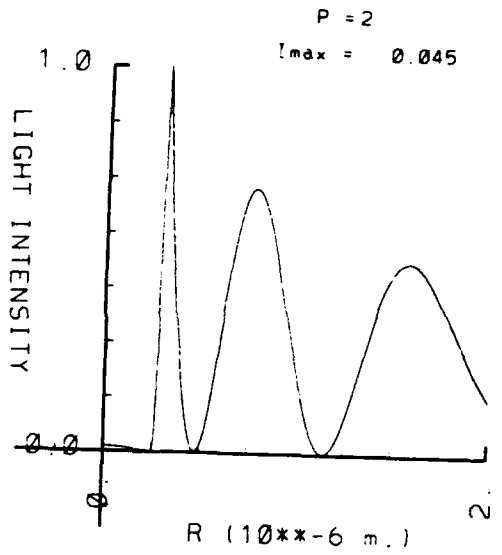
P = 2
Imax = 0.045
1.0
LIGHT INTENSITY
0.0
0.
2.
R (10**-6 m.)

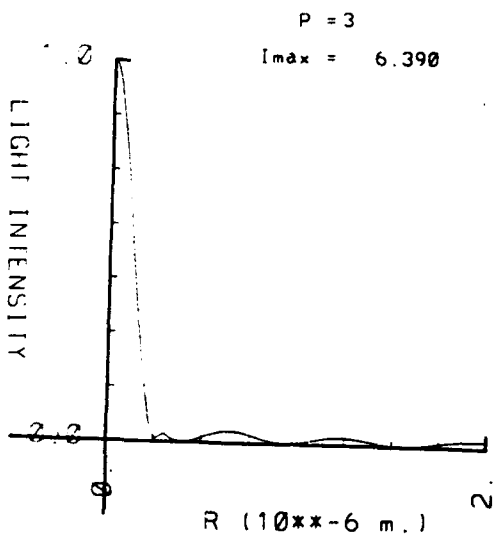
P = 3
Imax = 6.390
1.0
LIGHT INTENSITY
0.0
0.
2.
R (10**-6 m.)

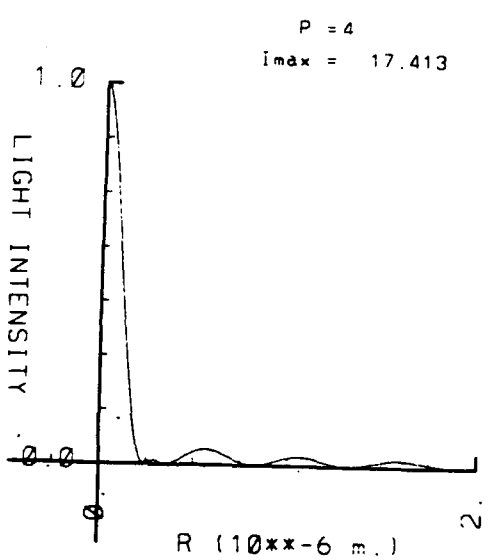
P = 4
Imax = 17.413
1.0
LIGHT INTENSITY
0.0
0.
2.
R (10**-6 m.)

Figure 14A

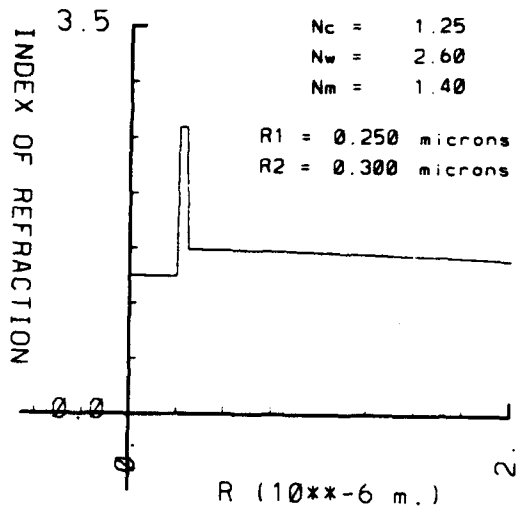
3.5
INDEX OF REFRACTION
Nc = 1.25
Nw = 2.60
Nm = 1.40
R1 = 0.250 microns
R2 = 0.300 microns
0.0
0.
2.
R (10**-6 m.)

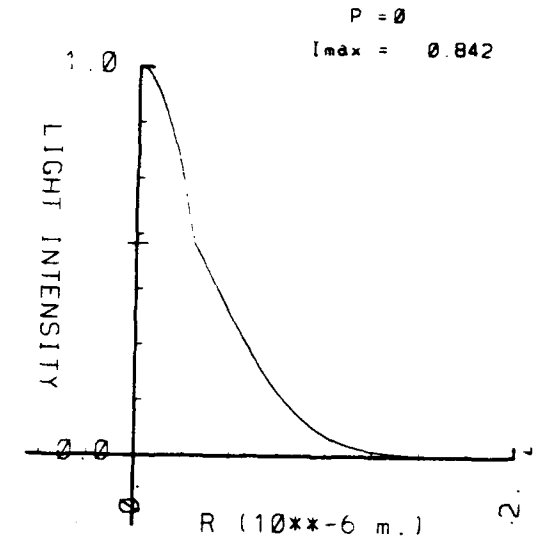
P = 0
Imax = 0.842
1.0
LIGHT INTENSITY
0.0
0.
2.
R (10**-6 m.)

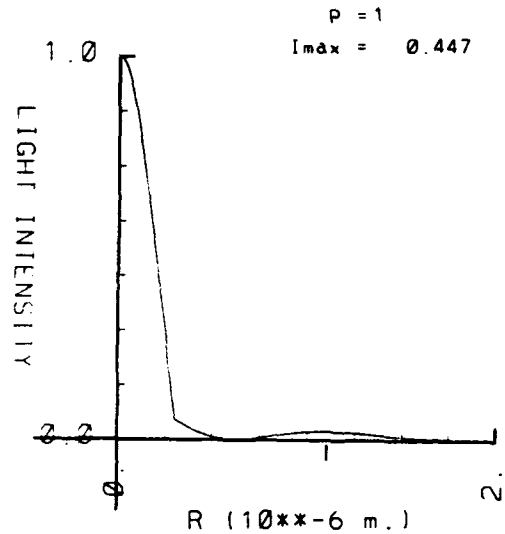
P = 1
Imax = 0.447
1.0
LIGHT INTENSITY
0.0
0.
1
2.
R (10**-6 m.)

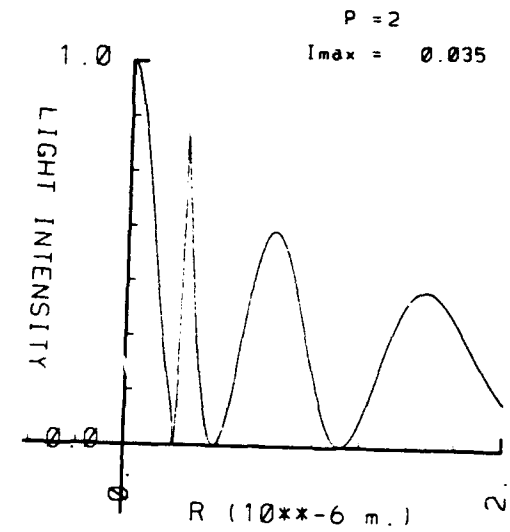
P = 2
Imax = 0.035
1.0
LIGHT INTENSITY
0.0
0.
2.
R (10**-6 m.)

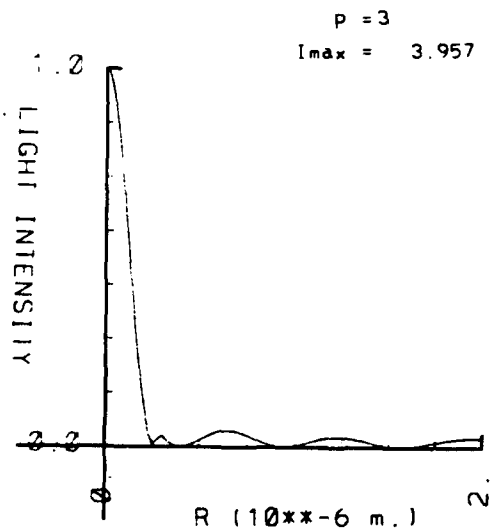
P = 3
Imax = 3.957
1.0
LIGHT INTENSITY
0.0
0.
2.
R (10**-6 m.)

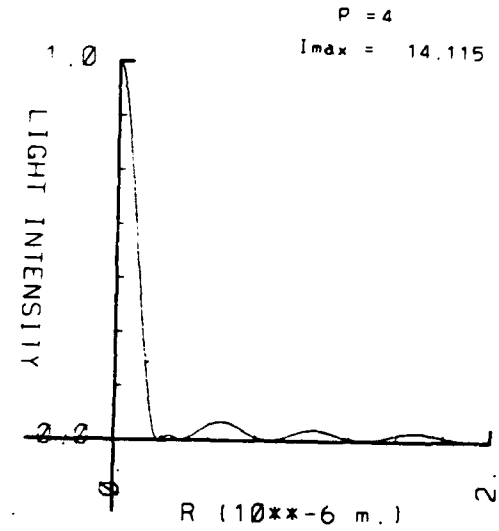
P = 4
Imax = 14.115
1.0
LIGHT INTENSITY
0.0
0.
2.
R (10**-6 m.)

Figure 15A

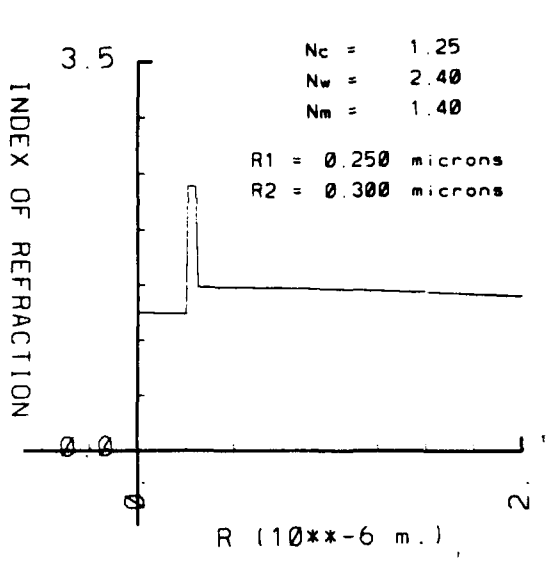
3.5
Nc = 1.25
Nw = 2.40
Nm = 1.40
R1 = 0.250 microns
R2 = 0.300 microns
INDEX OF REFRACTION
0.0
0
2.
R (10**-6 m.)

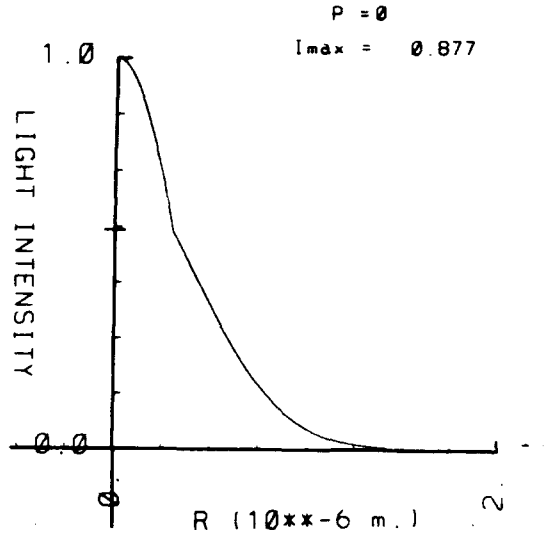
P = 0
Imax = 0.877
1.0
LIGHT INTENSITY
0.0
0
2.
R (10**-6 m.)

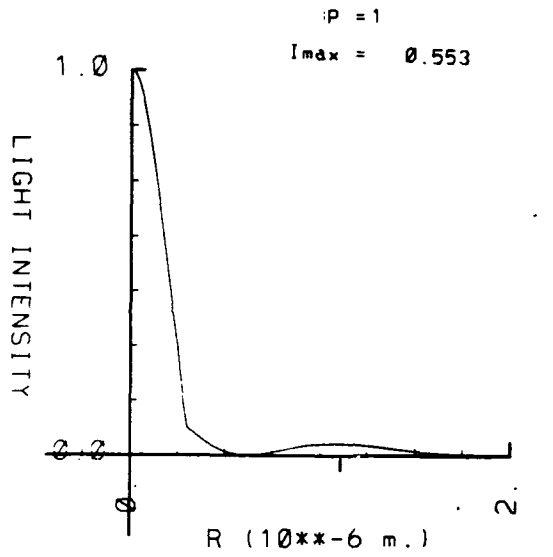
P = 1
Imax = 0.553
1.0
LIGHT INTENSITY
0.0
0
2.
R (10**-6 m.)

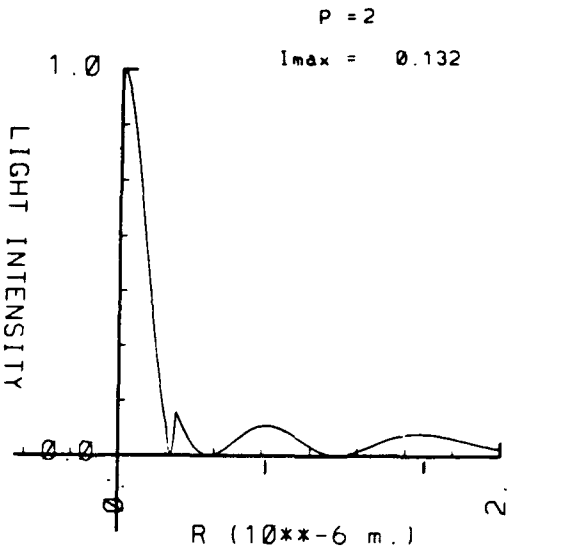
P = 2
Imax = 0.132
1.0
LIGHT INTENSITY
0.0
0
2.
R (10**-6 m.)

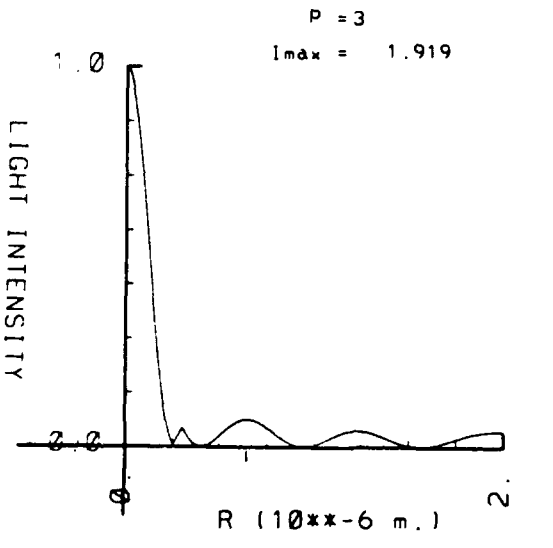
P = 3
Imax = 1.919
1.0
LIGHT INTENSITY
0.0
0
2.
R (10**-6 m.)

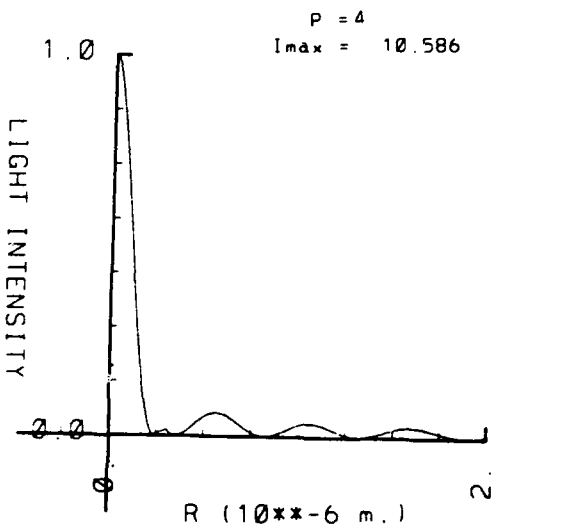
P = 4
Imax = 10.586
1.0
LIGHT INTENSITY
0.0
0
2.
R (10**-6 m.)

Figure 16A

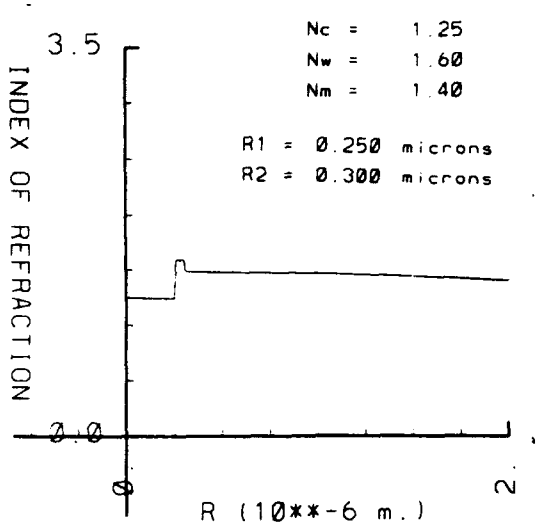
Nc = 1.25
Nw = 1.60
Nm = 1.40
R1 = 0.250 microns
R2 = 0.300 microns
INDEX OF REFRACTION
3.5
0.0
0
2.
R (10**-6 m.)

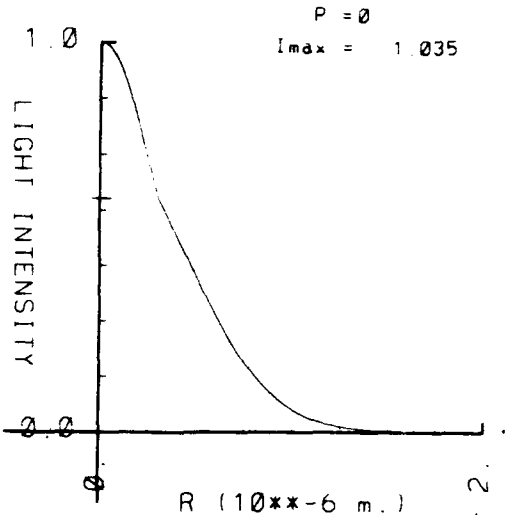
P = 0
Imax = 1.035
LIGHT INTENSITY
1.0
0.0
0
2.
R (10**-6 m.)

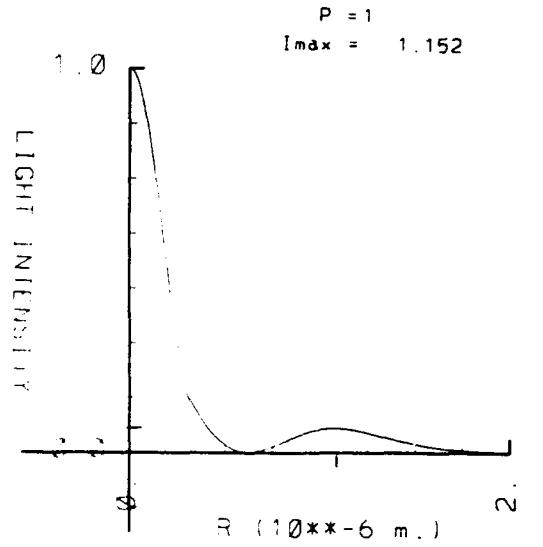
P = 1
Imax = 1.152
LIGHT INTENSITY
1.0
0
2.
R (10**-6 m.)

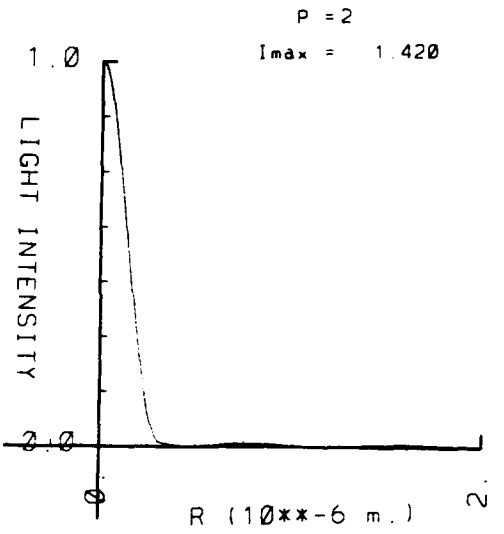
P = 2
Imax = 1.420
LIGHT INTENSITY
1.0
0.0
0
2.
R (10**-6 m.)

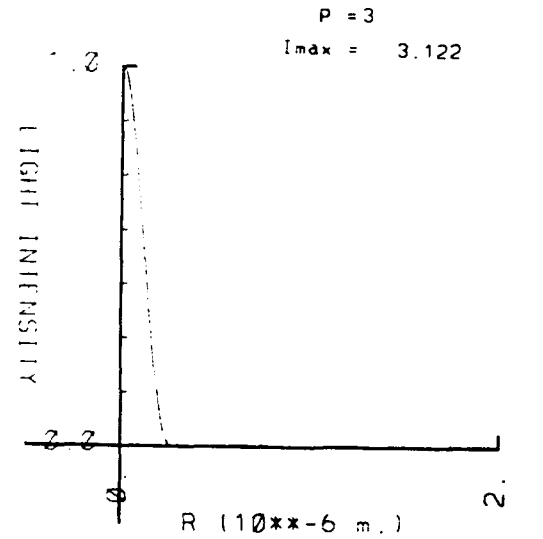
P = 3
Imax = 3.122
LIGHT INTENSITY
0
2.
R (10**-6 m.)

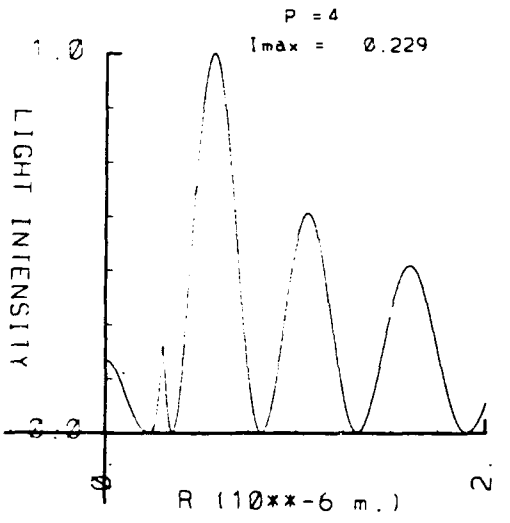
P = 4
Imax = 0.229
LIGHT INTENSITY
1.0
0.0
0
2.
R (10**-6 m.)

Figure 17A

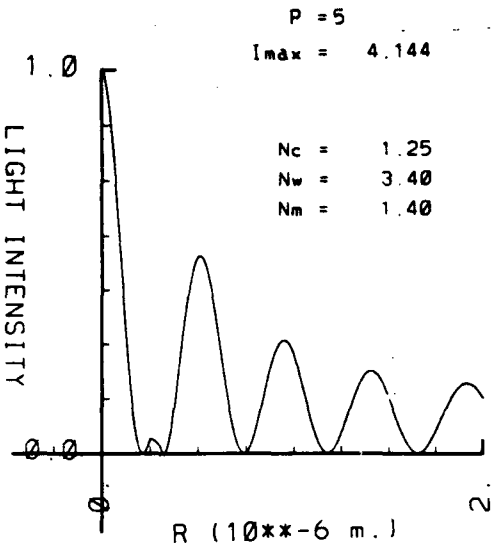

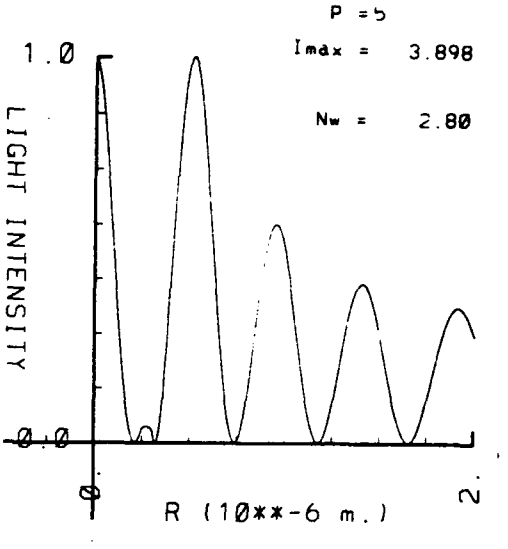

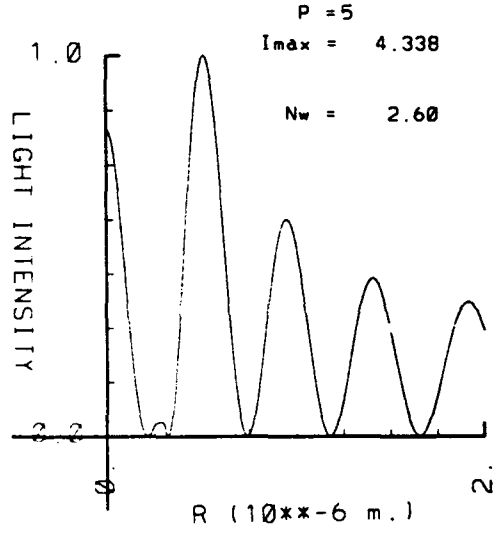

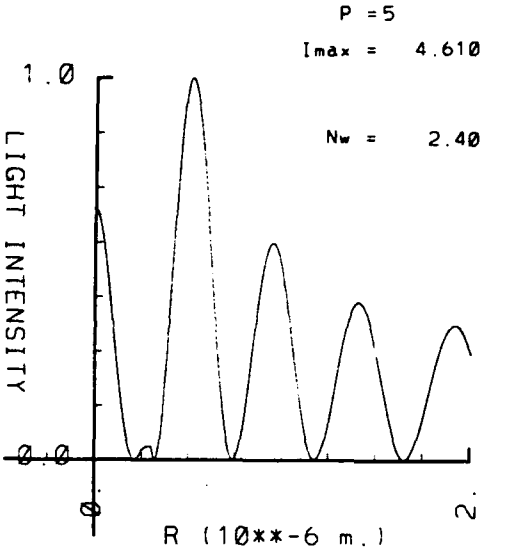

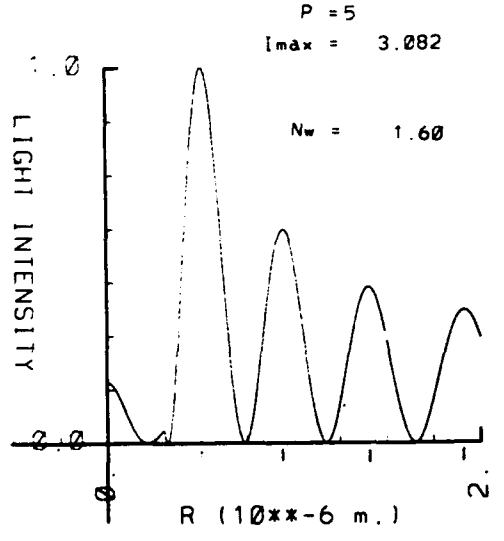

1.d-12*Ac=0.2000 m.**-2
1.d-12*Aw=0.1000 m.**-2
Am =0.1250

R1 = 0.250 microns
R2 = 0.300 microns
Rm = 2.000 microns

omega= 3.142 fmsec**-1

Figure 18A

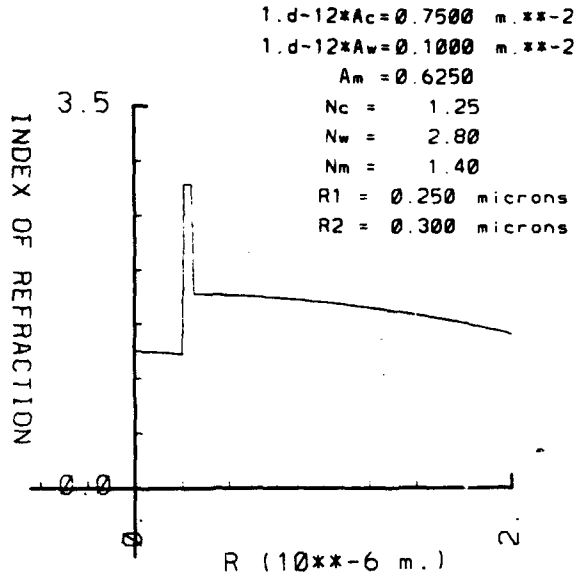
1.d-12*Ac=0.7500 m.**-2
1.d-12*Aw=0.1000 m.**-2
Am =0.6250
Nc = 1.25
Nw = 2.80
Nm = 1.40
R1 = 0.250 microns
R2 = 0.300 microns
INDEX OF REFRACTION
3.5
R (10**-6 m.)

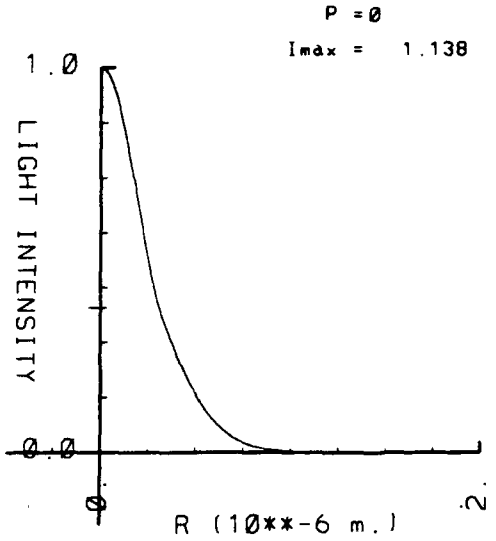
P =0
Imax = 1.138
LIGHT INTENSITY
1.0
R (10**-6 m.)

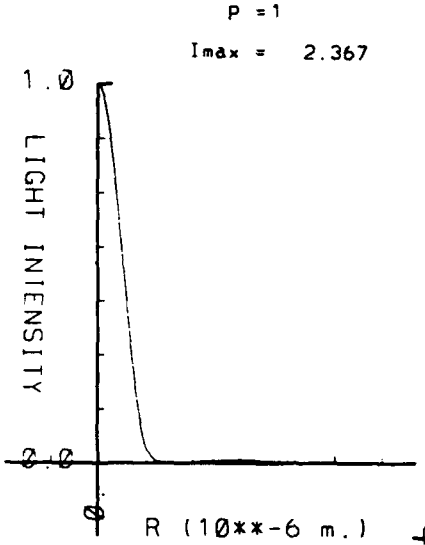
P =1
Imax = 2.367
LIGHT INTENSITY
1.0
R (10**-6 m.)

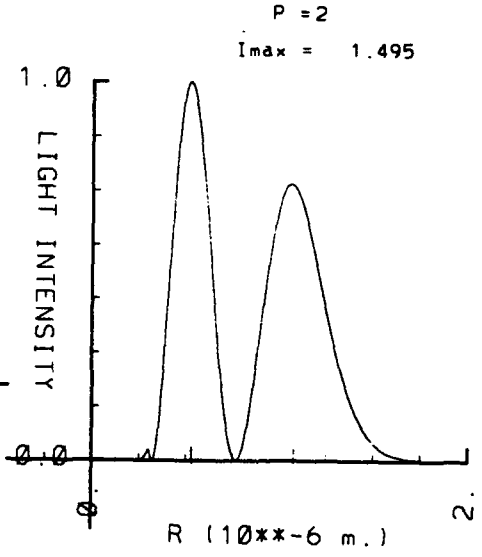
P =2
Imax = 1.495
LIGHT INTENSITY
1.0
R (10**-6 m.)

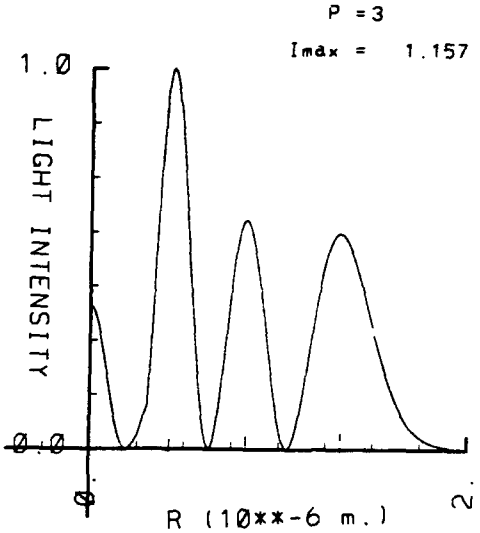
P =3
Imax = 1.157
LIGHT INTENSITY
1.0
R (10**-6 m.)

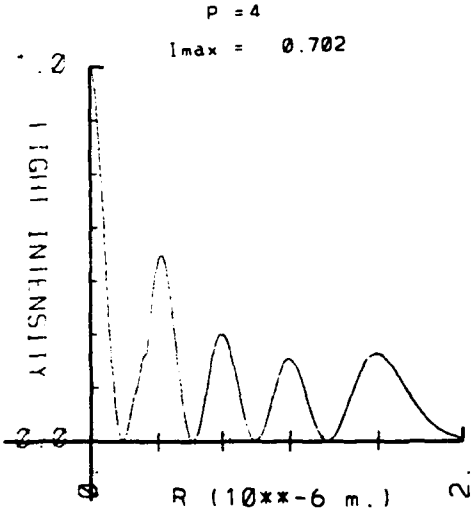
P =4
Imax = 0.702
LIGHT INTENSITY
.2
R (10**-6 m.)

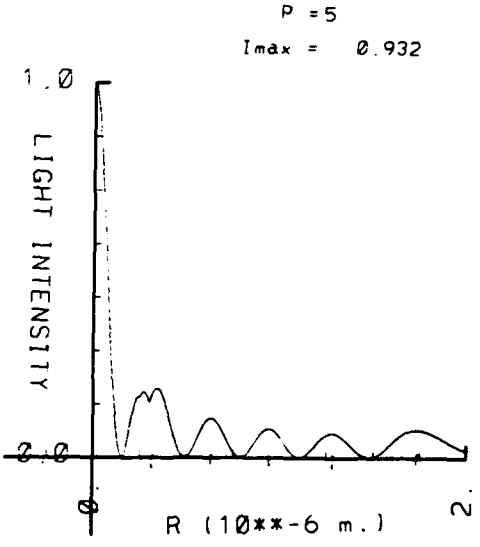
P =5
Imax = 0.932
LIGHT INTENSITY
1.0
R (10**-6 m.)

Figure 19A

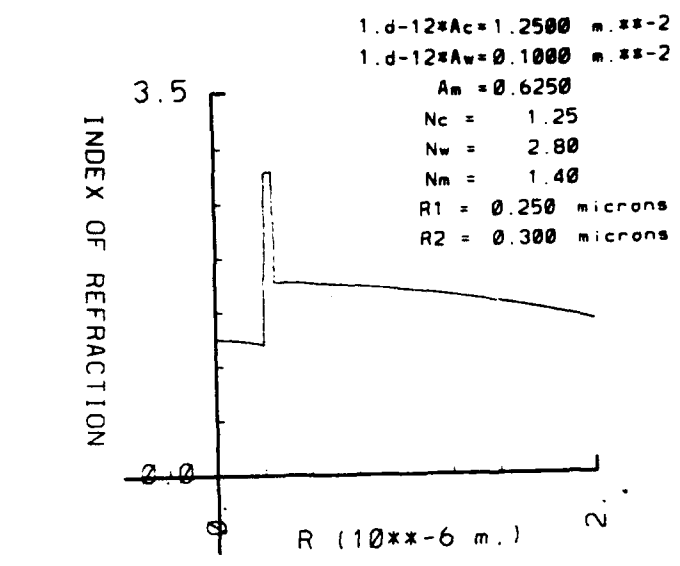
1.d-12*Ac=1.2500 m.**-2
1.d-12*Aw=0.1000 m.**-2
Am =0.6250
Nc = 1.25
Nw = 2.80
Nm = 1.40
R1 = 0.250 microns
R2 = 0.300 microns
INDEX OF REFRACTION
3.5
0.0
0.
R (10**-6 m.)
2.

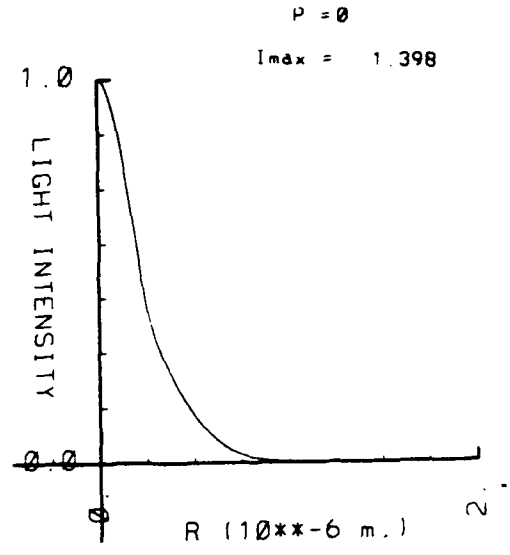
P =0
Imax = 1.398
LIGHT INTENSITY
1.0
0.0
0.
R (10**-6 m.)
2.

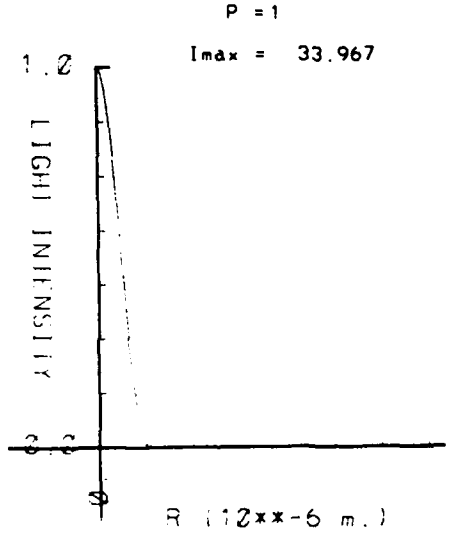
P =1
Imax = 33.967
LIGHT INTENSITY
1.0
0.0
0.
R (10**-6 m.)

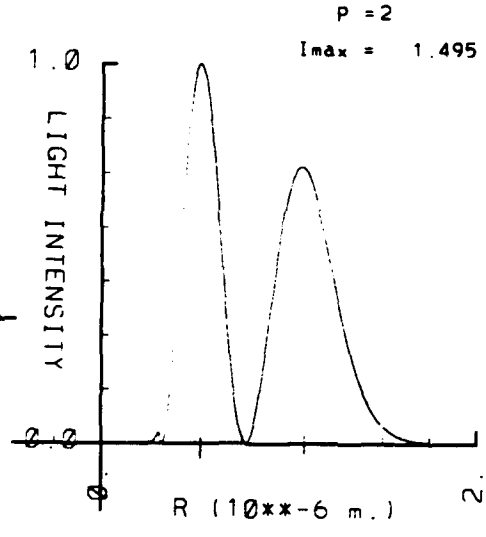
P =2
Imax = 1.495
LIGHT INTENSITY
1.0
0.0
0.
R (10**-6 m.)
2.

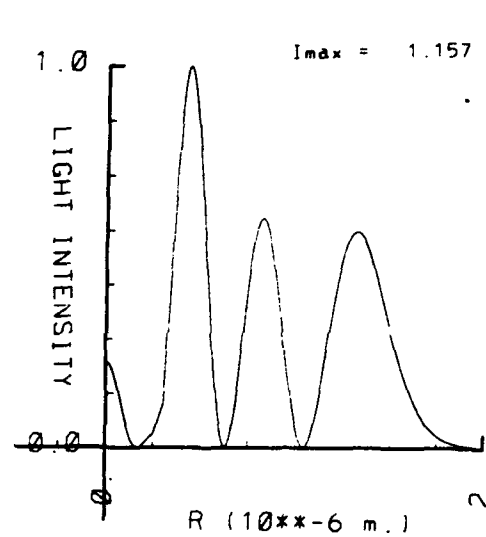
Imax = 1.157
LIGHT INTENSITY
1.0
0.0
0.
R (10**-6 m.)
2.

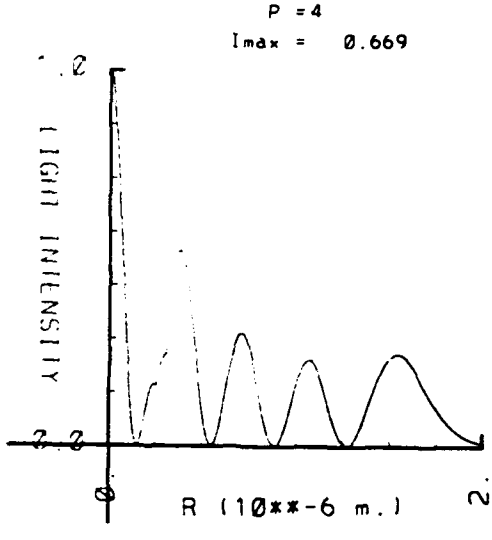
P =4
Imax = 0.669
LIGHT INTENSITY
1.0
0.0
0.
R (10**-6 m.)
2.

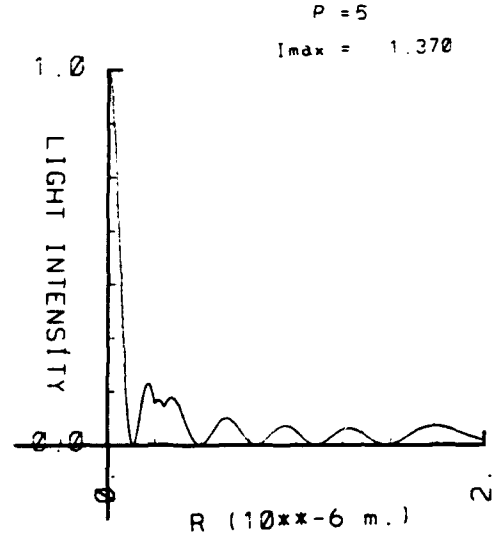
P =5
Imax = 1.370
LIGHT INTENSITY
1.0
0.0
0.
R (10**-6 m.)
2.

Figure 20A